Precision Medicine Based on Real-time Immune Status Profiling Utilizing Novel Nanoparticles and Engineered Nanomaterials

By

Yuxin Cai

A dissertation submitted to the Graduate Faculty of

Auburn University

in partial fulfillment of the requirements

for the Degree of Doctor of Philosophy

Auburn, Alabama

May.6th 2023

Keywords: Superparamagnetic, Biosensor, Cytokine,

Nanoplasmonic, microfluidics, multiplexed immunoassay

Committee:

Dr. Pengyu Chen, Associate Professor of Material Engineering

Dr. Bart Prorok, Professor of Material Engineering

Dr. Dongjoo Kim, Professor of Material Engineering

Dr. Raj Amin, Associate Professor of Drug Discovery and Development

Dr. Panagiotis Mistriotis, Assistant Professor of Chemical Engineering

Abstract

Cancer treatment strategies such as Anti-programmed death-ligand 1 (Anti-PD-L1) or chimeric antigen receptors (CAR) T-cells are limited by low objective response rates and severe side effects. This is partly due to the lack of personalized diagnosis and treatment based on the individual immune response. This research proposes the use of a lab-on-a-chip system and point-of-care (PoC) device to provide real-time monitoring of immune response, which can help reveal the fundamental mechanisms of the disease and tailor treatment to the patient's response. The challenge lies in accessing immune status profiling and performing regulated immune therapy.

To address this challenge, this research focuses on precise disease screening and developing engineering and biology techniques for immune status profiling. Localized surface plasmonic resonance (LSPR) based nanoplasmonic high throughput cytokine immunoassays and tumor-derived exosome profilings were developed to monitor cytokine levels in the tumor microenvironment. The former utilizes LSPR to monitor cytokine levels in the tumor microenvironment, while the latter identifies tumor-associated antigens that can activate immunological cell death and inhibit cancer metastasis.

Additionally, this research proposes a combined immunological cancer therapy design using copper ferrite nanoparticles as a drug load. These nanoparticles can be magnetically delivered to the tumor area, providing anti-cancer ingredients and hyperthermia effects to eliminate tumor cells. The therapy generates tumor-associated antigens that activate immunological cell death and inhibit the epithelial-mesenchymal transition to prevent cancer metastasis.

Besides considering increasing the objective rate of the immune response, immune status profiling also plays a vital role in moderating the side effects of some immune regulating strategies. Much about the mammalian nervous system and the brain's structures, functions, and connections remain unknown. Therefore, the microneedle biosensors for *in-situ* analysis of neuron signaling toward the human-computer interface were designed to provide both a neuron cytotoxic drug screening platform and a comprehensive understanding of neuron active mechanisms.

Overall, this research presents a promising approach to improve cancer treatment by combining engineering and biology techniques to monitor immune responses and tailor treatment based on individual responses.

Acknowledgments

I am deeply grateful to the numerous individuals who provided their invaluable assistance and guidance during my time at Auburn University, without whom the successful culmination of this study would not have been feasible.

First and foremost, I would like to thank my advisor, Prof. Pengyu Chen for his continued support and guidance throughout my Ph.D. journey. I am so grateful to work with such an outstanding researcher for five years. His patience and encouragement got me through my difficult time. His immense knowledge and scientific rigor helped me develop my research abilities. I would like to extend my appreciation to my committee members: Prof. Bart Prorok, Prof. Dong-Joo Kim, Prof. Raj Amin, and Prof. Panagiotis Mistriotis for their time to review this work and invaluable comments. My gratitude also goes out to our collaborators, Dr. Feng Li, Prof. Weiqiang Chen, and Prof. Yubing Sun for the insightful guidance, intense discussion, and consistent engagement of our projects.

Besides, Steven Moore, William Ingram, and Cheryl Rhodes, I sincerely appreciate your constant availability to offer assistance whenever I required it. Thank you to all the members and alumni of Advanced Nanomaterials Engineering Laboratory: Dr. Lang Zhou, Dr. Zhuangqiang Gao, Dr. Jingyi Zhu, Dr. Jiacheng He, Dr. Wen Yang, Chuanyu Wang, Alana MacLachlan, Siqi Wu, Muammar Chang, Shuai Wu, Haichuan Wang, Karan Ingale, Sara Boyd, Lili Chen, Yuan Gao, Te Yi Hsiao, Yiming Cheng, Feng Xiong, and Zhengyang Gu. Without their assistance, my study would not have been possible. More important, without their company, my days and nights in the lab would not have been so joyful.

Additionally, I would like to express my gratitude to my friends, Tianyi Wang, Qi Han, Yi Luo, Xuetong Wei, Dr. Xingxing Zhang, Cheng Chen, Eileen Chen, Brooke DeGaris, Stephen Copper, Yanan Li, Xiangcheng Kong, Dr. Kian Orangi, Ya Chang, Dr. Wu Chen, Farshad Amiri, Dr. Qianman Peng, Dr. Huitong Shi, Xuejia Kang, Chunghui Huang, Junwei Wang, Qi Wang, Yoolim Cha, Jialiang Sheng, Mingyuan Chen, Ranlin Liu, Dr. Jiahui Xu, Dr. Ralf Fischer, Dr. Yuzhe Sun, Dr. Yuzhe Liu, Dr. Liangxi Li, Dr. Doohee Lee, Dr. Pu Deng, Dr. Haotian Wu, Jingfan Yang, Dr. Houshang Yin, Qingyu Pan, Weili Liu, Rukai Guo, and Dr. Xin Wei.

Last but not the least, I would like to express my deepest appreciation to my family, especially my parents, Liang Cai and Prof. Jing Tan, my partner Le Cai, and my two lovely dogs, Offer Cai and Roubaix Cai. Your belief in me and my abilities has been a constant source of motivation and inspiration. Without your support, I would not have been able to achieve this milestone.

Thank you from the bottom of my heart and War Eagle!

Table of Contents

List of Figures

List of Abbreviations

0D	0-dimensional
1D	1-dimensional
2D	2-dimensional
3D	3-dimensional
α-SMA	α-smooth muscle actin
AC	Alternating current
AMF	Alternating magnetic field
APC	Antigen-presenting cell
APTES	(3-Aminopropyl)triethoxysilane
ATP	Adenosine triphosphate
AuNR	Gold nanorod
AuNP	Gold nanoparticle
AuNS	Gold nano seed
BCG	Bacillus Calmette-Guérin
BSA	Bovine serum albumin
CAF	Cancer-associated fibroblasts

CAR	Chimeric antigen receptors
CD	Cluster of Differentiation
CIK	Cytokine-induced killer
CLSM	Confocal laser scanning microscopy
CNTs	Carbon nanotubes
COMSOL	Commercial multiphysics simulation software
CRT	Calreticulin
CTAB	Hexadecyltrimethylammonium bromide
DC	Dendritic cell
DDC-Na	Sodium diethyldithiocarbamate trihydrate
DI	Deionized
DLS	Dynamic light scattering
DMEM	Dulbecco's modified eagle medium
DNA	Deoxyribonucleic acid
DRIE	Deep reactive-ion etching
EC	Endothelial cell
ECM	Extracellular matrix
EDC	1-ethyl-3-(3-dimethyl aminopropyl)carbodiimide

EDL	Electric double layer
EDX	Energy-dispersive X-ray spectroscopy
EG	Ethylene glycol
EIS	Electrochemical impedance spectroscopy
ELISA	Enzyme-linked immunosorbent assay
EMCCD	Electron-multiplying charge-coupled device
EMT	Epithelial-mesenchymal transition
FACSNP	Fe_3O_4-Au core-shell nanoparticle
FBS	Fetal bovine serum
FDTD	Finite difference time domain
FET	Field effect-transistor
HBSS	Hank's balanced salt solution
HMGB1	High mobility group box 1
ICD	Immunological cell death
IFN-α	Interferon alpha
IFN-γ	Interferon gamma
Ig	Immunoglobulin
IL-2	Interleukin 2

IL-6	Interleukin 6
ITO	Indium-doped tin oxide
LOD	Limit of detection
LSP	Localized surface plasmon
LSPR	Localized surface plasmon resonance
LTC	Leukemia tumor cell
M0	Unpolarized macrophages
M1	Pro-inflammatory macrophage
M2	Anti-inflammatory macrophage
mRNA	Messenger ribonucleic acid
MALDI	Matrix-assisted laser desorption/ionization
MCP-1	Monocyte chemoattractant protein 1
MHC	Major histocompatibility complex
MHT	Magnetic hyperthermia therapy
MS	Mass spectrometry
NHS	N-hydroxysuccinimide
NK	Natural killer
NP	Nanoparticle

NS	Nanosphere
OOC	Organ-on-a-chip
PBS	Phosphate buffered saline
PC	Polycarbonate
PD-1	Programmed cell death protein 1
PD-L1	Programmed death-ligand 1
PDMS	Polydimethylsiloxane
PEG	Polyethylene glycol
PI	Propidium iodide
PLA	Polylactic acid
PMMA	Poly(methyl methacrylate)
PoC	Point-of-care
PS	Polysterene
PTT	Photothermal therapy
PVP	Polyvinylpyrrolidone
qPCR	Quantitative polymerase chain reaction
RNA	Ribonucleic acid
RPMI	Roswell park memorial institute

SAW	Surface acoustic wave
SCION	Superparamagnetic copper iron oxide nanoparticle
SELEX	Systematic evolution of ligands by exponential enrichment
SEM	Scanning electron microscope
SD	Standard deviation
SP	Surface plasmon
SPR	Surface plasmon resonance
STD	Standard deviation
TAM	Tumor-Associated Macrophage
TEM	Transmission electron microscope
TGF-β	Transforming growth factor beta
TIL	Tumor-infiltrating lymphocytes
TME	Tumor microenvironment
TNF-α	Tumor necrosis factor-alpha
TOC	Tumor-on-a-chip
UV-Vis	Ultraviolet-visible
WGM	Whispering-gallery-mode
XRD	X-ray diffraction analysis

List of Symbols

C_{ACS}	Absorption cross-section
I_{AuNP}	Absorption intensity from AuNP
$I_{background}$	Absorption intensity from the background
$\Delta I/I_0$	Fractional intensity change
I_0	Initial intensity
ΔI	Intensity change
k_{slope}	The slope of the linear regression
M	Molar
R	Regression coefficient
σ	Standard derivation of the background signal
Ω	Far-field domain
$\Delta S/S$	Differential scattering signal
ΔS	AC signal
V_0	Surface potential
ε_0	Electric permittivity of vacuum
d	Distance

d_{TF}	Thomas-Fermi screening length
N	Electron number density
e	Elementary charge
ω_P*	Gold plasma frequency
m*	Effective electron mass
ε_∞	Static dielectric constant
γ	Characteristic collision frequency
V	Volume of the particle
L	Geometrical factor
ε_D	Dielectric constant
c	Speed of light in vacuum
ħ	Planck's constant divided by 2π
Δλ	Spectrum shift
$\Delta T/\Delta\lambda$	Derivative of the transmission spectrum
$\Delta\lambda_{LSP}$	Wavelength shift in the resonance
V_s	Stern layer potential
d_S	Electrical double layer thickness
k_B	Boltzmann constant

T	Absolute temperature
N_i	Known bulk concentration of ions
z	Valence of the ions

Chapter 1

Introduction

1.1 Background and Motivation

1.1.1 Nanomaterials

Nanomaterials are characterized as materials that possess a nanoscale size or surface in at least one dimension, whereas nanoparticles are particles that have a size ranging from 1 to 100 nm in all three dimensions.[1] As a result, all nanoparticles fall under the category of nanomaterials, but not all nanomaterials can be classified strictly as nanoparticles. Multifunctional nanoparticles have elicited much interest due to their unique physicochemical properties to broaden their promising applications in sensing, immunoassay, cancer immunotherapy, and so on.[2] Because of their nanoscale size and high surface-to-volume ratio, materials' physical, chemical, and biological properties are different compared to their bulk counterparts.[3] Pokropivny *et al* categorized nanomaterials

based on the number of dimensions they have in the nanoscale range.[4] According to their classification, 0-dimensional (0D) nanomaterials consist of materials where all three dimensions are in the nanoscale range, including nanoparticles like nanosphere, nanorod, and nanocube.[5-7] On the other hand, 1-dimensional (1D) nanomaterials are materials with two dimensions in the nanoscale range,[8] such as nanofiber, while 2-dimensional (2D) nanomaterials are materials that have only one dimension in the nanoscale range, like MXene[9].

Nanomaterials can be categorized into different types based on their composition, such as carbon-based nanomaterials,[10] ceramics-based nanomaterials,[11] polymer-based nanomaterials,[12] lipid-based nanomaterials,[13] and metal-based nanomaterials.[14] Due to their appealing electrical conductivity, Graphene and Carbon nanotubes (CNTs)[15] are among the most widely recognized types of carbon-based nanomaterials. Inorganic ceramics-based nanomaterials have various applications in catalysis, as opposed to polymer-based nanomaterials which are typically composed of organic materials and function as matrix materials.[16] On the other hand, lipid-based nanomaterials usually have a solid core and are spherical in shape, and are currently being utilized for drug delivery and messenger ribonucleic acid (mRNA) vaccines.[17-19] Metal-based nanomaterials have been widely researched for their unique optical properties, with plasmonic nanoparticles such as gold nanoparticles and silver nanoparticles attracting significant attention in biosensing and photothermal therapy (PTT) due to their localized surface plasmon resonance (LSPR).[20-22] Moreover, Superparamagnetic nanoparticles represent one of the most appealing prospects because they can be conveniently aligned to form a matrix by applying an external magnetic field without retaining residual magnetism (no

agglomeration) after the removal of the field.[23,24] Iron oxide superparamagnetic nanoparticles were chosen by us as a candidate with potential because of their good biocompatibility.[25]

Plasmon refers to the collective oscillation of electrons in a metal relative to the immobile positive ions.[26] When confined to the surface of a metal, this phenomenon is referred to as surface plasmon (SP),[26-28] and in the case of a nanoparticle, it takes the form of localized surface plasmon (LSP).[22,29] LSP can be stimulated by electromagnetic radiation with a wavelength much greater than the size of the plasmonic nanoparticle, with the highest amplitude of oscillation observed at the resonant frequency.[30] It has two significant impacts: (i) the electric field intensity is highest at the surface of the nanoparticle and decreases exponentially into the surrounding medium; (ii) the absorption is maximized at the resonant frequency of the plasmon.[31,32] Thus, LSPs can be utilized in sensitive biosensing applications due to their sensitivity to changes in the local refractive index.[33] Unlike surface plasmon resonance (SPR), which detects changes in the bulk dielectric environment up to a range of 600-1000 nm, LSPR is less susceptible to the bulk effect and nonspecific bindings due to its decay length of several nanometers.[34,35] Additionally, LSPR necessitates less bulky optics in comparison to SPR, making it a viable candidate for point-of-care (PoC) applications.[36-38]

1.1.2 Biosensors and immunoassays

Biosensors are analytical tools that convert the presence of a biological or chemical substance into a detectable signal.[39-42] One example of a biosensor is an immunoassay,[43]

which uses antibodies to identify the concentration of macromolecules, usually proteins.[43-45] A typical biosensor consists of three primary components: a transducer, a bioreceptor, and an analyte.[46] The transducer functions as the detection element that converts a biorecognition event into a measurable signal.[47] The bioreceptor is an element that selectively identifies target molecules,[48] with antibodies being the most commonly utilized in immunoassays. Finally, the analyte is the substance of interest.[49]

After Leland reported the first-generation biosensor for measuring oxygen concentration in blood in 1956,[50] co-reactants were incorporated to improve the analytical performance in the second generation of biosensors,[51] and now, in the third generation of biosensors, receptors were incorporated into the sensing element. In 1983, Liedberg introduced the initial real-time surface plasmon resonance (SPR) biosensing platform.[52]

Biosensing platforms utilizing different detection methodologies have been reported, and they can be broadly classified as either label-detection methods or label-free detection methods.[53] A label detection method employs foreign molecules attached to the probe element to report the presence of target molecules.[54] Typically, it requires several labeling and washing steps, leading to an extended assay time. The "gold standard" method for protein detection, enzyme-linked immunosorbent assay (ELISA), would be a good example.[55] It requires secondary antibodies conjugated to enzymes. Following the binding between target proteins and secondary antibodies, the enzymes catalyze a substrate, leading to a color change.[56]

Similar to ELISA, fluorescent-based detection is frequently utilized in sandwich immunoassays,[57] where fluorescent dyes are attached to the secondary antibodies (also known as detection antibodies).[58] A so-called "sandwich structure" is formed when the

target molecule binds between the primary antibody and the secondary antibody, and fluorescent intensity is measured to determine the analyte concentration via a calibration curve.[59] However, this method is prone to false-positive signals resulting from molecular interaction disruptions and photobleaching.[60,61]

Chemiluminescent-based detection similarly translates binding events into light emission but differs from fluorescent methods as the luminescence produced arises from a chemical reaction, rather than from photon absorption.[62,63] During molecular relaxation to a lower energy state, one photon of light is emitted. Although chemiluminescent methods have been shown to detect analytes at low concentrations, they are limited by inefficient energy transfer.[64]

Electrochemical biosensors utilize electrical signals such as current, potential, and impedance to transduce biorecognition events.[65] Compared to mechanical biosensors, electrochemical biosensors generally demonstrate higher sensitivity.[66,67] However, real biological samples with high ion strength and diverse interfering molecules pose significant challenges to electrochemical biosensors.[68]

Amperometric biosensors measure current variation in a redox reaction and have been used for protein,[69] exosome,[70] and microRNA[71] analysis due to their simplicity, low cost, and ease of miniaturization. Nonetheless, the use of redox reactions typically requires an electron-transfer reagent, restricting its ability to record dynamic biological reactions.[72] Electrochemical impedance spectroscopy (EIS)[73] is a technique that measures the electrical impedance of an interface under steady-state alternating current (AC) and constant direct current (DC) bias conditions, imposing minimal damage to biological samples.[74,75] Recent advancements in 2D nanomaterials have led to field-effect-transistor (FET)-based

biosensors,[76] which are sensitive to local changes in electric properties.[76] Nevertheless, similar to other electrochemical sensors, FET-based biosensors are greatly affected by interfering molecules present in the sample.[77]

Mechanical-based biosensing is a rapid and label-free detection technique that measures surface deflection or resonance shift induced by surface stress or mass variation upon the interaction between the receptor and analyte.[77] The binding of the analyte can be swiftly detected and transformed into the signal response of a change in bending or vibration frequency. Microcantilever-deflection-based biosensors use microscale structures as physical, chemical, or biological sensors to identify changes in cantilever deflection resulting from weight variations on the surface.[77,78] In contrast, quartz crystal biosensing platforms detect variations in oscillation frequency resulting from changes in mass.[79] Another prevalent mechanical biosensor is the surface acoustic wave (SAW) biosensor,[80] which utilizes a propagating acoustic wave on the surface of a piezoelectric crystal, with mass changes of the crystal leading to frequency variations of the applied wave.[81,82]

Similarly, but label-free, mass spectrometry (MS) is a highly sensitive and high-throughput technique that detects ionized analytes based on their mass-to-charge ratio.[83] Initially, MS was limited to detecting small molecules as there was no effective method to ionize samples noninvasively.[84,85] However, this obstacle was overcome by the development of matrix-assisted laser desorption/ionization (MALDI).[86] Currently, MALDI-based MS is widely used in proteomics and metabolite analysis.[87,88]

General optical biosensors, convert biorecognition events into light signals, such as resonance wavelength or light intensity,[89] enabling the direct detection of various chemical

and biological substances.[90] Photonic crystals are periodic nanostructures made of dielectric materials that trap light with a specific wavelength in a confined small volume by reflection.[91] Deposition of target analytes on photonic crystal results in local disruption of the periodicity and symmetry of the crystal, inducing a change in reflection wavelength.[92] Photonic crystal biosensors typically exhibit high sensitivity because of the high-quality factor of the perfectly arranged structure.[93] In contrast, whispering-gallery-mode (WGM) based biosensing platforms use light confinement within a glass sphere through continuous total internal reflection.[94] Resonance occurs when the optical path length is an integer multiple of the wavelength, resulting in a dip in the transmitted light intensity. The binding of target molecules to the sphere increases the path length, which can be characterized by a redshift at a given resonant frequency.[95,96]

Our study focuses more on the plasmonic biosensor, one of the most widely used optical biosensors.[97] During the plasmonic biosensor's development, SPR was the primary plasmonic biosensing platform, which generated a propagating evanescent wave sensitive to refractive index variations on the metal surface.[98,99] Currently, SPR techniques are widely used to study bio-molecule surface binding, analyte-antibody binding affinity, protein-protein interactions, and cell detection.[100] The conventional Kretschmann configuration is commonly used for SPR biosensors, which require bulky optical equipment, making system miniaturization a significant challenge.[101] Furthermore, its evanescent field shows a greater depth of penetration, therefore being susceptible to the non-specific binding and bulk effect. Unlike SPR, LSPR occurs at the interface between a noble nanoparticle and its surrounding medium when illuminated by light at a specific

wavelength.[22,102] As the electric field is significantly enhanced on the nanoparticle surface, LSPR is highly sensitive to local changes in the refractive index.[103]

In our study, LSPR-based detection currently uses a label-free sensing approach where probe elements, such as antibodies or aptamers, are attached to the surface of the nanoparticle. The binding of the target analyte results in a local change in refractive index and triggers a measurable optical signal, including a shift in resonance wavelength or a change in light intensity. Due to its outstanding sensitivity and simplicity of system miniaturization, integration, and multiplexing, the LSPR-based biosensing platform has the potential to be a promising candidate for next-generation POC immunoassay.[30,104]

1.1.3 Biorecognition elements

In a biosensor device, the biorecognition element is utilized to capture or bind the target analyte. A successful biosensor requires a strong binding affinity and selectivity between the biorecognition element and the analyte of interest. The commonly used biorecognition elements are antibodies, enzymes, nucleic acids, and aptamers.[30,105]

Antibodies are large proteins (~150 kDa) produced by the immune system to specifically recognize and neutralize foreign substances known as antigens. They have a Y-shaped structure with two identical heavy chains and two identical light chains.[106] In humans, antibodies can be categorized into five isotypes (IgA, IgD, IgE, IgG, and IgM) based on their heavy chain constant regions,[107] with IgG being the most abundant in the blood and commonly used in biosensing platforms.[108] Antibodies have millions of antigen-binding regions at the tips, allowing them to recognize a wide range of antigens with high

specificity.[109] Although antibodies have been widely used in biosensors due to their high affinity to the target molecule, their production often involves animals or cell cultures, making the process costly and laborious.[110-112] Thus, in recent years, there has been growing interest in the study of nanobodies, which are single-domain antibodies that lack a light chain and consist of only one variable domain located on a heavy chain.[113] Nanobodies are considerably smaller than traditional antibodies, with a size of 12-15 kDa, but they retain the same degree of recognition and exhibit improved stability.[114] Moreover, nanobodies can be produced on a larger scale and their monomeric structures can be genetically encoded, making them attractive candidates for advanced therapeutics and biosensing applications.[115]

Enzymes typically bind to target analytes through non-covalent interactions, such as hydrogen bonding and electrostatics, and produce signals through a biocatalytic process.[116] They capture and catalyze target analytes, converting binding events into measurable signals, such as electrical, optical, or thermal signals. To improve sensitivity, the signals can be further amplified.[117,118]

Nucleic acid probes, which can be either DNA or RNA molecules of varying lengths (ranging from short oligonucleotides to multigenic chromosomal segments),[119] are utilized to identify the presence of specific nucleotide sequences within microorganisms. Complementary binding motifs of DNA or RNA provide the binding specificity.[120,121]

Aptamers are small single-stranded DNA or RNA molecules that could selectively bind to target analytes, including proteins, peptides, carbohydrates, or live cells.[122,123] The specificity and binding capabilities of aptamers usually rely on their unique 3D folded structures formed after binding.[124] Aptamers are synthesized through an in vitro selection

process called Systematic Evolution of Ligands by Exponential Enrichment (SELEX).[125] SELEX is a combinatorial chemistry technique used to isolate single-stranded oligonucleotides with high binding affinity to target analytes.[126] The process starts with the incubation of the target analyte in a pool of random oligonucleotide sequences. After repeated rounds of purification and amplification, only high-affinity aptamers are left and mass synthesized. Since their discovery, aptamers have gained significant attention in diagnostic and therapeutic fields due to their high stability, low immunogenicity, ease of chemical modifications, and mass production capabilities.[125,126]

1.1.4 Cancer immunotherapy

Though significant efforts have been made to combat cancer, it remains one of the deadliest diseases, primarily due to cancer metastasis, which is a major contributor to the high mortality rate among cancer patients.[127,128] Due to the heterogeneity of metastatic cancers and the challenges of treatment, chemotherapy is currently the main clinical solution.[129] However, it is limited by toxic side effects and the emergence of drug resistance.[130] Cancer immunotherapy that elicits a lasting and adaptable immune response in patients with metastatic cancer is becoming an increasingly promising approach.[131-133]

Immune checkpoint blockade therapy is a type of cancer immunotherapy that blocks proteins known as checkpoints, which are produced by some immune system cells such as T cells and certain cancer cells.[134,135] These checkpoints play a role in regulating the strength of immune responses and can sometimes prevent T cells from attacking cancer cells.[136] By blocking these checkpoints, immune checkpoint inhibitors can help T cells to

more effectively attack cancer cells.[137] Checkpoint proteins found on T cells or cancer cells include PD-1/PD-L1 and CTLA-4/B7-1/B7-2.[138-143] Immune checkpoint inhibitors are commonly used in cancer treatment. This approach has achieved some level of clinical success in the treatment of cancer, but still, immune checkpoint therapy has only helped a limited number of patients due to inadequate immune system activation.[144,145]

T-cell transfer therapy is a form of immunotherapy that enhances the ability of the immune cells to attack cancer.[146] Two primary types of T-cell transfer therapy are tumor-infiltrating lymphocytes (TIL) therapy and chimeric antigen receptors (CAR) T-cell therapy.[147-150] Both involve collecting the patients' immune cells, amplifying them in the laboratory, and then reintroducing the cells back into the patient's bloodstream through needles in patients' veins. The process of growing the patient's T cells in the lab can take 2 to 8 weeks. During this time, the patient may have treatment with chemotherapy and, maybe, radiation therapy to get rid of other immune cells. Reducing the patient's immune cells helps the transferred T cells to be more effective. After these treatments, the T cells that were grown in the lab will be given back to the patient via an intravenous needle.[151,152]

TIL therapy utilizes T cells known as tumor-infiltrating lymphocytes, which are present in the patient's tumor. The medical team tests these lymphocytes in the laboratory to determine which ones most effectively identify the patient's tumor cells.[153] Afterward, the chosen lymphocytes undergo treatment with substances that promote their rapid multiplication.[153] The rationale for TIL therapy is those lymphocytes in or near the tumor have already demonstrated the ability to recognize your tumor cells, but there may not be enough of them to effectively kill the tumor or counteract the signals that the tumor uses

to suppress the immune system. Providing large numbers of the most reactive lymphocytes can help to overcome these challenges.[154,155]

In CAR T-cell therapy, T cells are collected from the patient and modified in a laboratory to produce a CAR protein that allows the T cells to recognize and bind to specific proteins on the surface of cancer cells. These modified T cells are then grown in large numbers and infused back into the patient to enhance their ability to target and kill cancer cells.[156] Monoclonal antibodies can be a form of immunotherapy as they aid in activating the immune system against cancer.[157] Some monoclonal antibodies function by tagging cancer cells so that the immune system can better identify and destroy them. For instance, rituximab is an example that attaches to the CD20 protein present in certain types of cancer cells and B cells, leading to their elimination by the immune system.[158] On the other hand, other monoclonal antibodies facilitate the process of bringing T cells closer to cancer cells, thereby increasing the efficacy of immune cells in killing cancer cells.[152,159]

Cancer treatment vaccines are a form of immunotherapy that aims to enhance the body's natural defenses against cancer.[159] The idea behind cancer treatment vaccines is that cancer cells contain tumor-associated antigens, which are not typically present in normal cells or are present at lower levels. Treatment vaccines help the immune system learn to recognize and respond to these antigens,[160] enabling it to destroy cancer cells. The cancer treatment vaccines can be generated from patients' tumor cells, tumor-associated antigens that are found on cancer cells, and patients' dendritic cells.[161-163]

Immune system modulators are a type of immunotherapy that could boost the body's immune response to fight cancer.[164,165] Immune system modulators include cytokines, Bacillus Calmette-Guérin (BCG), and immunomodulatory drugs.[166] Cytokines are low

molecular weight signaling proteins secreted by various cells, including macrophages, lymphocytes, and natural killer (NK) cells.[167] They play a key role in modulating the immune response of cells and regulating cell maturation and growth, therefore, they also play important roles in the immune system's ability to respond to cancer.[168] Interferon (IFN)-α and interleukin (IL)-2 are commonly used to treat cancer.[169,170] BCG is a weakened form of the bacteria causing tuberculosis. BCG will not induce disease in humans but can be utilized as an immunotherapy treatment for bladder cancer, where it is directly instilled into the bladder with a catheter to induce an immune response against cancer cells.[171] Moreover, ongoing research is being conducted to determine the potential of BCG in treating other types of cancer.[172]

1.1.5 Neural activities sensing

The mammalian nervous system contains billions of neurons that communicate with each other through quadrillions of synapses using electrical, chemical, and mechanical signals.[173,174] However, despite its vital role in biology, much about the brain's structures, functions, and connections remain unknown.[175] Neuroscience research has focused on studying the structure, function, and electrophysiological properties of neurons to uncover the mechanisms underlying brain function.[176] A comprehensive understanding of these mechanisms requires obtaining detailed information from various scales, ranging from molecules and individual cells to large brain circuits.[177] To investigate the collective behavior of large groups of neurons, it is necessary to monitor them on the millimeter to centimeter scale.[178] Conversely, to access the chemical and subcellular environment that governs the activity of individual neurons, it is crucial to investigate their nanoscale

environment. The manufacture of glass and silicon for microfluidics requires the use of advanced equipment and dangerous chemicals, making inorganic-based microfluidic devices costly to produce. Consequently, rigid polymers, such as poly(methyl methacrylate) (PMMA), have emerged as a popular alternative material for microfluidics.[179,180]

Currently, investigations into different scales are carried out on separate samples by utilizing distinct physical phenomena for sensing. However, there is a need for effective solutions that can enable simultaneous measurements at the scale of large neural networks.[181]

Traditionally, electrophysiological signals from networks of neurons have been detected by recording spontaneous or evoked electrical activity using multi-electrode array bio-devices.[182,183] On the other hand, the characterization of the neuronal molecular environment has been achieved using fluorescence optical spectroscopy or electrochemical methods that target specific molecules such as dopamine through oxidation-reduction reactions with carbon fiber electrodes.[183-186]

To address the need for combined measurements at multiple scales, Tsai-Wen Chen et al. introduced a novel class of highly sensitive fluorescence calcium indicators. These indicators are fast enough to detect individual action potentials, thus allowing for the correlation of electrical recording and fluorescence imaging for fast signals.[187-189] However, at the time of the study, this technology could only be used on cells with a gene expression of fluorescence indicators. As a result, the reported electrical fluorescence measurement was performed on only a few single neurons.[190]

Overall, the development of effective solutions that can enable simultaneous measurements at the scale of large neural networks could greatly enhance our understanding of neuronal activity and the molecular processes that underlie it. The continued advancement of technology in this area could ultimately lead to breakthroughs in the diagnosis and treatment of neurological disorders.

1.1.6 Microfluidics-based immunoassay and microenvironment

Microfluidics involves the manipulation of fluids that are confined to channels with dimensions at the microscale and encompasses both the science and technology of such systems.[191-193] Common materials used in microfluidics include rigid polymers, inorganic materials such as silicon, glass, and ceramics, as well as polydimethylsiloxane (PDMS). Silicon was the initial material of choice for microfluidics due to its well-established and extensively researched surface properties in the semiconductor industry. However, glass soon became the preferred material due to its superior optical transparency and biocompatibility.[30,105,194]

The manufacture of glass and silicon for microfluidics requires the use of advanced equipment and dangerous chemicals, making inorganic-based microfluidic devices costly to produce. Consequently, rigid polymers, such as poly(methyl methacrylate) (PMMA), have emerged as a popular alternative material for microfluidics. PMMA offers several benefits for microfluidics, including excellent optical transparency and ease of fabrication. However, PMMA-based microfluidic devices have not been successfully scaled up for mass production due to potential deformation during fabrication and high channel

roughness. As a result, PMMA-based microfluidics have remained limited to laboratory prototypes rather than industry-level production.[195] In this regard, PDMS has become the most popular material for microfluidics due to its low cost, optical transparency, biocompatibility, and ease of large-scale manufacturing. Recent advancements in microfabrication have further driven the growth of emerging microfluidic applications, including the development of biochips for point-of-care disease diagnosis, high-throughput sequencing, and single-cell manipulation.[196]

Microfluidic systems provide a powerful method for upstream sample processing, including the isolation, purification, concentration, and cultivation of specific cells for cellular analysis. These systems can create a biologically relevant microenvironment for cellular analysis, with a precisely controlled solution at a high spatial resolution. Furthermore, the flexible design of microfluidic structures allows for the isolation of individual cells from a larger population. This can be achieved by confining the cells to a functionalized microstructure surface, such as microwells, or by trapping and sorting target cells using force gradients generated by specially designed electromagnetic fields.[105,197]

Current microfluidics-based biosensors can be classified into (i) paper-based biosensing;[198] (ii) discrete microfluidics-based biosensing[199] and (iii) channel-based biosensing.[30,33] The use of paper-based microfluidic biosensors has generated significant interest due to their low cost, superior biocompatibility, and portability. The intrinsic porous structure of paper-based microfluidic devices enables capillary flow, which facilitates reagent storage, mixing, and reactions. Discrete microfluidics-based biosensing is an emerging technology that enables the dispensing of fluids into separate functional modules (microchambers). The isolation of each module is accomplished using an oil phase.

Channel-based biosensing is the most widely used of the three classes of microfluidics-based biosensors.[197] This method employs microchannels to define microscale flow regimes, and pumps are used to manipulate the continuous flow of fluids. Distinct functionalities, including sample pre-treatment, preparation, and analysis, are achieved by assigning them to different microchannels in microchannel-based microfluidics. In this study, we will integrate microchannel-based microfluidics into nanoplasmonic biosensing.

In addition to being used as a sensing platform based on microchannel-based microfluidics, microfluidic devices have also become an optimal platform for developing complex model systems that provide better-engineered microenvironments in cancer research and treatment. By cultivating microtissues within a microfluidic chip, researchers can create an organ-on-a-chip (OOC) microenvironment that offers a distinctive opportunity to replicate the structures and physiological conditions of human organs *in vitro*.[200,201] Like microchannels, soft lithography based on PDMS has become the most commonly used fabrication technique for OOCs due to its optical transparency, high biocompatibility, and ease of fabrication. In the soft lithography process, a silicon wafer is first coated with photoresist, exposed to UV light under a mask, and etched to create the mold of the OOCs. PDMS is then cast and solidified on the mold, and the designed microfluidic patterns are peeled off using a replica molding process.[197] Furthermore, injection molding is suitable for fabricating thermoplastic-based devices (such as polycarbonate (PC) and PMMA), excelling in mass production efficiency.[202] In recent years, 3D printing has emerged as a method for OOC fabrication due to its assembly-free process and ability to rapidly prototype complex structures with high design flexibility.[203,204]

Tumor-on-a-chip (TOC), which is a significant aspect of OOC, has gained considerable attention for producing functional 3D in vitro human tumor models for oncology research.[205,206] By reconstructing the tumor microenvironment (TME) on a chip with crucial cancer-associated cellular and non-cellular components, TOC enables the study of simulated *in vivo* tumor pathological processes, such as expansion, angiogenesis, metastasis, and interactions between tumor-stromal-immune cells in the TME.[207] The specific traits of the TME in TOC, including the biological gradient, niche factors, dynamic cellular interactions, and 3D configurations of the tumor and stromal cells, are particularly important in generating reliable, well-controlled preclinical models for studying tumor evolution, cancer-immune interactions, and developing novel chemo- and immune-therapies that conventional cell cultures or animal models cannot achieve.[208]

In general, TOC enables the recreation of a wide range of cellular and non-cellular TME features, such as multicellular interactions, biochemical properties based on the extracellular matrix (ECM), and biophysical cues such as hypoxia and its gradients.[209] Tumors, along with vasculatures, stromal cells, and immune cells, can grow on a chip with a complex tissue structure that is either self-organized or spatially arranged by design, mimicking their *in vivo* counterparts.[210] This outperforms 2D models and 3D tumor spheroids/organoids models in terms of complexity, physiological relevance, repeatability, and controllability. The primary cellular components in the TME include cancer-associated fibroblasts (CAFs),[211] which stimulate cancer cell invasion and proliferation, endothelial cells (ECs), which form vasculatures to promote tumor growth and metastasis,[212] and immune cells such as tumor-associated macrophages (TAMs), which assist tumor cells in escaping immune surveillance.[213] Non-cellular components in the TME, including

cytokines, growth factors, ligands, small RNAs, DNA, soluble factors, metabolites, and ECM, have been shown to direct interactions with cellular components and play a crucial role in shaping the tumor niche and promoting tumor progression.[214,215]

1.2 Dissertation Structure

This research presents a promising approach to improve cancer treatment by combining engineering and biology techniques to access immune profiles and tailor treatment based on individual responses. The work focuses on three key aspects: (1) rapid detection of certain biomarkers; (2) induce a certain immune response; (3) microenvironment fabrication *ex vivo*. The general background and motivation for the study are discussed in Chapter 1, while the specific projects aimed at addressing these critical issues are presented in Chapters 2 through 4. The study concludes by discussing the remaining challenges and future directions in Chapter 5.

In Chapter 1, we introduced the motivation of this study and discussed state-of-art techniques and knowledge on nanomaterials, biosensors, immunoassays, biorecognition elements, cancer immunotherapy, neuron activities, and microfluidic devices.

In Chapter 2, we demonstrated a high-throughput, label-free, multiplex immunoassay that accurately and sensitively analyzes multiple immune biomarkers rapidly. The magnet-assisted patterning method provides several benefits, including feasibility, flexibility, scalability, and cost-effectiveness, compared to other technologies for large-scale array fabrication. The multiplex immunoassay based on the patterned microarray can serve as a

powerful tool for routinely monitoring a wide range of biomarkers with rapid turnaround time and high statistical accuracy.

In Chapter 3, we demonstrated the potential of the multifunctional complex designed and synthesized by us as an effective therapeutic option for primary and metastatic tumor treatments. The unique combination of targeted delivery, magnetic thermal therapy, and immune therapy allows for the induction of cell death in primary tumor cells and the stimulation of systemic immune responses.

In Chapter 4, we demonstrated a 3D microneedle sensing arrays equipped with gold nanoparticles to detect neuron spiking activities through the LSPR optical detection method. The sensing structure enables the simultaneous realization of cell secretion and electrical signal transmission on a single chip, which offers high-resolution, real-time imaging, and information regarding the mammalian neuron system.

In Chapter 5, we concluded this work and showed the future direction of the research regarding precision medicine.

Chapter 2

Magnet Patterned Superparamagnetic Fe_3O_4/Au Nanoparticles as Plasmonic Sensing Array for Label-Free High Throughput Cytokine Immunoassay

2.1 Introduction

The ongoing revolution in fundamental immunology and clinical discovery is heavily dependent on the availability of diagnostic tools that can provide immediate, quantitative information at the bedside or in the clinic,[2] particularly for immune monitoring in practical medical treatment.[216] To determine the rapidly changing immune status of patients in various inflammatory disease conditions,[217] fast, accurate, and high-throughput analysis of multiple immune cells and secreted cytokines using a small sample volume is essential.[218,219] The current "gold standard" clinical technology, which is based primarily on ELISA, has several limitations, including complex labeling and washing processes that require up to 72 hours for the total assay time and a sample volume of 0.5-2 mL per test per patient, making it unsuitable for point-of-care immune monitoring.[220]

Label-free optical biosensing platforms, where the optical responses are measured in real-time without the need for secondary labeling, offer unique advantages in the rapid analysis of complex biological samples.[221] Among these techniques, inclusive of photonic crystal, optical ring resonator, surface plasmon resonance (SPR),[222] fiber optics, and interferometry, the nanoplasmonic biosensing based on the LSPR of noble metal NPs have shown exquisite levels of sensing performance.

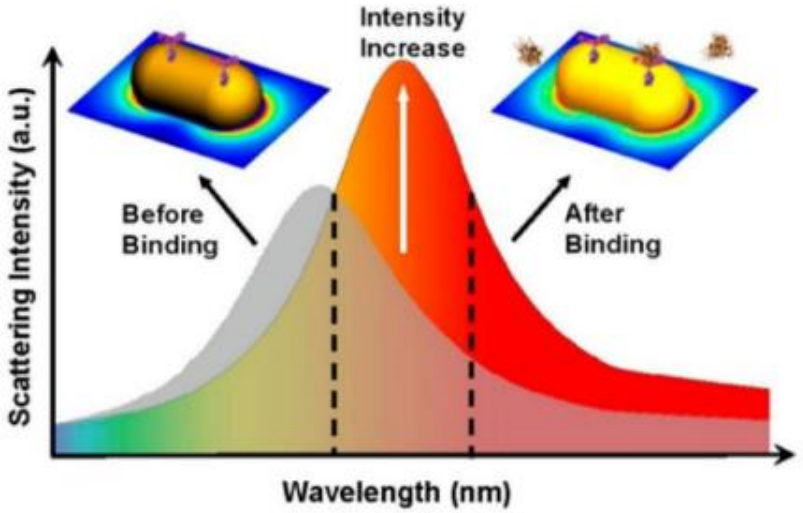

Fig.2.1 The schematic of the nanoplasmonic biosensing based on the LSPR.

Recent developments in nanotechnology and nanomaterials have led to the design and manufacture of next-generation nanoplasmonic biosensors with various nanostructures,[223] such as nanorods,[224] nano-bipyramids,[225] nanoflowers,[226] nano core-shell structures,[227] and nanohole arrays.[228] These nanoplasmonic structures offer considerable potential in sensor sensitivity, tuneability, miniaturization, high throughput capability, and large-scale fabrication.[229] The integration of these platforms into functional microfluidic devices has opened up new biological interfacing opportunities and shown promise for practical biomarker detection. However, the widespread adoption of these devices in real clinical

and pharmaceutical settings has been hindered by challenges in throughput and manufacturability, without compromising desirable sensitivity, multiplicity, and reliability.[230] While microarray nanoplasmonic sensing platforms have shown promise in the parallel quantification of multiple analytes,[231] the majority of these sensing arrays have been fabricated using electron beam lithography,[232] direct laser writing,[233] chemical electrodeposition,[234] or dip pen nanolithography.[235] These methods require specialized instrumentation and are costly, time-consuming, and not suitable for large-scale production.[236] Although a few high-throughput multianalyte nanoplasmonic sensing platforms are under development, addressing the challenges of cost, complexity, sensing performance, throughput, and scalability is critical for the widespread adoption of this technology in medical practice.[235]

2.2 Materials and methods

2.2.1 Design the high-throughput, label-free, multiplex LSPR immunoassay

An easy-to-implement, scalable nanoparticle surface patterning technique for generating regular-shape, well-dispersed, individual sensing spots over a large area is desired. Moreover, the strong plasmonic coupling afforded by the decorated gold nanoparticles will be able to support the need for superior sensitivity to the local refractive index change upon cytokine binding.

To achieve optimal optical sensing performance, we simulated the electric field distribution near the surface of AuNP embedded on the surface of an iron oxide porous structure upon interaction with the external electric field using commercial electromagnetic

simulation software, COMSOL Multiphysics. Critical factors such as AuNP size and AuNP shape play important roles in determining the plasmon resonance and scattering spectrum of the sensing particles needed for the ideal immunoassay (Figure 2.2).

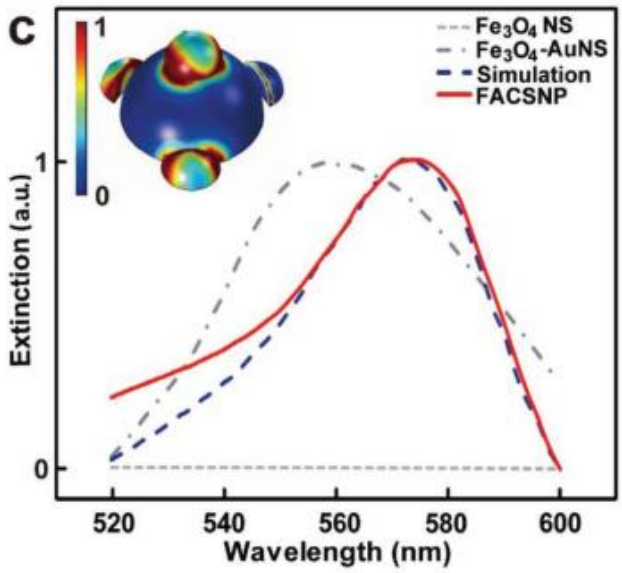

Fig.2.2 The simulated UV–vis spectra of Fe_3O_4 nanospheres, Fe_3O_4-Au nanospheres, and Fe_3O_4-Au core-shell NPs.

We performed a finite difference time domain (FDTD) simulation and predicted the scattering efficiency on a single FACSNP. The optical response of FACSNPs upon light excitation was simulated by the finite element method using COMSOL. The dimensions of Fe_3O_4 NS and the decorated AuNPs were determined based on the TEM results in Figure 2.5. The far-field domain was constructed as a semi-sphere and the perfectly matched layer with the same radius was set on the top of the far-field domain as the boundary of light. A polarized incident electromagnetic wave that was perpendicular to the wave vector was set. The absorption light intensity was evaluated by the absorption cross section C_{ACS}, which is the integration of the absorption wave intensity over the surface of far-domain Ω.

$$C_{ACS} = \int \frac{I_{AuNP}}{I_{background}} d\Omega$$

where I_{AuNP} is the absorbance intensity from the AuNPs and $I_{background}$ the background signal without the presence of AuNPs.

2.2.2 Synthesize and characterize the magnetic nano biosensing particles

The FACSNPs were synthesized according to the fabrication procedures as illustrated in Figure 2.3. Briefly, the monodisperse Fe_3O_4 nanospheres (Fe_3O_4 NS) were prepared by a modified solvothermal reduction method.[237] The Fe_3O_4 NS then functioned with 3-aminopropyl-triethoxysilane (APTES) to allow the covalent attachment of Au nano seeds (AuNS) on the Fe_3O_4 nanocore. Finally, the FACSNPs were formed through in situ seed growth by directly reducing the Au^{3+} on the Au nano seeds. We used cetrimonium bromide (CTAB) to modify the surface of our FACSNPs. This provided the core–shell structured Fe_3O_4 /Au nanoparticles with a positively charged surface showing a zeta potential of +46 mV (Zeta sizer Nano ZS90, Malvern).

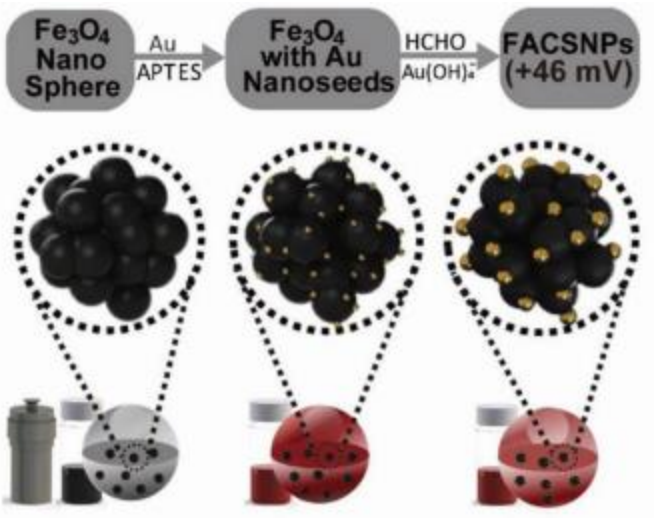

Fig.2.3 Synthesis process of the Fe_3O_4/Au core–shell NPs.

Figure 2.4 shows the representative scanning electron microscope (SEM) images of the obtained Fe_3O_4 NS, Fe_3O_4 NS decorated with AuNS (Fe_3O_4-AuNS), and FACSNPs. The Fe_3O_4 nanocore displayed a structure composed of a cluster of many small Fe_3O_4 nanoparticles with diameters around 20 nm as shown in the high-contrast dark part of the core region. The AuNS and AuNPs (bright dots circled in yellow of the SEM images) were immobilized on the surface of the Fe_3O_4 nanocore with sizes around 3–5 and 20 nm,[238] respectively. Multiple-crystalline porous structures were observed for the core–shell nanomaterial with an average diameter of 50–60 nm. We determined the composition (major elements: Fe, O, and Au) of the FACSNPs by energy-dispersive X-ray spectroscopy (EDX, bottom right panel of Figure 4). Characteristic spectra of Fe, O, and Au were observed in the plot, confirming the presence of the major elements in the FACSNPs. Other signature peaks in the EDX spectrum were resulted from the silicon substrate.

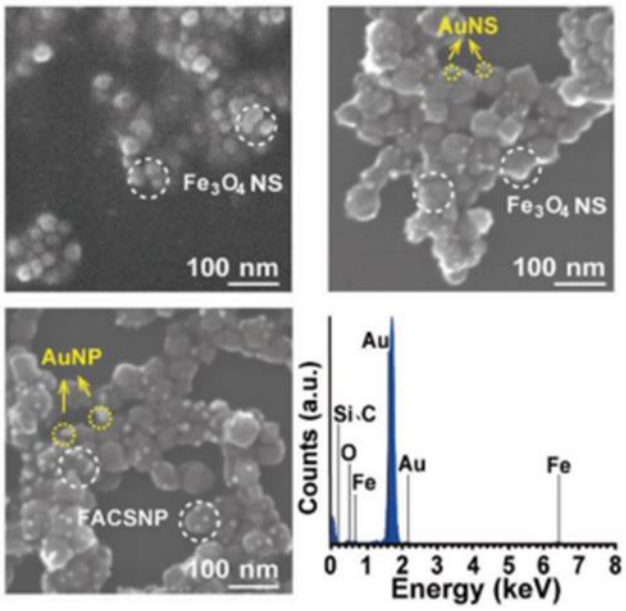

Fig.2.4 SEM images of Fe_3O_4 NS, Fe_3O_4-AuNS, and FACSNPs drop-cast onto a conductive silicon substrate. The element composition of FACSNPs was analyzed by energy-dispersive X-ray spectroscopy shown in the bottom right panel.

The CTAB coating on the FACSNPs resulted in a positively charged surface with a zeta potential of 46 ± 6 mV (Zetasizer Nano ZS90, Malvern). The transmission electron microscopy (TEM) was used to characterize the synthesized FACSNPs as shown in Figure 2.5.

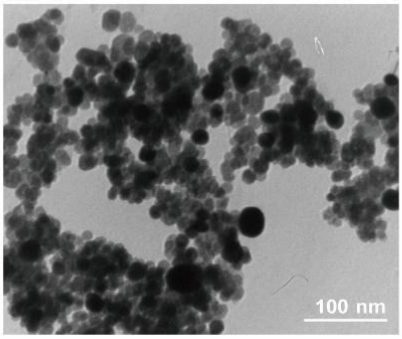

Fig.2.5 Transmission electron microscopy of FACSNPs drop-cast onto a glass substrate.

The dimensions of the FACSNPs and the decorated AuNPs were measured to be 60 ± 6 nm and 19 ± 2 nm, respectively (Figure 2.6).

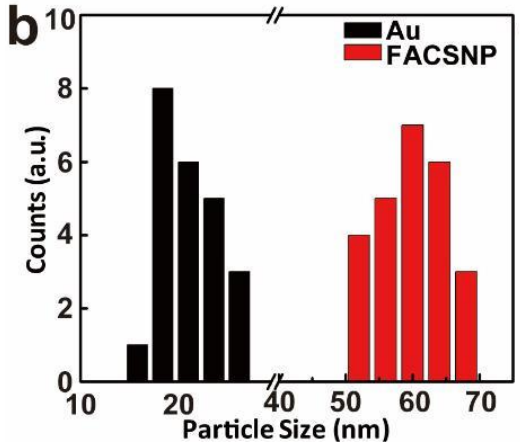

Fig.2.6 Statistics size distributions of the embedded gold nanoparticles and the FACSNPs measured from a high magnification of the TEM in Fig.2.5.

Figure 2.7 the XRD results of the diffraction spectrum of Fe_3O_4 nanospheres (NS). The sharp diffraction peaks were indexed to be (112), (211), (202), (220), (312), (303), (224), (332), and (143) Bragg reflections of crystalline cubic inverse spinel of bulk Fe_3O_4, respectively (JCPDS no. 75-1609).[237,239]

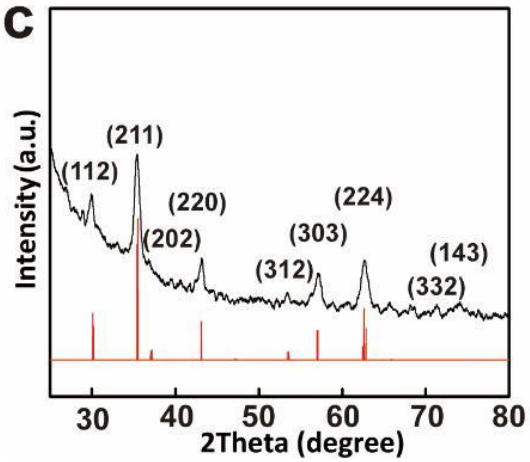

Fig.2.7 XRD spectrum of Fe_3O_4 NS.

We further examined the magnetism of Fe_3O_4 NS and FACSNPs by measuring the magnetic hysteresis loop using a vibrating sample magnetometer. The remanent magnetizations and coercivities were measured to be close to zero, which demonstrates that both the Fe_3O_4 NS and FACSNPs exhibited superparamagnetic characteristics. Modification of Fe_3O_4 NS with AuNPs slightly weakened the magnetization saturation value (Figure 2.8). But the FACSNPs can still be easily magnetized under an external magnetic field and demagnetized and redispersed immediately in the solution when the external magnetic field was removed.

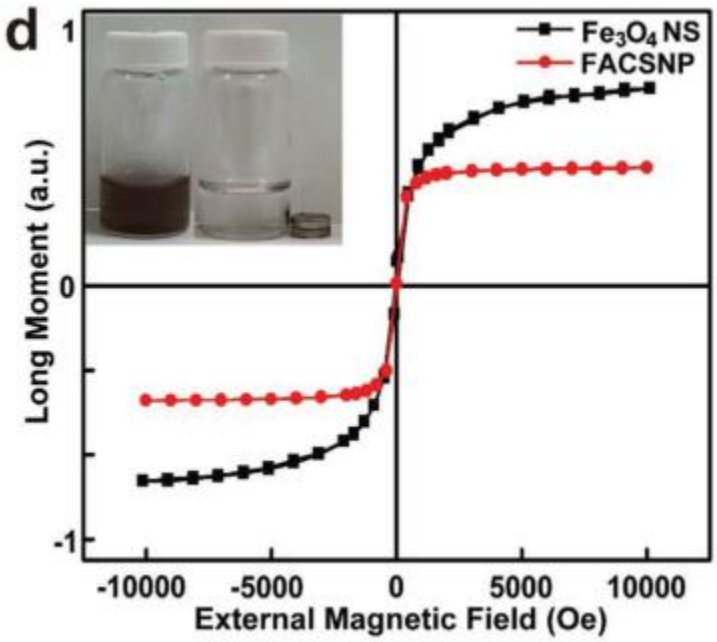

Fig.2.8 Magnetization curves of the Fe_3O_4 NS and FACSNPs, suggesting the superparamagnetic characteristics of the NPs. The inset figure shows the effect of the external magnetic field on FACSNPs in aqueous dispersion.

Figure 2.9 and 2.10 shows the effect of an external magnetic field on the FACSNPs under a dark-field microscope. When an external magnetic field was applied, the FACSNPs

can be magnetized and well aligned with the external magnetic field (Figure 2.9). The removal of the external magnetic field resulted in the immediate random dispersion of the FACSNPs (Figure 2.10). These observations are consistent with the magnetism measurement of the hysteresis loops, confirming the superparamagnetism of the FACSNPs.

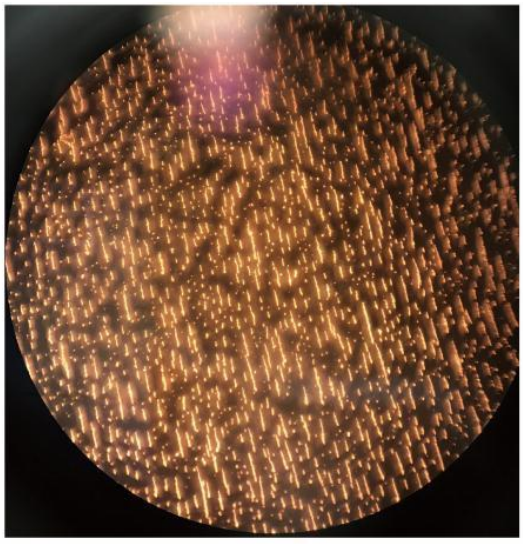

Fig.2.9 Dark field image of the FACSNPs drop-cast into the center of a glass substrate with an external magnetic field. The FACSNPs spontaneously lined up with the orientation of the magnetic field lines.

Fig.2.10 Dark field image of the on-glass FACSNPs right after the external magnetic field was removed, the FACSNPs immediately redispersed in the aqueous solution.

It should be noted that the conventional single-phase solid Fe_3O_4 NPs also exhibit superparamagnetic properties when the diameters of the NPs are in the range of 8.0–30 nm. However, this smaller NP size makes the growth of 20 nm AuNPs onto the core much less energy favorable as compared to the nanocore of FACSNPs ($\approx$60 nm) with a cluster of small Fe_3O_4 NS. As such, the entire FACSNPs afford both the superparamagnetic and strong plasmonic coupling characteristics, which allow tracking, manipulation, and patterning of the FACSNPs without losing the advantage of the stable colloidal suspension, rendering them a well-suited material for microarray plasmonic biosensor fabrication as shown below.

2.2.3 Magnet-Assisted Fabrication of the FACSNP Microarray

Using the physical and chemical properties of the FACSNPs that arise from both the intrinsic properties of constituent nanoparticles and their interparticle interactions, we adopted a magnet-assisted self-assembly process to pattern uniform antibody-functioned microarray on a glass substrate.

Figure 2.11 presents the schematics of the fabrication process. We first treated polydimethylsiloxane (PDMS) microwell mask (20 μm × 20 μm well size) and a glass substrate with oxygen plasma to make the surface hydrophilic and negatively charged. Two of the microwell-shaped PDMS masks were placed into a 3D-printed plastic frame to fix the pattern positions for subsequent antibody function and sample loading. FACSNPs (10 μL) dispersion was then dropped onto the plasma-treated PDMS masks and degassed for 25 min to ensure that all the microwells were fulfilled with the particle dispersion. The treated glass substrate was then attached to the FACSNPs-loaded PDMS mask. Ceramic magnets were mounted on the bottom side of the glass substrate to exert a strong magnetic force on the superparamagnetic FACSNPs in the microwells.

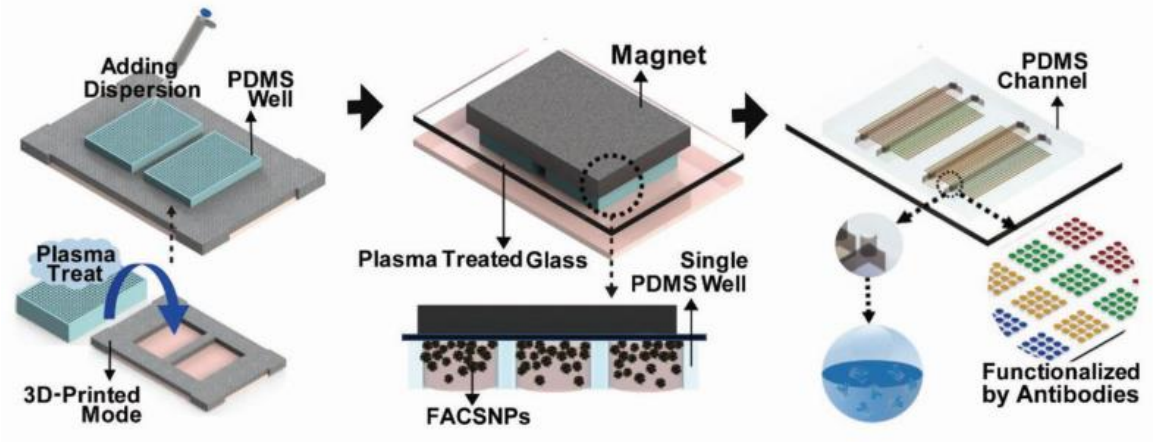

Fig.2.11 Illustrations of the magnet-assisted patterning process of the FACSNP microarray.

After overnight incubation, the positively charged FACSNPs were bound to the glass substrate by electrostatic attraction and assembled into uniform square-shaped microarrays over a large surface area as presented in the dark-field image (Figure 2.12).

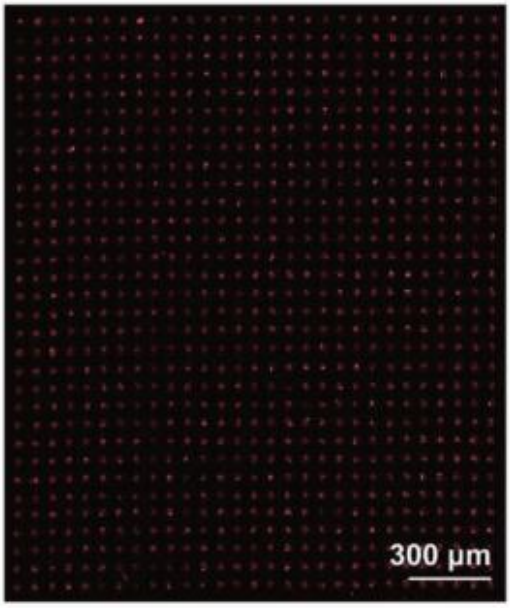

Fig.2.12 Dark-field microscopy images of the FACSNP microarray on the glass substrate. The FACSNPs confined in PDMS microwells self-assembled into a series of regular square-shape sensing spot arrays with the assistance of the external magnetic field.

Prior to the FACSNPs microarray fabrication, we first prepared PDMS microwell mask layers in both square and round shapes using soft lithography. The mold for the PDMS well-patterning mask was fabricated on a silicon substrate using deep reactive-ion etching (DRIE). The PDMS prepolymer (Sylgard-184, Dow Corning) was prepared by thoroughly mixing a curing agent with a base monomer (wt: wt = 1: 10) and poured onto the silicon mold, and cured in an oven at 65°C for 6 hrs. The cured PDMS mask layer was then peeled off from the mold to form a well-patterning mask layer. The layer was cut into multiple pieces for future use.

In order to precisely deposit the FACSNP microarrays on desired positions of the chip, we designed a 3D-printed polylactic acid (PLA) mold. A substrate was mounted into the 3D-printed mold to assist in the positioning of the PDMS masks later. Glass slides were first cleaned with Piranha solution (H_2SO_4:H_2O_2 = 3:1 v/v) for 10 min, rinsed thoroughly with deionized water, and kept in an ultrasonic bath with ethanol for 15 min. Then, the PDMS micro well-shape masks and a glass substrate were both treated with an oxygen plasma (Plasma Etch, Inc.) for 2 minutes. After plasma treatment, the PDMS masks became hydrophilic and allowed the proper wetting of the FACSNPs aqueous dispersion on the masks. The plasma-treated glass substrate turned to negatively charged owing to the dissociated hydroxyl groups existing on the glass, which can interact with the positively charged CTAB-coated FACSNPs and immobilize them on the surface. After that, the micro well-shape PDMS masks were mounted into the 3D-printed plastic mold. The plastic mold was detached after the PDMS mask positions were fixed. Each area of the plasma-treated PDMS masks was filled with 3.5 μL of FACSNPs dispersion. Then, the whole device was degassed in a vacuum desiccator for 25 min. The excessive FACSNP aqueous dispersion

on the surface of the PDMS masks was removed after degassing.[240] The plasma-treated glass substrate was then attached to the FACSNPs-loaded PDMS microwell layer. Strong ceramic magnets were fixed on the other side of the glass substrate to attract the FACSNPs to the glass surface. The whole device was incubated in a humid environment overnight. After incubation, the magnet and the PDMS masks were removed. The fabrication processes were shown in detail in Figure 2.13.

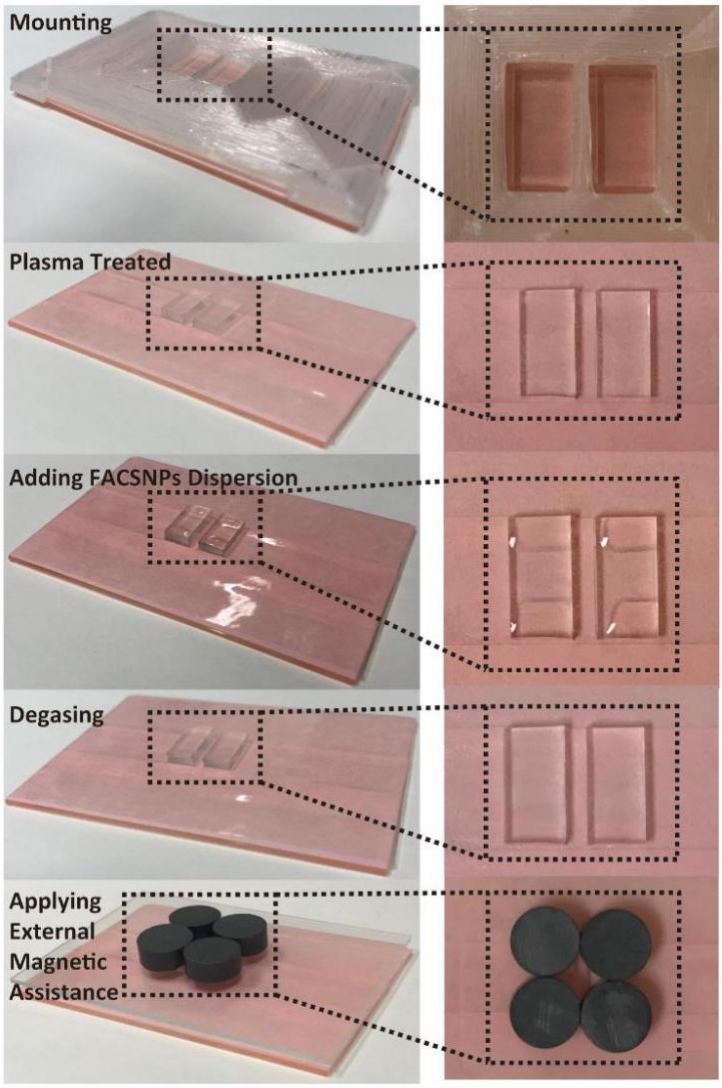

Fig.2.13 Photographs showing the detailed fabrication processes of the magnet-assisted patterning of FACSNP microarray.

We compared the patterning quality of the FACSNP microarray with and without the magnets as shown in Figure 2.14 and Fig. 2.15. The magnet-assisted patterning of FACSNP microarray showed clearly better uniformity on the shape and intensity of the array spot. Without the external magnetic field, aggregations, unfilled patterns, and "coffee-ring" shapes of the FACSNPs were observed on the glass substrate after overnight incubation. PDMS masks with different dimensions and geometries of the microwells were also used for creating different FACSNP microarray patterns. We obtained nicely patterned microarrays with the square shape of 20μm × 20 μm (spot-to-spot distance = 40 μm, Figure 2.14), mini square shape of 15 μm × 15 μm (spot-to-spot distance = 25 μm, Figure 2.16) and round shape of 40 μm in diameter (spot-to-spot distance = 60 μm, Figure 2.17). These results demonstrate the tunability and scalability of our magnet-assisted patterning technique for FACSNP microarrays.

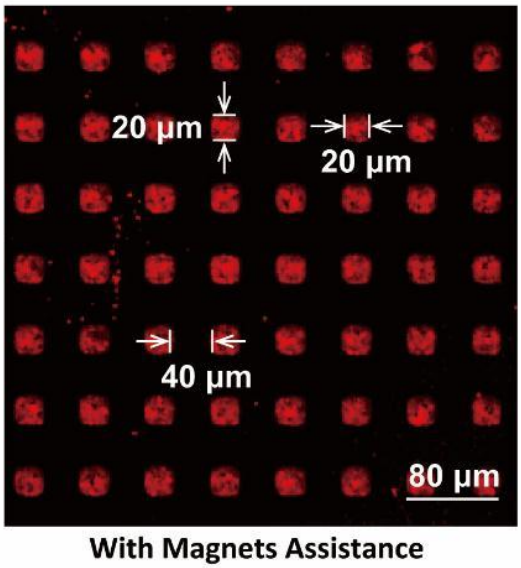

Fig.2.14 Dark field image of the sensing spots pattern formed with the magnet's assistance.

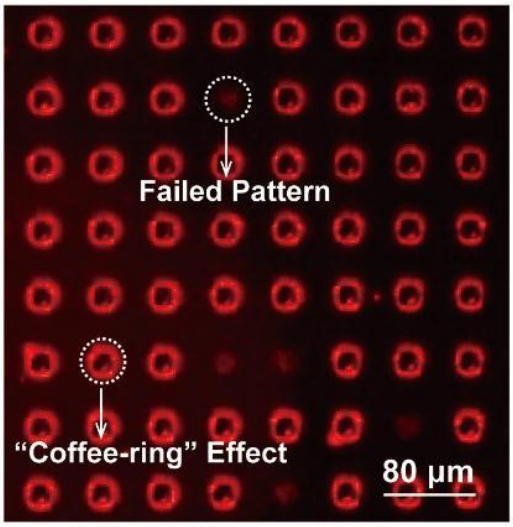

Fig.2.15 Dark field image of the sensing spots pattern formed without magnets assistance.

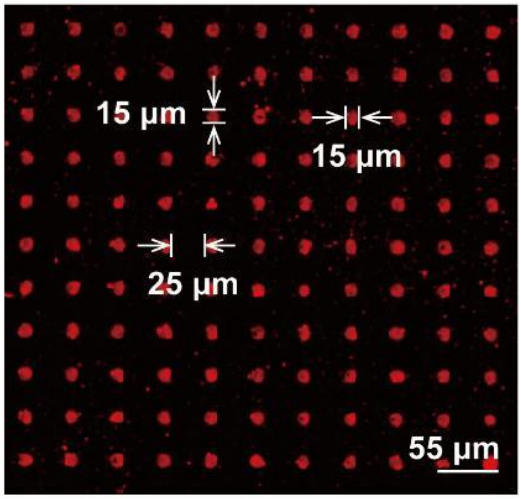

Fig.2.16 Dark field image of mini square-shape biosensing spots arrays.

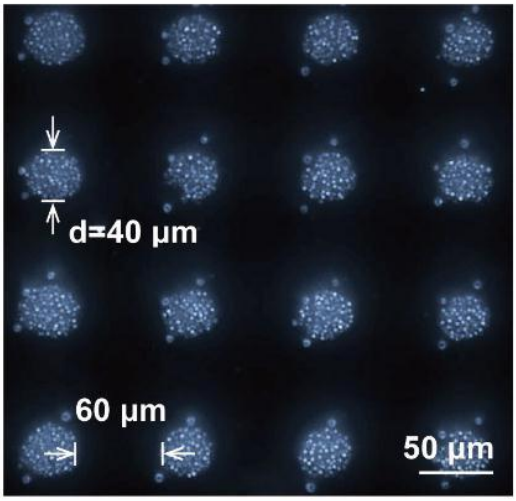

Fig.2.17 Dark field image of the round-shape patterned sensing spots, in which the FACSNPs dispersed uniformly.

Here, the magnet served as a concentrator that significantly enriched the local concentration, thus increasing the binding possibility of the FACSNPs to the glass substrate and avoiding the "coffee ring" effect. The release of the magnetic field allowed the redistribution of the FACSNPs owing to the superparamagnetic characteristic. As a result, we obtained a clearly better pattern quality of the FACSNPs with the magnet, showing a much stronger scattering intensity under dark-field imaging with regular microarray shapes (Figure 2.18) and well-dispersed particle deposition as shown in Figure 2.18, 2.19.

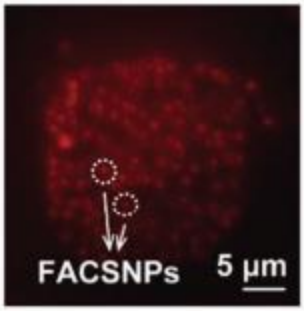

Fig.2.18 Dark-field microscopy image of individual FACSNPs biosensing spot at higher magnification, showing the well-dispersed FACSNPs immobilized in the sensing spot.

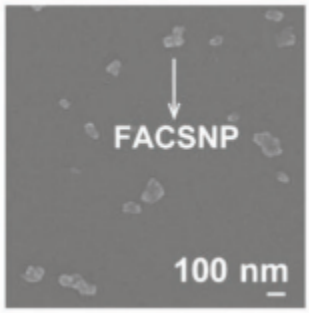

Fig.2.19 SEM image of the FACSNPs before antibody function.

Following the microarray patterning, we functionalized the FACSNPs with a panel of four cytokine antibodies using parallel microfluidic channels. The detailed function steps based on standard EDC/NHS chemistry are described in the Materials and Methods. The functionalized FACSNPs were imaged under SEM showing a thick layer of antibody coating on the NPs (Figure 2.20).[241,242]

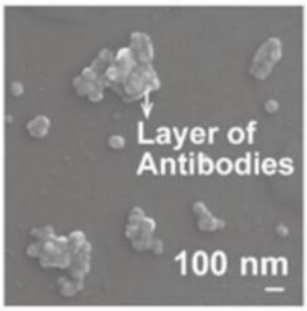

Fig.2.20 SEM image of the FACSNPs after successful antibody attachment

We further confirmed the antibody functionalization by measuring the zeta potential on the aqueous suspensions of the FACSNPs before and after the process. The functioned FACSNPs showed a neutralized zeta potential of +15 mV, indicating a partially coated surface of the FACSNPs with the antibodies. The successful antibody functionalization yielded four physically separated sensing regions with each consisting of large numbers of microarray sensors targeting specific cytokines.

This permits the multiplex detection of four cytokines in a massively parallel manner with high statistical accuracy. It should be noted that the shape, dimension, periodic distance, pattern area, and the number of target analytes of the microarray biosensor can be readily tuned by changing the design of the PDMS suggesting excellent flexibility, scalability, and manufacturability of our fabrication technique.

2.3 Results and discussion

2.3.1 FACSNP Microarray Imaging and Calibration for Label-Free High Throughput Cytokine Detection

The clinical and immunological relevance of cytokine detection requires real-time, high throughput, and sample-efficient analysis while simultaneously achieving a low limit of detection (LOD). To provide such discriminatory power for valuable clinical outcomes, we integrated our previously developed LSPR dark-field imaging technique with the FACSNP microarray biosensor into an optofluidic immunoassay for rapid, sensitive, and high throughput detection of cytokines in real biological samples. The optical setup and the principle of LSPR microarray imaging are illustrated in Figure 2.21.[241]

Briefly, the prepared FACSNP microarray chip was mounted on a standard darkfield microscope (Nikon Eclipse Ni-U). The binding of the analyte cytokines onto the FACSNPs induces an increase in the intensity and a spectral red shift of the scattering light. The collective light intensity shift was then recorded in real time by an electron-multiplying charge-coupled device (EMCCD) camera. A customized MATLAB program was used to automatically select the regions of interest through an edge detection/background subtraction algorithm and quantify the intensity change for each microarray sensing spot.[243]

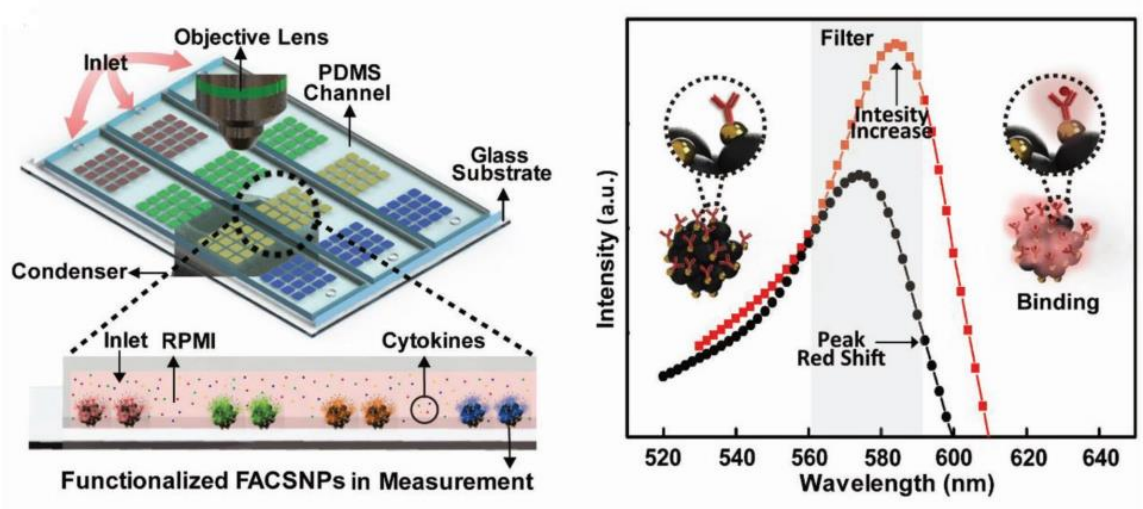

Fig.2.21 Schematic of the dark-field microscope setup for FACSNP microarray imaging. The prepared microarray chip was fixed on the motorized stage with the other side in contact with the dark-field condenser via silicon oil. A sample was injected from the inlet of the PDMS channel covered on the prepared pattern, flown through the sample channel, and collected from the outlet. Different cytokines in the sample were captured by the antibody-conjugated FACSNPs on the microarray. The light scattered from the FACSNPs was collected by a 20× objective lens and imaged by the EMCCD. The right panel shows the principle of FACSNP microarray imaging. The binding of specific cytokines onto the FACSNP results in an intensity increase and a spectrum red-shift. [241]

The intensity-based LSPR microarray imaging provides unique advantages over the traditional plasmonic biosensors based on spectrum-shift detection schemes. The obtained optical signals from the assembled microarrays contain statistical information over a large amount of the FACSNPs, which minimizes the variances in particle structure and spatial distribution. This distinct feature of LSPR microarray imaging offers unprecedented opportunities for high throughput immunoassay with inherently excellent statistic accuracy.

As such, we first performed the calibration of the FACSNPs microarray chip through parallel detection of four different cytokines: interleukin-6 (IL-6), monocyte chemoattractant protein 1 (MCP1), tumor-necrosis-factor alpha (TNF-α), and transforming growth factor beta (TGF-β) in Roswell Park Memorial Institute (RPMI) cell culture medium.

To validate the multiplex sample measurement capability of the microarray immunoassay that can specifically detect target cytokines in a complex biological medium, we performed measurements on a set of samples with each containing only one specific type of the cytokines (IL-6, MCP-1, TNF-α, TGF-β) at the concentration of 1000 pg/mL. As shown in Figure 2.22, we found no statistically significant difference between the measured cytokine concentrations and their expected values of 1000 pg/mL.

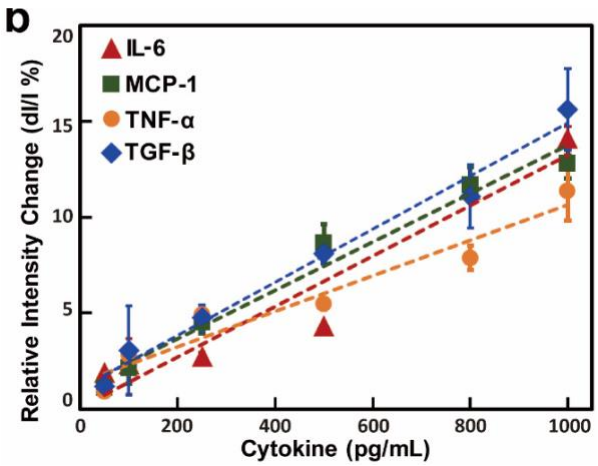

Fig.2.22 Calibration curves of IL-6, MCP-1, TNF-α, TGF-β obtained from the FACSNP microarray immunoassay.

Furthermore, most of the sensors targeting cytokines absent in the mixture yielded signals below the limit of detection as anticipated.

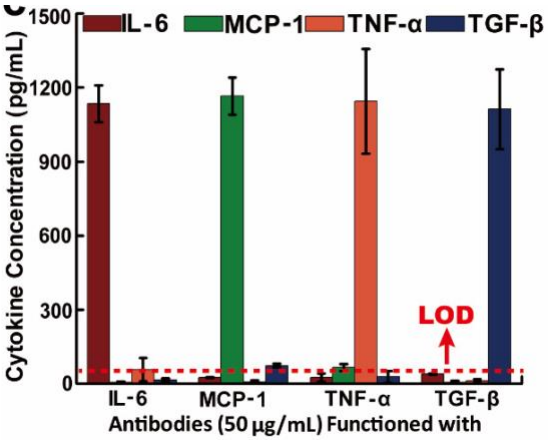

Fig.2.23 The selectivity of multiplex microarray immunoassay measured in cytokine concentrations. The red dashed line is the limit of detection of our FACSNP microarray immunoassay. Data were presented as the mean ± SD (n= 3).

The spiked samples with known concentrations (50, 100, 250, 500, 800, 1000pg•mL^{-1}) of cytokines were loaded into the sample loading channels and the quantified signal changes of the microarrays were translated into intensity maps as shown in Figure 2.24.

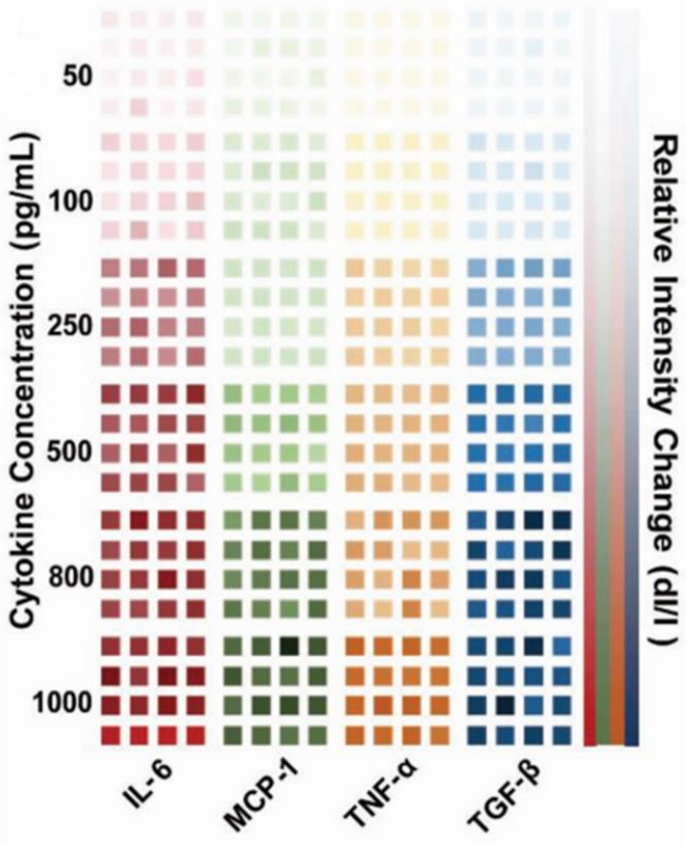

Fig.2.24 Mapping of intensity variations of FACSNP microarray for four different types of cytokines (IL-6, MCP-1, TNF-α, and TGF-β) at different concentrations.

Here, we selected a 4 × 4 sensing array for each cytokine and recorded the real-time intensity shift of all the sensing spots in one sample channel. Thus, we can simultaneously acquire 64 real-time binding curves for four cytokines in one loading channel and achieve a total number of 384 (64 × 6) measurements for the whole immunoassay. The sensing matrix can be easily scaled up by increasing the number of sensing arrays and sample loading channels. We established the calibration curves for each cytokine based on the concentration-dependent fractional intensity change ($\Delta I/I_0$). The intensity shift ($\Delta I/I_0$) was averaged over the 16 LSPR sensing microarrays by calculating the signal difference before (I_0) and after ($I_0 + \Delta I$) the sample incubation. We further determined the LOD as defined

by $3\sigma/k_{slope}$, where σ is the standard derivation of the background signal of the control medium and k_{slope} is the slope of the linear regression of each calibration curve. The calculated LODs for the four cytokines were 18.96 pg•mL^{-1} for IL-6, 14.57 pg•mL^{-1} for MCP-1, 32.62 pg•mL^{-1} for TNF-α, and 22.08 pg•mL^{-1} for TGF-β. As a result, our FACSNP microarray immunoassay shows comparable sensing characteristics in terms of sensitivity, assay time, and sample volume to the most state-of-art LSPR biosensors, while offering unique advantages in selectivity, throughput, and manufacturability toward practical applications.[244]

2.3.2 FACSNP Microarray Immunoassay for Functional Immunophenotyping of TAM

TAMs are the most prominent immune cells in the tumor microenvironment composed of leukocytes, fibroblasts, and vascular endothelial cells. They play a vital role in non-resolving inflammation in the tumor microenvironment, which is known as a hallmark of cancer.[245]

In general, macrophages show a high degree of plasticity in response to local environments and can be polarized into pro-inflammatory (M1) or anti-inflammatory (M2) macrophages. The M1 phenotypes are well adapted to promote a strong immune response by secreting high levels of pro-inflammatory cytokines. In contrast, the M2 phenotypes are activated by T helper cell 2 and tumor-derived cytokines (IL-4, IL-10, and IL-13), which are well-suited for the promotion of proliferation, invasion, and angiogenesis of tumor cells and thus the tumor development (Figure 2.25).

With the unraveling relationship of the apparent dual nature of macrophages to tumor development, the M2-like TAMs are now being recognized as potential diagnostic biomarkers and therapeutic targets for cancer.

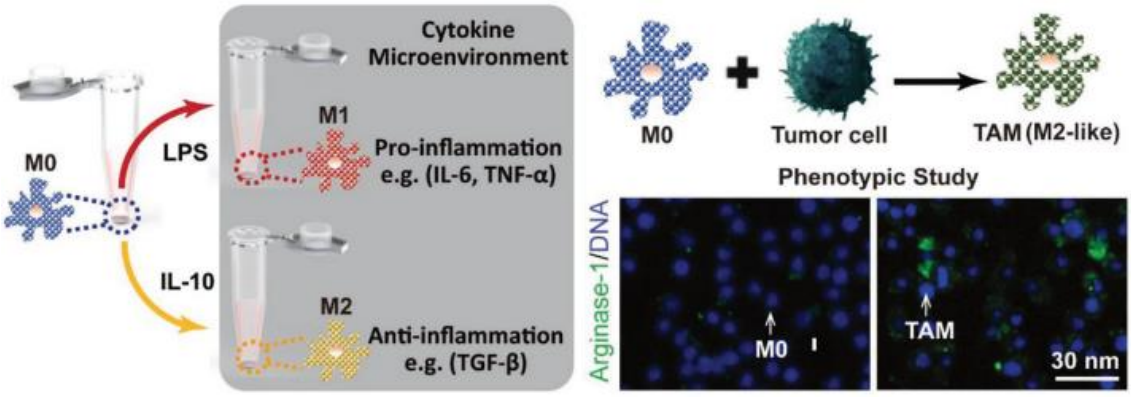

Fig.2.25 The schematics of macrophage polarization under different stimulation conditions. The right panel shows the transformation of the macrophages into M2-like TAMs after exposure to a biomimetic tumor microenvironment.

To explore the practical use of our FACSNP microarray immunoassay for clinical diagnosis, we performed the functional immunophenotyping of macrophages exposed to the leukemia tumor cell (LTC) microenvironment. Here, we measure the cytokine secretion profiles of macrophages under stimulation or treatment using LTC-conditioned media (Figure 2.26). The original unpolarized macrophages (M0) expressed no significant secretion for pro-inflammatory cytokines (IL-6 and TNFα) and anti-inflammatory cytokine TGF-β. The stimulation with lipopolysaccharides (LPS) turned M0 into the M1 phenotype macrophages, where strong IL-6 and TNF-α expressions were observed in the cell culture medium with a negligible amount of TGF-β released. In contrast, the M2 phenotype macrophages polarized by IL-10 showed a significantly increased concentration of anti-

inflammatory cytokine (TGF-β) expression, while the inflammatory responses by IL-6 and TNF-α secretion were largely suppressed. The macrophages treated with LTC-conditioned media displayed a similar cytokine secretion profile with that of M2 macrophages, indicating their transformation into M2-like TAMs. The measurements of LTC-conditioned media showing low levels of all cytokines further confirm that the measured TGF-β and MCP-1 were secreted by the polarized TAMs. Here, the MCP-1 is known as a potent chemotactic factor for monocyte trafficking and thus was detected in all the macrophage culture media. The relatively higher level of MCP-1 released by M2 and TAMs could be attributed to the promoted macrophage recruitment in the tumor microenvironment.

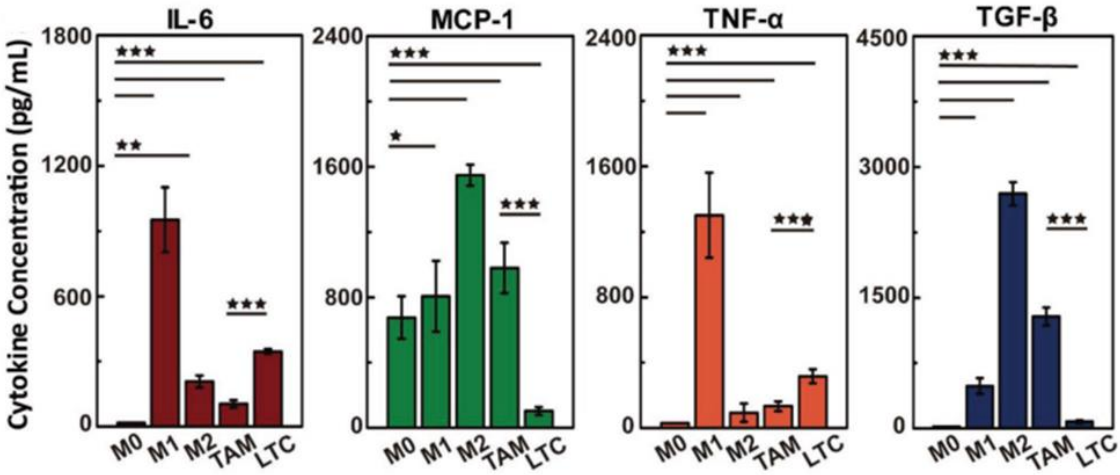

Fig.2.26 Cytokine secretion profiles of macrophages after treatment in different polarization conditions. M0 denotes the unpolarized, original macrophages. M1 is the original macrophage treated with 100 ng mL^{-1} of LPS for 48 h. M2 is the original macrophage treated with 100 ng mL^{-1} of IL-10 for 48 h. TAM presents the macrophages polarized by the leukemia tumor condition (LTC) culture medium. The cytokine concentrations were quantified by measuring the cell medium samples (n = 3) using the

FACSNP microarray immunoassay. Data were presented as mean ± SD. p Values were calculated using the One-Way ANOVA, *$p < 0.05$, **$p < 0.01$, ***$p < 0.0001$.

To validate the results obtained from the FACSNP microarray immunoassay with the existing "gold-standard" assay – ELISA, we performed ELISA-based measurements for the same cell medium samples (M0, M1, M2, and TAM). The ELISA-based measurements were based on the singleplex scheme. In other words, the assay targeted only one of the four cytokines in each measurement to avoid any potential crosstalk between different probe molecules. We repeated the singleplex ELISA measurements for all four cytokines across the prepared serum samples. Finally, we compared the results generated from both methods as shown in Figure 2.27. It should be noted that the measured cytokine concentrations from the FACSNP microarray immunoassay were smaller than those obtained from ELISA. This could be due to the degradation of the cytokines in the real samples during sample shipment and transportation. We believe that a side-by-side validation measurement would be ideal for probing the accuracy and reliability of the FACSNP microarray immunoassay.

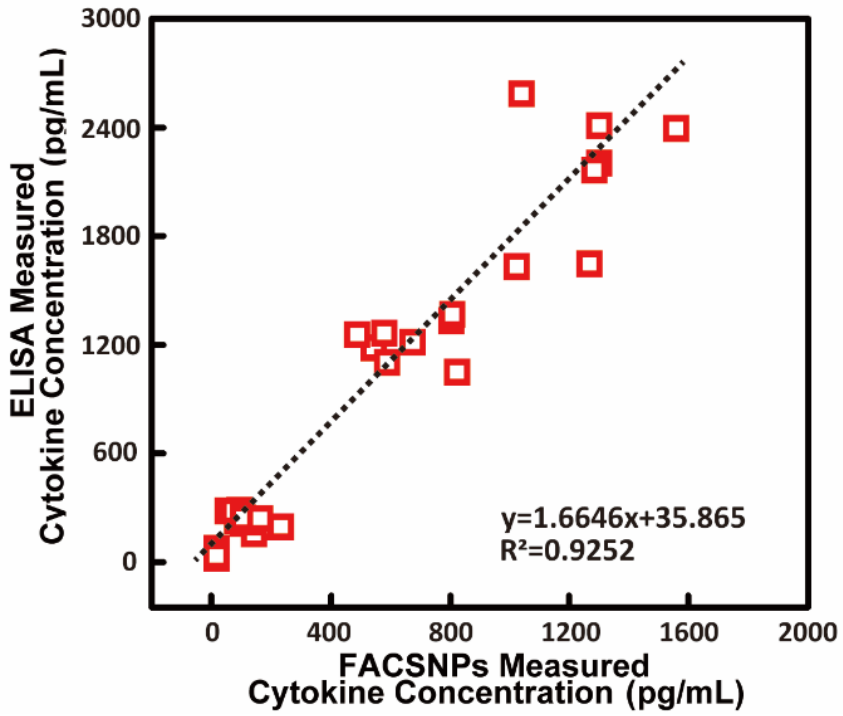

Fig.2.27 Correlation between results obtained from our FACSNP microarray immunoassay measurements and the ELISA for the cell medium samples.

All the results obtained from the FACSNP microarray immunoassay were validated by the singleplex ELISA for all four cytokines across the cell medium samples prepared above. An excellent linear correlation (R^2 = 0.9252) was obtained between the results measured by both methods. As such, the FACSNP microarray immunoassay showed discriminative power for immunophenotyping of macrophages in a biomimetic tumor environment, which could be potentially applied as a rapid and high throughput method for point-of-care clinical cancer diagnosis.

2.7 Conclusion

In conclusion, we have demonstrated a high-throughput, label-free, multiplex immunoassay that enables the analysis of multiple immune biomarkers in a rapid, accurate, and sensitive manner. The key to the success of this platform is by synergistically utilizing both the superparamagnetic and nanoplasmonic properties of the FACSNPs for large-scale array patterning and high-throughput sensing. The magnet-assisted patterning approach shows great advantages over many other technologies for large-scale array fabrication in terms of feasibility, flexibility, scalability, and cost-effectiveness. The multiplex immunoassay based on the patterned microarray can generally serve as a powerful tool for routinely monitoring a wide variety of biomarkers with rapid turn-around time and high statistic accuracy, which can be readily implemented for point-of-care clinical diagnosis. This platform possesses unique characteristics that do not exist with currently available technologies in clinical settings, which can be further expanded by integrating with nano- and microfluidic systems to provide multiscale measurements from whole-blood level to single-cell level for comprehensive functional analysis of the immune system.

Chapter 3

Engineered Multifunctional Superparamagnetic Copper Iron Oxide Nanoparticles (SCIONs) for a Combined Magnetic Hyperthermia and Immune Therapy of Metastatic Cancers

3.1 Introduction

Metastatic cancer has been one of the most lethal diseases for decades, as it has complex pathophysiology and can affect multiple organs and systems simultaneously. Despite the substantial investments and efforts made, the high mortality rate among metastatic cancer patients remains a major public health concern, affecting millions of people worldwide.[129-131] Recently, cancer immunotherapy has emerged as a highly promising treatment option, with the aim of regulating the immune system and eliciting an intrinsic immune response to target and eliminate tumor cells.[132,133] Several strategies have demonstrated promising clinical outcomes, including targeting checkpoint molecules for the PD-1/PD-L1 axis,[138] administering cancer vaccines,[161] and transferring adoptive cells such as cytokine-induced killer cells (CIK)[169] and chimeric antigen receptor T cells (CAR-

T).[149] However, these approaches face challenges in the complex tumor microenvironment, including insufficient activation of the immune system, the low objective response rate in patients,[140] poor infiltration of the therapeutic agents into the tumor microenvironment, and difficulties in tracking and controlling the distribution of the anticancer components. As a result, the combination of therapies for the treatment of metastatic cancer has gained significant attention as a means of enhancing infiltration into the tumor microenvironment and eliciting a stronger immune response, thereby providing a more comprehensive approach to treating this complex form of cancer.[246]

Given the severe side effects associated with conventional radiotherapy or chemotherapy and the limited penetration capacity of near-infrared light, magnetic hyperthermia therapy (MHT) has emerged as a promising option for combination therapy.[247] Hyperthermia is a cancer therapy that raises the local temperature of the tumor to 41-45°C for a specified period, killing the tumor cells and sensitizing them to other treatments.[248] By using the magnetic field, the MHT is a remote-controlled therapeutic system that offers the ability to selectively release the anticancer agents with high local efficacy, excellent tissue penetration, and minimal harm to healthy tissue, providing a safe and effective way to enhance the infiltration of therapeutic agents and improve treatment.[249]

Iron oxide nanoparticles have been extensively investigated in the field of cancer treatment due to their potential as a targeted drug delivery method.[250] Targeted drug delivery aims to overcome the limitations of conventional drug delivery by using nanoparticles as carriers to deliver drugs specifically to areas of the patient's body affected by the disease while minimizing interaction with healthy tissue.[251,252] The unique property

of superparamagnetism, along with the small size, biocompatibility, ease of surface functionalization, and superior magnetic responsiveness of iron oxide nanoparticles, allow for effective dispersion of the nanoparticles and targeted delivery in the tumor microenvironment without incurring the high cost and prolonged preparation time associated with other drug delivery methods such as cell-specific ligands and pH-responsive approaches. Furthermore, exposure of these magnetic nanoparticles (MNPs) to an alternating magnetic field (AMF) generates highly localized heat within the cancer cells, rendering them an ideal candidate for MHT. Meanwhile, the precise targeting of the particles can also be achieved through manipulation by a magnetic field, enabling the simultaneous realization of MHT cancer treatment and targeted drug delivery. A few recent studies have shown promising results in MHT cancer treatment with the remaining challenges of delivering immunotherapy and MHT with one system concurrently, ensuring the combined therapy takes effect simultaneously and coherently.[246]

In this study, we designed and synthesized superparamagnetic copper iron oxide nanoparticles (SCIONs) and engineered them into a monodisperse multifunctional anti-cancer SCION complex, as depicted in Figure 3.1.

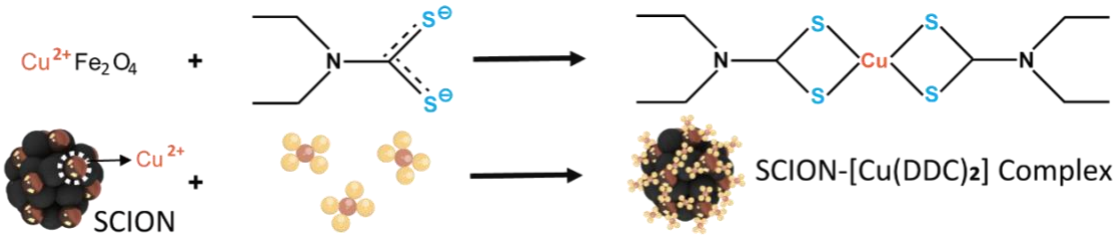

Fig.3.1 Schematic diagram of SCIONs and further self-assembling process between SCIONs and DDC-Na.

The porous structure of the SCIONs provides ample Cu^{2+} sites, which when loaded with sodium diethyldithiocarbamate trihydrate (DDC-Na), form the $[Cu(DDC)_2]$ complex (a widely proven anti-cancer ingredient) that self-assembles on the surface.[253] Compared to the traditional approach of delivering high-performance hyperthermia magnetic nanoparticles and programmed checkpoint blockade therapy ingredients separately, each SCION-complex serves as a multifunctional treatment component that simultaneously provides both MHT and $[Cu(DDC)_2]$ complex treatment. We performed a series of characterization and a preclinical study with the anticancer complex, the combined therapy of SCION complex and AMF manifested significant outcomes in eliminating tumor cells, restricting primary tumor growth, activating the immune response in the tumor microenvironment, and hindering the tumor cells metastasis.

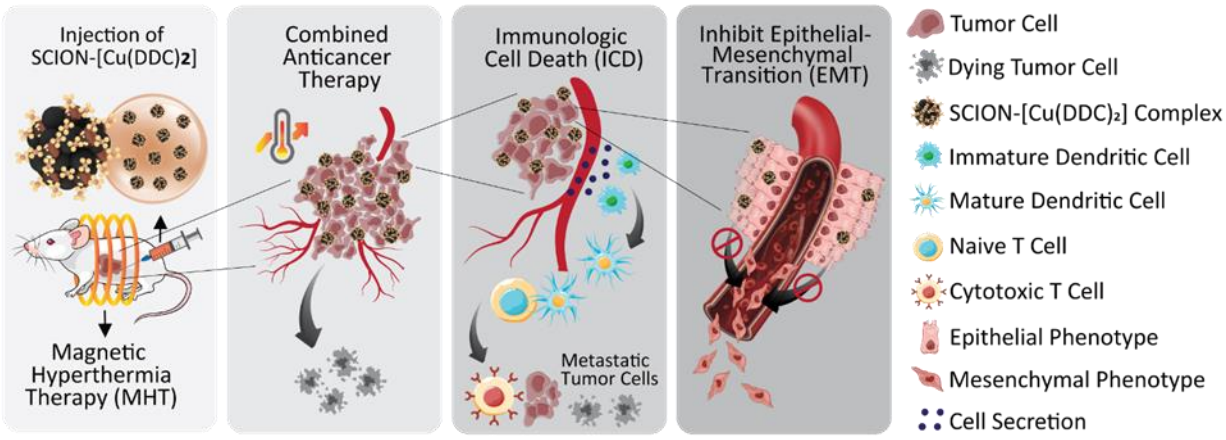

Fig.3.2 The mechanism of the combined MHT and SCIONs complex cancer therapeutic treatment and immune response in the tumor microenvironment.

The inherent mechanism and the process of the anti-cancer effect are proposed in Figure 3.2. (1) The SCION complex generates a considerable amount of local heat to eliminate tumor cells when AMF is applied. (2) Meanwhile, the anti-cancer ingredients

will continuously function in the tumor microenvironment inducing tumor cell death and apoptosis.[254] (3) Combined MHT and [$Cu(DDC)_2$] complex treatment ablation of tumor cells could generate tumor-associated antigens, The antigens were uptake by dendritic cells (DCs), which would lead to the activation of immunological cell death (ICD).[255] (4) The anti-cancer ingredients loaded on the surface of the SCION complex keep functioning to inhibit epithelial-mesenchymal transition (EMT) to prevent cancer metastasis from happening.[256]

3.2 Materials and methods

3.2.1 Synthesis and Characterizations of the SCIONs and the anti-cancer complex

The synthesis of the anti-cancer SCION-complex was performed through a facile and cost-efficient self-assembling process. Taking advantage of the sodium atom in DDC-Na's strong tendency to bind with divalent copper Cu^{2+}, $FeCl_3$ salt, and $CuCl_2$ salt was dispersed in ethylene glycol (EG) and subjected to a high-temperature solvothermal reductive reaction.[105] Polyvinylpyrrolidone (PVP) served as an ideal stabilizer, remaining negatively charged at -34mV ± 4.28 mV and leading to the synthesis of monodisperse SCIONs. The SCIONs dispersion was then mixed with a DDC-Na solution in a 1:1 ratio, resulting in the formation of the [$Cu(DDC)_2$] complex on the surface of the SCIONs. The detailed synthesis process is described in the Experimental Section. Scanning electron microscope (SEM) images of the SCIONs (Figure 3.3) and self-assembled SCIONs complex (Figure 3.4) were taken to visualize the surface texture.

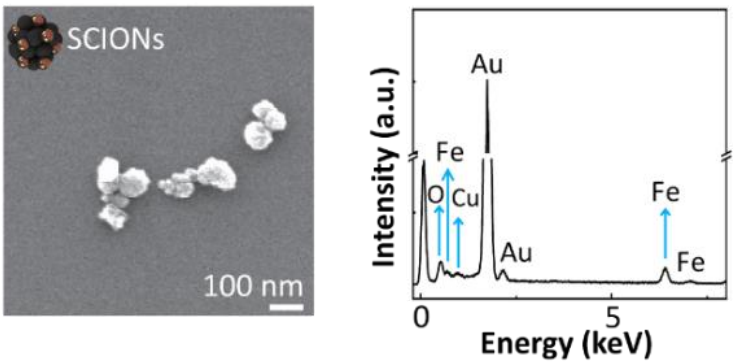

Fig.3.3 The representative SEM image (left) and the EDS (right) of our SCIONs. The left one shows the surface texture of the SCIONs.

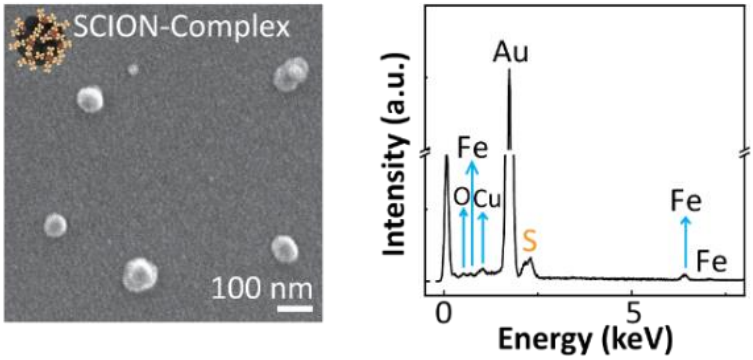

Fig.3.4 The representative SEM image (left) and the EDS (right) of our self-assembled SCIONs complexes. The SEM image shows the SCIONs are covered with a layer of $[Cu(DDC)_2]$ complex. Inside the EDS, the S peak indicates the SCION-$[Cu(DDC)_2]$ complex was successfully synthesized, while the Au peaks are the gold coater on the samples to improve the conductivity.

The SEM image in Figure 3.3 shows multiple Cu^{2+} sites on the surface of the SCIONs, while the SEM image in Figure 3.4 displays the SCIONs covered with a layer of $[Cu(DDC)_2]$ complex, indicating the successful surface functionalization of the SCIONs. Energy-dispersive X-ray spectrum (EDS) was also performed on both the SCIONs (Figure

3.3) and the self-assembled SCIONs complex (Figure 3.4). The peak of sulfur in the EDS spectrum of the SCIONs complex (Figure 3.4) confirms the successful complexation of the SCIONs-[$Cu(DDC)_2$].

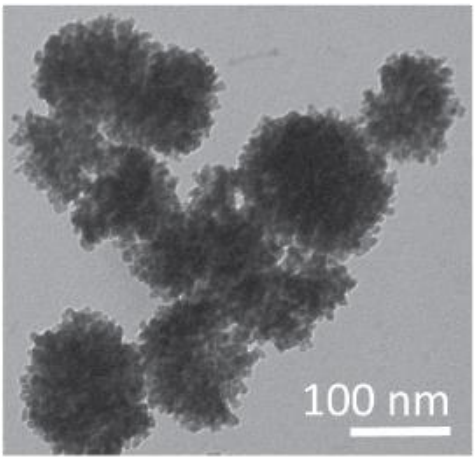

Fig.3.5 The representative TEM image of our synthesized SCIONs.

The synthesized SCIONs showed a porous structure composed of clusters of small spheres, as measured by transmission electron microscopy (TEM) (Figure 3.5) with an average diameter of 78 nm ± 8 nm. After the formation of the [$Cu(DDC)_2$] complex on the surface of the SCIONs, the SCION complex was measured by TEM with an average diameter of 128 nm ± 14 nm (Figure 3.6).

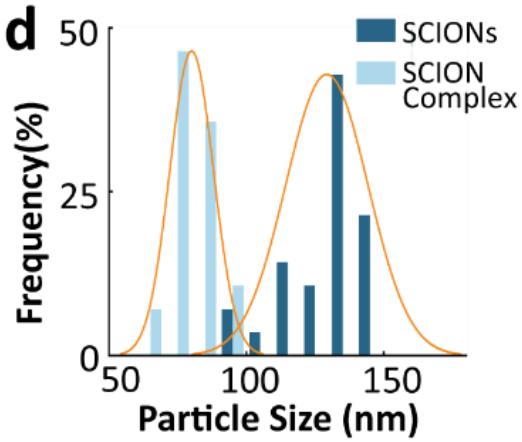

Fig.3.6 The size distribution for the SCIONs.

The X-ray diffraction (XRD) pattern (Figure 3.7) also demonstrated the highly crystalline nature of the SCIONs, with peaks (220) and (311) confirming the presence of divalent copper Cu^{2+}.

Nevertheless, to save the preparation time and cost of the targeted drug delivery nano-carriers and to utilize targeted drug delivery in more common situations, here we harness the unique superparamagnetism feature of the SCIONs confirmed by the hysteresis loop (Figure 3.7).

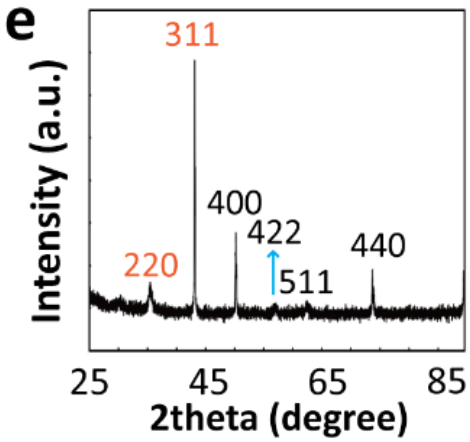

Fig.3.7 The magnetic hysteresis loop of the synthesized SCIONs.

When the magnetic particle size is sufficiently small, they will stay in the so-called "superparamagnetic state", which means the particles can still be conveniently aligned or manipulated by an external magnetic field, but after the magnetic field is removed, there won't be any magnetism left in the particle. The active anticancer SCIONs complexes can be delivered to the desired tumor local area by an external magnetic field, and once the magnetic field is removed, the particles can be well-dispersed in the tumor microenvironment.

3.3 Results and discussion

3.3.1 Functional Mechanism and In Vitro Study of the anti-cancer complex

By applying an external magnetic field to a site where tumor cells are proliferating, our anti-cancer SCION-[$Cu(DDC)_2$] complex would be drawn to the prime tumor microenvironment, where it could then be dispersed and trigger tumor cell death. We evaluated the magnetic targeting anti-cancer efficacy of the SCION-[$Cu(DDC)_2$] complex in both 2D and 3D cultured cell lines. The 2D cultured mouse breast cancer cell line 4T1 was first used to determine the anticancer activity of the complex. The cells were seeded into 96-well plates (2000 cells/well) and incubated overnight, and then treated with the appropriate formulation for 48 hours before undergoing the MTT assay.[257] The results showed significant anticancer efficacy in 4T1 cells (as demonstrated in Figure 3.8), while the control SCIONs showed no cytotoxicity. To assess the effects of the SCION-[$Cu(DDC)_2$] complex on other metastatic cancers, the mouse melanoma cell line (B16F10) was also subjected to the MTT assay with the same treatment (as shown in Figure 3.9).

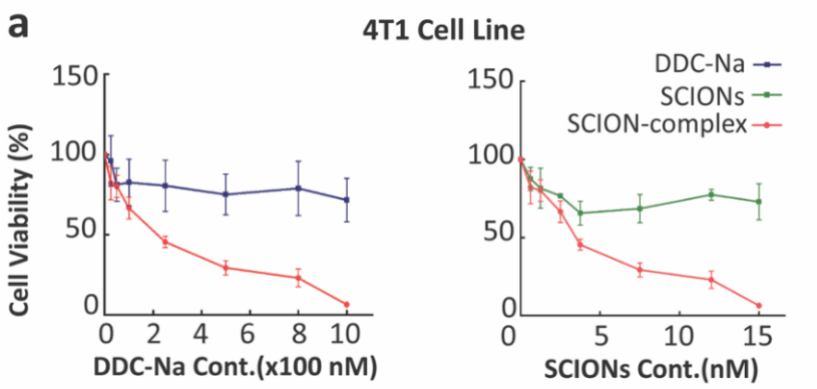

Fig.3.8 MTT assay 4T-1 cells were treated with the same formulations for 48 h further added SCION-[Cu(DDC)$_2$] complex dispersion compared to DDC-Na solution and SCION-[Cu(DDC)$_2$] complex dispersion compared to SCIONs dispersion and analyzed with the MTT assay. The results are the mean ± SD (n = 4).

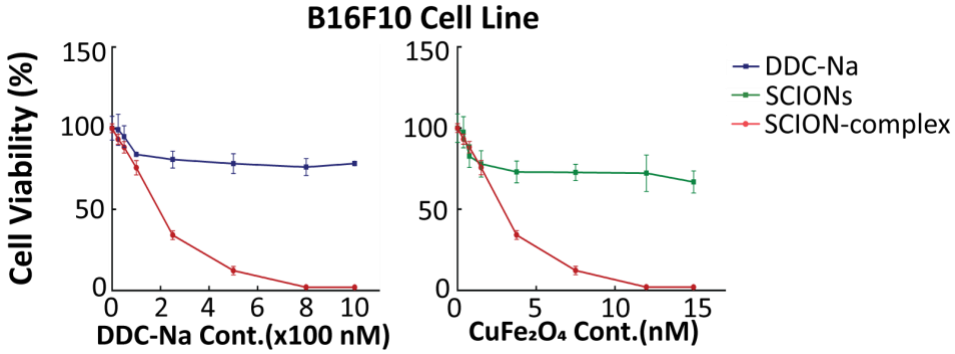

Fig.3.9 MTT assay B16F10 cells were treated with the same formulations for 48 h further added SCION-[Cu(DDC)$_2$] complex dispersion compared to DDC-Na solution and SCION-[Cu(DDC)$_2$] complex dispersion compared to SCIONs dispersion and analyzed with the MTT assay. The results are the mean ± SD (n = 4).

Apoptosis, the process of programmed cell death, is typically identified by specific physical features and biochemical pathways that require energy. Tumor cell apoptosis refers to the programmed cell death of cells within a tumor, which is an important

mechanism for the elimination of cancerous cells in the body.[258] This process can be induced by a variety of factors, including our immunotherapy, the flow cytometry results in Figure 3.10 reveal that our SCION-complex significantly increased the apoptotic tumor cells (4T1 cell line) rate.

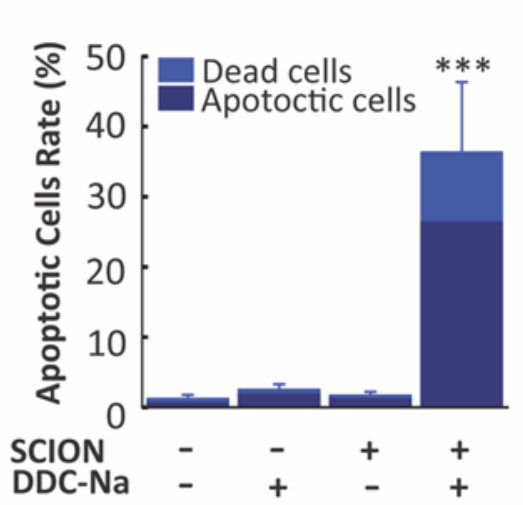

Fig.3.10 Annexin V/PI apoptosis assay determines the percentage of late-stage apoptotic cells (annexin V+/PI+) and early-stage apoptotic cells (annexin V+/PI-) with flow cytometry. (SCION, 15nM; DDC-Na 1M. Data are presented as the mean ± SD, n = 3, *** $P < 0.001$ compared with the negative control. # $P < 0.05$, ### $P < 0.001$ compared with the CDL treatment group).

The liquid overlay method was employed to establish tumor spheroids for the in vitro 3D model anticancer effect experiment. Fluorescent mouse breast cancer cell line 4T1-mCherry was used. Briefly, a 96-well plate was pretreated with 1% (w/v) agarose gel and then seeded with 4T1-mCherry cells.[259] The spheroids typically formed in five days and were then treated with various test formulations and imaged every 24 hours. Figure 3.11 clearly shows that the structure of the tumor spheroids was damaged by the complex. The

outside part of the tumor spheroids continued to disintegrate, while the control group maintained the integrity of its original structure and showed growth in spheroid size.

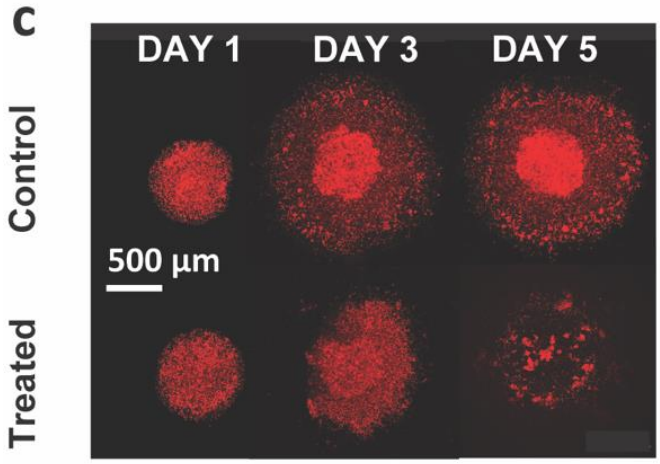

Fig.3.11 Tumor spheroids were treated with control formulation and SCION-[$Cu(DDC)_2$] complex dispersion (1M) for 72 h. At the end of treatment, tumor spheroids were analyzed with the Cell Imaging Multi-Mode Reader. It clearly shows the tumor spheroids structure was damaged by SCION-[$Cu(DDC)_2$] complex dispersion, while the other two show the integrity of the original structure.

As previously stated, metastasis is a critical issue for the majority of cancer patients. Our SCION-[$Cu(DDC)_2$] complex has been demonstrated to have anti-cancer effects on primary tumor sites, however, its true potential lies in its ability to function continuously in the tumor microenvironment and prevent the migration of tumor cells from the primary site to neighboring organs and tissues. In our experiments, a wound-healing assay was performed using the red fluorescence protein-labeled mouse breast cancer cell line 4T1-mCherry.[260] The 4T1-mCherry cells were seeded in a 96-well plate to form a confluent monolayer, which was then scraped with a pipet tip to create a scratch. The cells were then

treated with the control medium, SCION dispersion, DDC-Na solution, and the SCION-complex dispersion in high/low concentration after the generation of the scratch. The photographic records of the wound healing process were taken at the outset and every eight hours, while the representative comparison between the control group and the high-concentration SCION-complex group is depicted in Figure 3.12. The prominent difference in migration between these two groups clearly demonstrates the efficacy of our SCION-[$Cu(DDC)_2$] complex in preventing tumor cell metastasis.

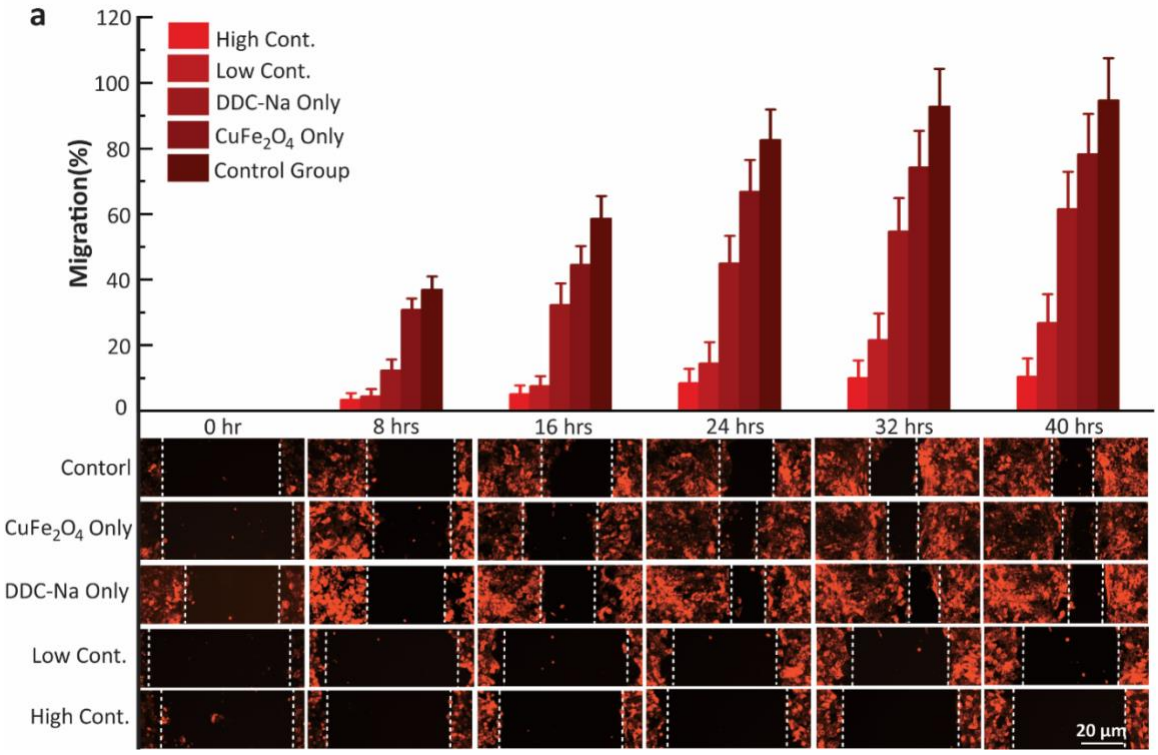

Fig.3.12 SCION-[$Cu(DDC)_2$] complex capability of hinging tumor cell metastasis. Wound-healing study. Cells received different treatments after the generation of the scratch. Then, photos were taken at the beginning and every eight hours. Cherry red fluoresce protein labeled 4T1 cells were used in this study. Summary bar graph illustrating percentage wound closure at indicated time points during the scratch wound assay.

Accumulating evidence suggests that the presence of intra-tumoral heterogeneity is a key factor in the development of resistance to anticancer therapies. In the process of wound healing, fibroblasts, which are a part of the paraneoplastic stroma, are known to play a vital role. There has been a rising interest in exploring the pathophysiological roles of cancer-associated fibroblasts (CAFs) in the complex tumor microenvironment.[261] We proved the suppressive ability of our SCION-complex to the intra-tumoral CAF heterogeneity by the western blot showing low levels of α-smooth muscle actin (α-SMA) (Figure 3.13) and the transwell system with various treatments to 4T1 cells in the top chamber and fibroblasts in the bottom chamber (Figure 3.14).[211,262]

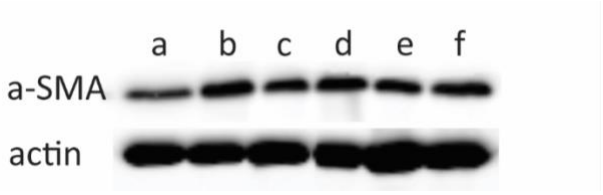

Fig.3.13 The western blot shows the secretion level of α-SMA of the CAFs while the 4T1 cancer cells are treated with different formulations. Group a is treated with the dispersion of our SCION-[$Cu(DDC)_2$] complex for 4 hours. Group b is treated with the dispersion of our SCIONs for 4 hours. Group c is treated with the dispersion of our SCION-[$Cu(DDC)_2$] complex for 4 hours. Group d is treated with the solution of DDC-Na for 4 hours. Group e is treated with the solution with TGF-β stimulation for 12 hours. Group f is treated with the solution with TGF-β stimulation for 24 hours.

Activated fibroblasts accumulate in the wound and are involved in many aspects of the tissue remodeling cascade that initiates the repair process and prevents further tissue damage. CAFs play crucial roles in tumor progression and the response to chemotherapy.

The concept of intra-tumoral CAF heterogeneity refers to the presence of inflammatory CAFs with low levels of α-smooth muscle actin (α-SMA) and high levels of IL-6 expression, which are in striking contrast to transforming growth factor-β (TGF-β)-dependent myofibroblast CAFs with high α-SMA expression levels.

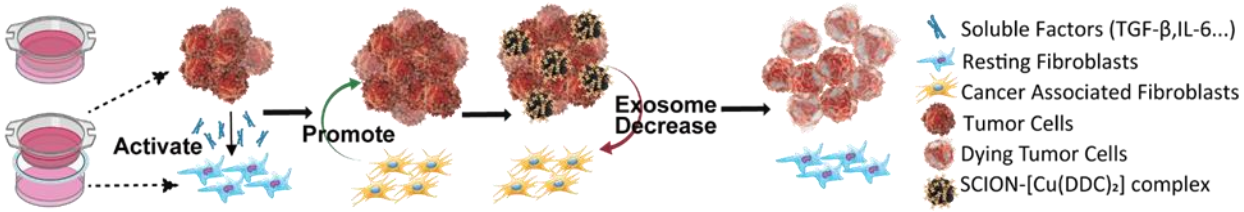

Fig. 3.14 Transwell coculture system to mimic the CAFs in the tumor microenvironment in vitro to study the impact of our SCION-complex on the CAF heterogeneity. In the transwell system, mice fibroblasts were seeded in the bottom chamber and 4T1 cells with SCION-complex (or different formulations) were seeded in the top chamber. Because of the transwell system deployment, mice fibroblasts were inaccessible to either 4T1 cells, while the medium containing tumor antigens of 4T1 cells and different formulations could pass the micropores (pore size = 0.28 μm) in the membrane to stimulate or suppress the fibroblasts.

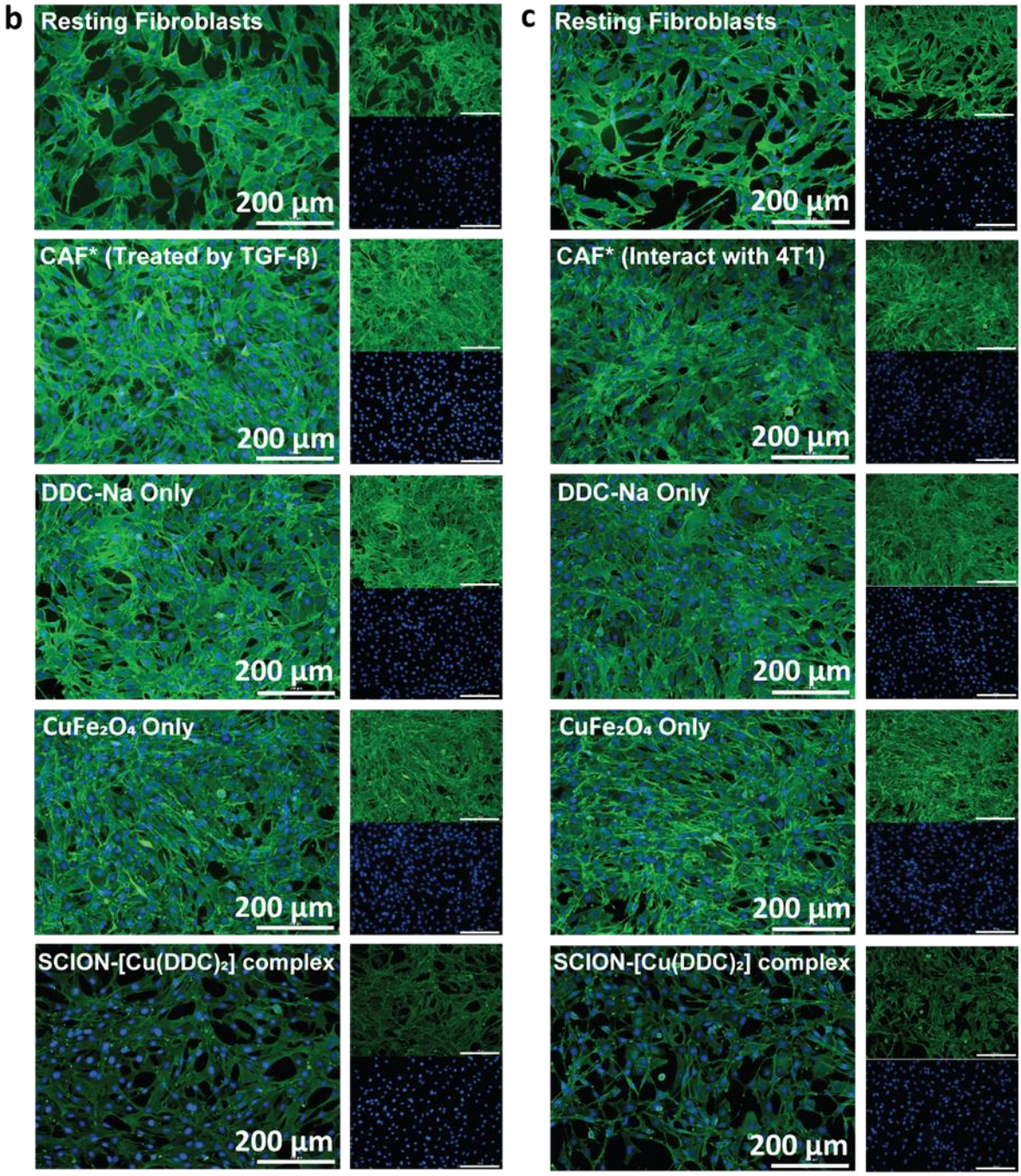

Fig.3.15 Fluorescence image of transwell coculture system to mimic the CAFs in the tumor microenvironment in vitro to study the impact of our SCION-complex on the CAF heterogeneity. After 12hrs co-cultures, the mice fibroblasts were activated to the CAFs

phenotype. The SCION-complex treatment suppressed the CAFs heterogeneity and the CAFs were back to the resting fibroblasts phenotype.

3.3.2 The *In Vitro* Magnetic Hyperthermia Therapy by Utilizing the Multifunctional SCIONs Complexes

The SCIONs play a critical role in the combined magnetic hyperthermia and immune therapy by facilitating magnetic manipulation for drug delivery and generating local heat for magnetic hyperthermia therapy (MHT). For the in vitro study, the murine breast cancer cell line 4T1 was used. The cells were seeded into 12-well plates (15,000 cells/well) and treated with the standard protocols for 48 hrs. The anti-cancer SCIONs complexes were then added to the 4T1 cell environment. An external magnetic field with a round shape was applied to the central area of the cell incubation well, allowing the magnetic positioning SCIONs complexes to be directed to and act on a specific area of cells, as illustrated in Figure 3.16. Figure 3.17 shows that the application of an external magnetic field was effective in delivering and confining the anticancer system to the desired area, as evidenced by the clear boundary (Figure 3.16, right, enlarged view) between the round central area and the surrounding ring area, both of which were stained using the JC-1 fluorescence probe staining method. The central area, subjected to the magnetic field, showed a red color indicating the death of tumor cells, while the surrounding ring area, without the magnetic field, showed a green color indicating the survival of cancer cells. The drug demonstrated effective anti-cancer performance, and the process will be further detailed in the cytotoxicity verification section.

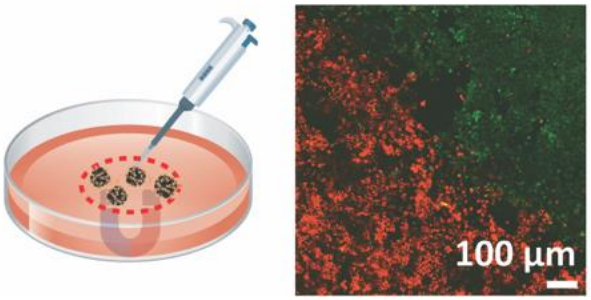

Fig.3.16 Scheme of the magnetic-targeting process and the primary anti-cancer response of our SCIONs Complexes. Enlarged images show the clear boundary between the targeted treating area with external magnetic field manipulation and the off-target ring area.

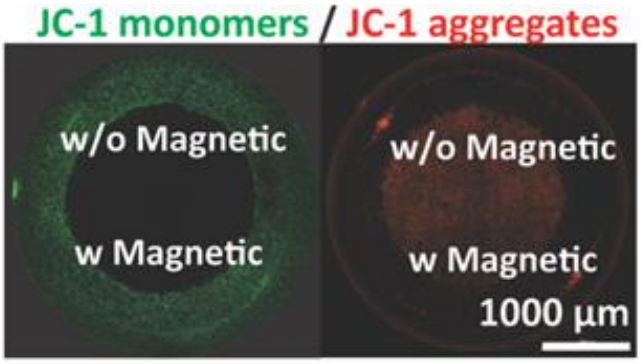

Fig.3.17 The image of 4T1 cells treated with magnetic targeted delivery SCIONs-Complex with JC-1 as a fluorescence probe staining. The mitochondrial membrane potential of 4T1 cells was determined with JC-1 as a fluorescence probe staining method, which clearly shows the external magnetic field confining our SCIONs Complexes in the middle round area while taking effect.

Further, the intracellular uptake of Cy5-labeled SCIONs complexes was evaluated using mCherry-expressing 4T1 cells via confocal laser scanning microscopy (CLSM) (as shown in Figure 3.18). The result provides clear evidence of the rapid and efficient cellular

uptake of the SCIONs complexes, ensuring their effectiveness in *in vitro* intracellular MHT for the eradication of tumor cells.

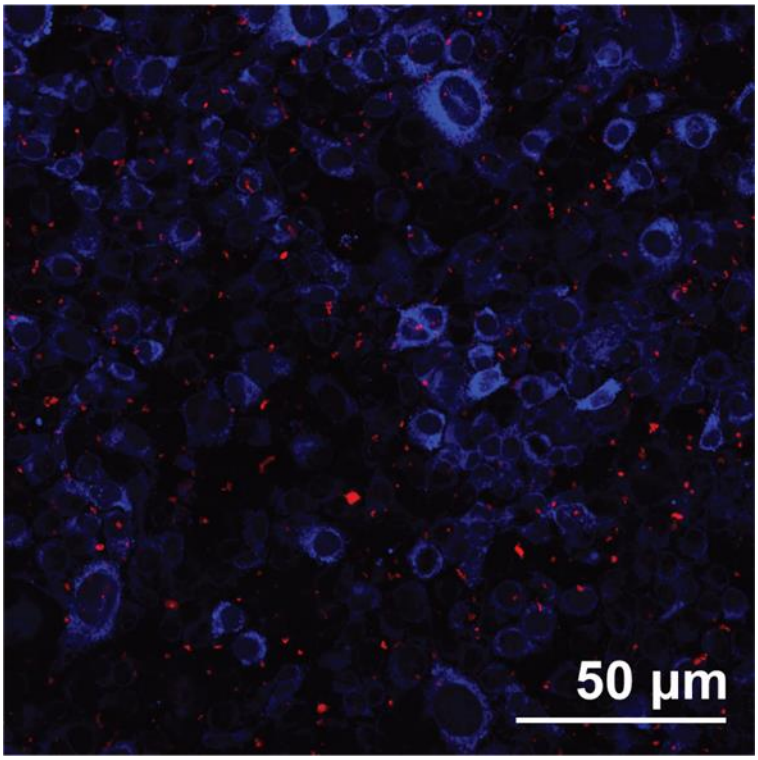

Fig. 3.18 The confocal microscopic images of the 4T1-mCherry cells intracellular uptake of Cy5-labeled SCIONs complexes. The image colors were transformed into their complementary counterpart for better presentation.

Observed through confocal microscopic images, demonstrate the strong cellular uptake of the SCIONs complexes, as indicated by the presence of strong fluorescent signals generated from the Cy5-labeled nanoparticles around the nuclei of the 4T1-mCherry cells. This provides clear evidence of the rapid and efficient cellular uptake of the SCIONs complexes, ensuring their effectiveness in *in vitro* intracellular MHT for the eradication of tumor cells.

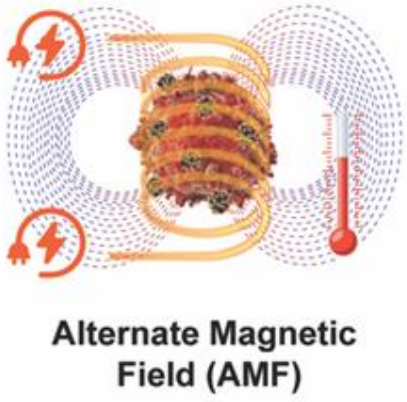

Fig.3.19 The scheme of the SCIONs Complexes hyperthermia effect when an AMF is applied.

By applying an alternating magnetic field (AMF) instead of a constant external magnetic field, a magnetic hyperthermia therapy was introduced to the tumor cells, wherein the SCIONs complexes generated a significant amount of heat (as shown in Figure 3.19). The exposure of cells to temperatures up to 45°C creates a condition of intracellular heat stress, known as hyperthermia. This heat stress can cause a failure in thermoregulation, leading to negative effects such as protein misfolding and aggregation, alteration of signal transduction, changes in the pH value of the environment, reduced oxygenation of the tumor, and induction of cell apoptosis and death. In comparison to chemotherapy, magnetic hyperthermia therapy not only has milder side effects, but it also does not result in drug resistance among tumor cells, ensuring long-term efficacy in cancer treatment.

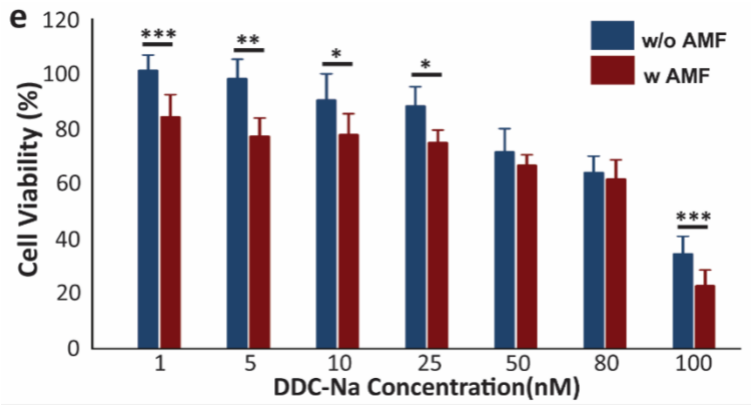

Fig.3.20 The 4T1 cells were separated into two groups, for each determined concentration, one group of 4T1 cells was treated with an AMF for 20 mins; then the cells were incubated at 36℃ for 24hrs; all the cells were treated with our SCIONs Complexes. It clearly indicates the magnetothermal effects helped to increase the anti-cancer efficiency by at least 5%.

As aligned in Figure 3.20, the introduction of hyperthermia has resulted in a significant enhancement in the ability of the SCION-complex to combat cancer. Specifically, the use of hyperthermia has been found to improve the effectiveness of the SCION-complex in destroying cancerous cells by up to 20%, representing a momentous improvement in anticancer therapy.

3.3.3 The immunological cancer therapeutic treatment utilizing the complex

Current research in tumor immunotherapy recognizes the importance of immunogenic cell death (ICD) in activating anti-cancer immunity. The release of specific damage-associated molecular patterns creates an active tumor immune microenvironment, leading to the maturation of dendritic cells and the stimulation of T-cell priming. Activated

T-cells then target and eliminate tumor cells, reducing the risk of metastasis.[263-265] As depicted in the schematic of ICD (Figure 3.21), cells undergoing ICD are often characterized by four biomarkers: (1) cancer-cell-surface translocation of calreticulin (CRT);[266] (2) adenosine triphosphate (ATP) release by the cancer cells;[267] (3) high mobility group box 1 (HMGB1) released by the cancer cells;[268] and (4) interferon-γ (IFN-γ) released by T-cells.[269] CRT transfers to the cell surface and serves as an "elimination" signal to antigen-presenting cells with CD91 receptors, while extracellular ATP acts as a short-range trigger. HMGB1 is a biomarker of late-stage ICD and is required for antigen presentation by dendritic cells (DCs). The damage-associated molecular patterns facilitate the presentation of antigens released from cancer cells, activate anti-cancer cytotoxic T-cells, and establish long-term adaptive anti-cancer immunity. A range of therapies, including chemotherapy and radiotherapy, can effectively induce ICD and generate "in situ tumor vaccines," transforming the inactive tumor immune microenvironment into an active one and offering a new approach to cancer therapy.[161]

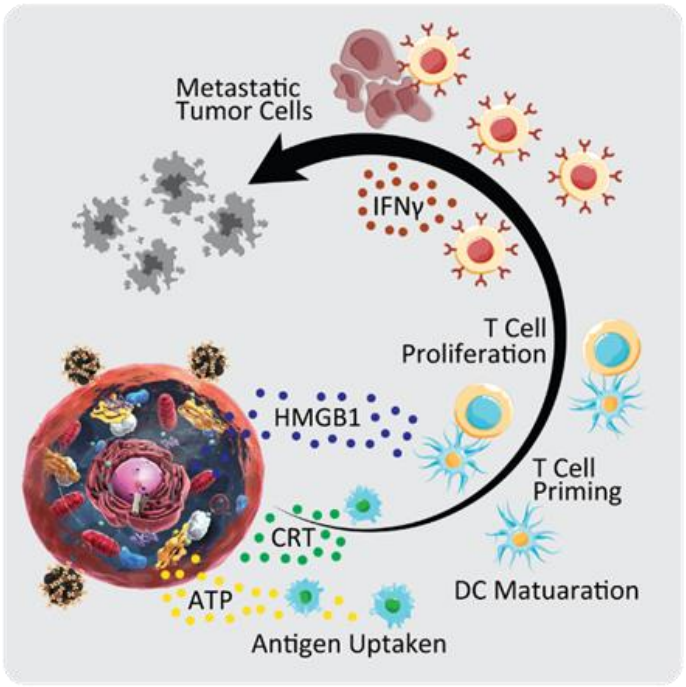

Fig.3.21 The mechanism of the immunogenic cell death induced by our SCION-[Cu(DDC)$_2$] complex.

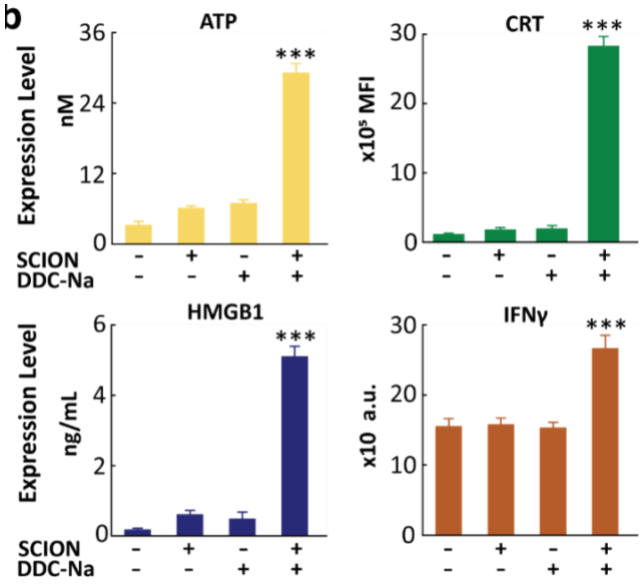

Fig.3.22 Biomarkers of ICD. Cell surface CRT was determined with flow cytometry. ATP release was determined with an ATP bioluminescence detection kit. HMGB1 release was

determined with ELISA. IFN-γ release was determined with flow cytometry. (Data are presented as the mean ± SD, n = 3, * $P < 0.05$, ** $P < 0.01$, *** $P < 0.001$, compared with the negative control group; * $P < 0.05$, ** $P < 0.01$, *** $P < 0.001$, compared with CDL treatment group.)

In order to assess the effectiveness of our SCION-[$Cu(DDC)_2$] complex treatment in inducing immunogenic cell death (ICD), we evaluated its ability to elicit the release of damage-associated molecular patterns and activate dendritic cell maturation. The results, as depicted in Figure 3.22, showed that the SCION complex group exhibited the highest level of cell surface calreticulin (CRT) compared to the negative control. The therapy groups with DDC-Na and the SCIONs did not result in a significant increase in cell surface CRT. The results further indicated that the treatment with the SCION complex led to the most substantial release of adenosine triphosphate (ATP) in the cell culture medium. The release of high mobility group box 1 (HMGB1) in the conditioned cell culture medium was determined using an ELISA kit and was found to be significantly increased by the SCION complex therapy. These results provide strong evidence that our SCION-[$Cu(DDC)_2$] complex treatment is capable of efficiently ICD and may hold potential as a "tumor vaccine" approach for the treatment of metastasis.

Additionally, our SCION-[$Cu(DDC)_2$] complex demonstrates the potential to restrict the migration of tumor cells from the primary site by inhibiting the epithelial-mesenchymal transition (EMT) process. EMT is a biological transformation that enables a polarized epithelial cell to adopt a mesenchymal cell phenotype, which is characterized by increased migratory capacity, invasiveness, resistance to apoptosis, and heightened production of extracellular matrix components (Figure 3.23).[270]

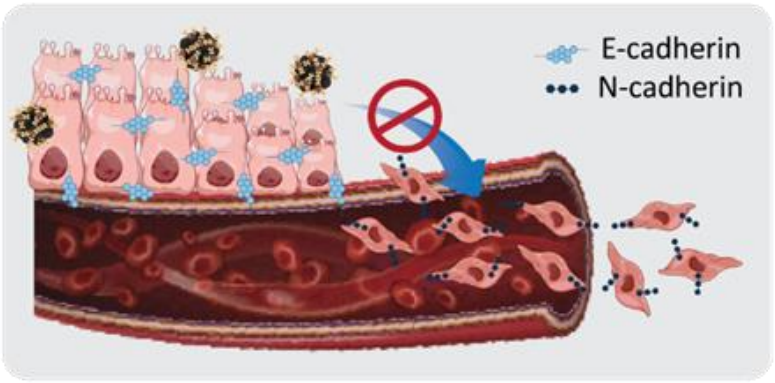

Fig.3.23 The mechanism of the tumor cell epithelial-mesenchymal transition hinged by the complex.

This process is initiated by the activation of various molecular processes, such as the regulation of transcription factors, expression of specific cell-surface proteins, and changes in the expression of specific microRNAs. E-cadherin is a key component of cell adhesion and is a hallmark of the epithelial phenotype, while N-cadherin confers enhanced migratory and invasive capacity to tumor cells (Figure 3.24).[271]

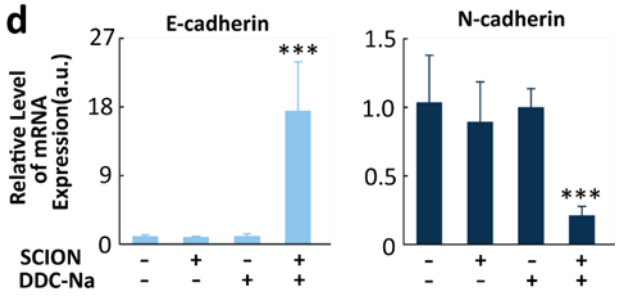

Fig.3.24 The relative level of E-cadherin mRNA, and N-cadherin mRNA expression were determined by the real-time polymerase chain reaction. The results indicate that our SCION-[Cu(DDC)$_2$] complex efficiently hinges on the EMT process. (Data are presented as the mean ± SD, n = 3, *** $P < 0.001$ compared with the negative control. * $P < 0.05$, *** $P < 0.001$).

To evaluate the impact of our SCION complex on EMT, we treated 4T1 cells with our system and analyzed various biomarkers, including Slug transcription factor, Snail transcription factor, Twist transcription, and Vimentin. The results, as displayed in Figure 3.24 and Figure 3.25, showed a significant increase in E-cadherin and a decrease in N-cadherin and other biomarkers, indicating the potential of our system to restrict the migration of tumor cells by inhibiting the EMT process.[272]

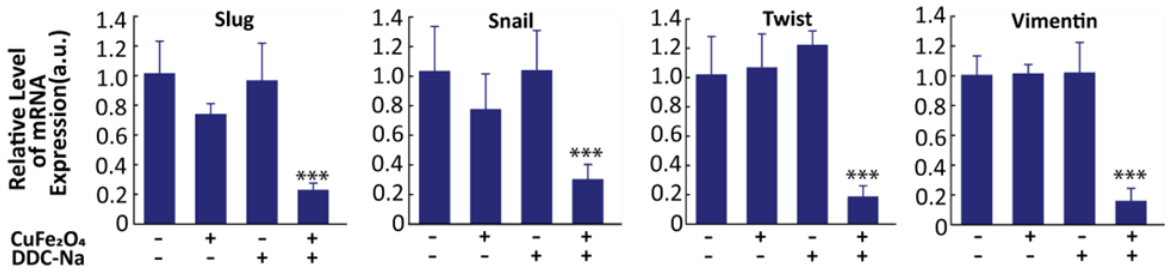

Fig.3.25 The relative level of the Slug transcription factor, Snail transcription factor, Twist transcription, and Vimentin mRNA expression was determined by the real-time polymerase chain reaction. The results indicate that our SCION-[$Cu(DDC)_2$] complex efficiently hinges on the EMT process. (Data are presented as the mean ± SD, n = 3, *** $P < 0.001$ compared with the negative control. * $P < 0.05$, *** $P < 0.001$ compared with the CDL treatment group).

3.3.4 *In vivo* Immunotherapy Combined with MHT

In the treatment of metastatic cancer, the challenge is to provide effective therapy for metastatic cancer cells, which are a major cause of post-primary therapy morbidity. To address this challenge, we aimed to exploit the potential of our SCION complex to enhance the immune response and potentially inhibit metastatic tumor growth in combination with immunological cancer treatment. To validate the advantages of this combined

immunological cancer therapy with MHT, we conducted a preclinical animal experiment using 4T1 cell inoculated BALB/c mice.

A total of 1×10^6 4T1 cells were inoculated in the right flank of each BALB/c mouse to form a tumor. Once the tumor size reached approximately 100 mm^3 in volume, the mice were randomly assigned to one of four groups, each consisting of 6 mice: (1) saline control; (2) SCION complex injection; (3) SCION injection combined with MHT; (4) SCION complex injection combined with MHT. Every other day, Groups 1 and 2 were administered 100 μL of phosphate-buffered saline (PBS) and SCION complex PBS dispersion, respectively. Groups (3) and (4) were injected with 100 μL SCION PBS dispersion and SCION complex PBS dispersion, respectively, and treated with MHT for 20 minutes right after the injection every other day.

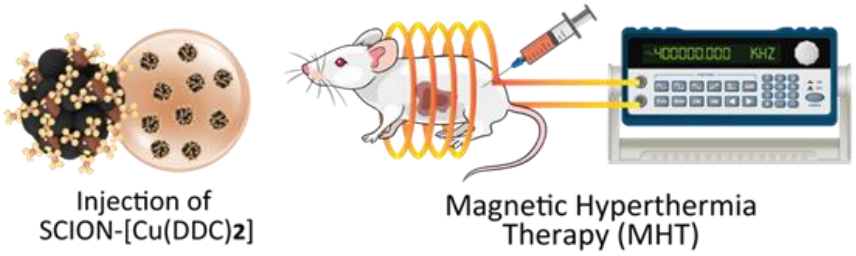

Fig.3.26 Schematic illustration of the combined SCIONs Complexes and MHT to inhibit the growth of tumors.

The body weights and tumor sizes of the mice in each group were recorded every other day. The design of the MHT device for the mice is shown in Figure 3.26. The representative real-time infrared thermal image of SCIONs complexes injected and restricted to the tumor area under AMT is shown in Figure 3.27.

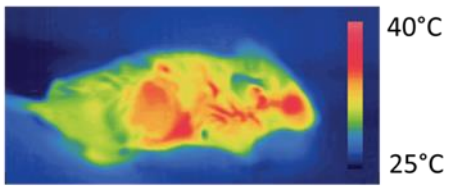

Fig.3.27 Representative real-time IR thermal imaging of SCIONs subcutaneously in the tumor area under AMF.

The tumor region is visibly heated. The magnetic hyperthermia performance of the SCION complex was evaluated at varying magnetic field intensities and concentrations in vitro. Importantly, there was no degradation of MHT efficacy observed during one or five cycles of AMF on/off, demonstrating the exceptional stability of the SCION complex for magnetic hyperthermia applications.

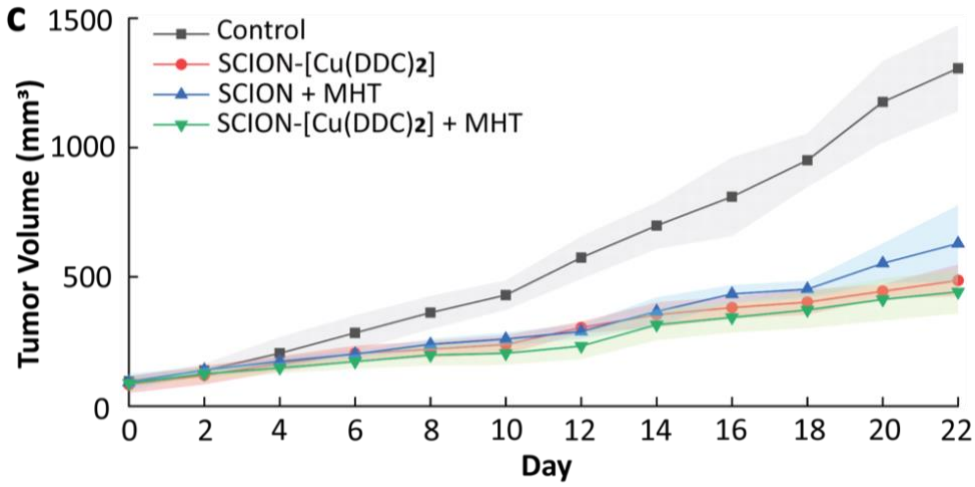

Fig.3.28 Tumor growth curves of diverse groups after various treatments as indicated (n = 5).

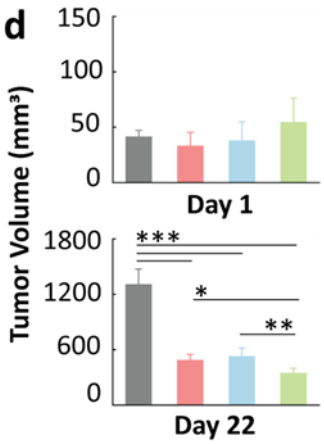

Fig.3.29 Average tumor size of diverse groups before and after 10 treatments as indicated (n=5).

The results of the tumor growth and average tumor volume increase of each group are displayed in Figures 3.28 and 3.29. The tumor growth in the saline control group (1) followed the expected aggressive progression, while groups (2), (3), and (4) displayed a successful delay in tumor growth to varying degrees. The data shows that both SCION complex treatment and SCION MHT contributed to the delay in tumor growth, with the latter exhibiting improved performance at the beginning of the treatment. The combination of SCION complex and MHT therapy in the group (4) resulted in the most significant inhibition of tumor growth, with stable efficacy observed throughout the early to late stages of treatment.

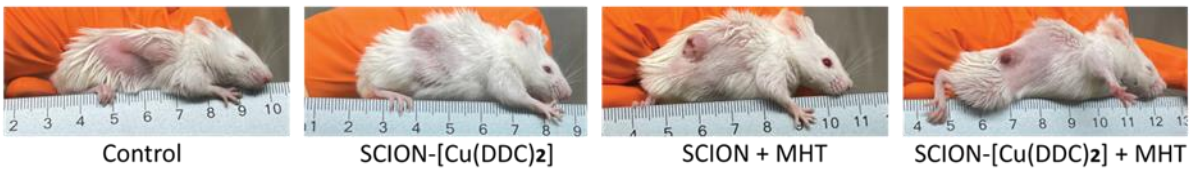

Fig.3.30 Representative digital photos of 4T1 tumor-bearing mice on the 15th day after various treatments.

Figure 3.30 is the representative digital photos of the mice in each group on the 15th day of the treatment. Corresponding to the tumor growth curve, compared to no inhibiting behavior of tumor growth in the control group, groups 2, 3, and 4 all displayed significant inhibiting effects, while group 4 furtherly confirmed the noteworthy improvement in the anti-cancer performance of the combined hyperthermia immunotherapy.

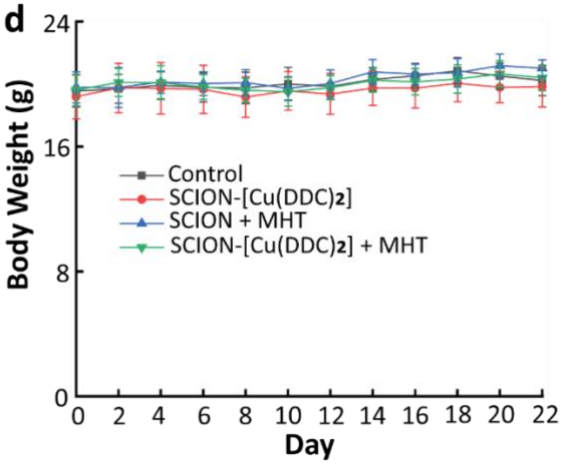

Fig.3.31 Mice bodyweight curves of diverse groups after various treatments as indicated (n = 5).

Additionally, no distinct changes were found in the body weights of all groups, indicating the comparatively high biosafety of varied treatments.

3.6 Mechanism Study of the Immunological Cancer Therapy Combined SCION-complex and MHT Treatment

The combination of SCION complex and MHT were investigated on the immune cells in the 4T1 tumor-bearing mice to explore its synergistic effect on the immunological cancer therapeutic treatment. As previously described, the initiation of the immunogenic cell death

(ICD) process is triggered by the maturation of DCs when the primary tumor is treated with the SCION-complex. Then, the recognition of tumor-associated antigens by DCs leads to their activation and maturation. In turn, T cells, particularly cytotoxic CD8+ T cells, enter the patient's body and target any remaining tumor cells. Cytotoxic T cells (CD8+ T cells) are widely recognized as vital contributors to cancer immunotherapy, inducing the apoptosis of tumor cells through the release of perforin and granzyme.

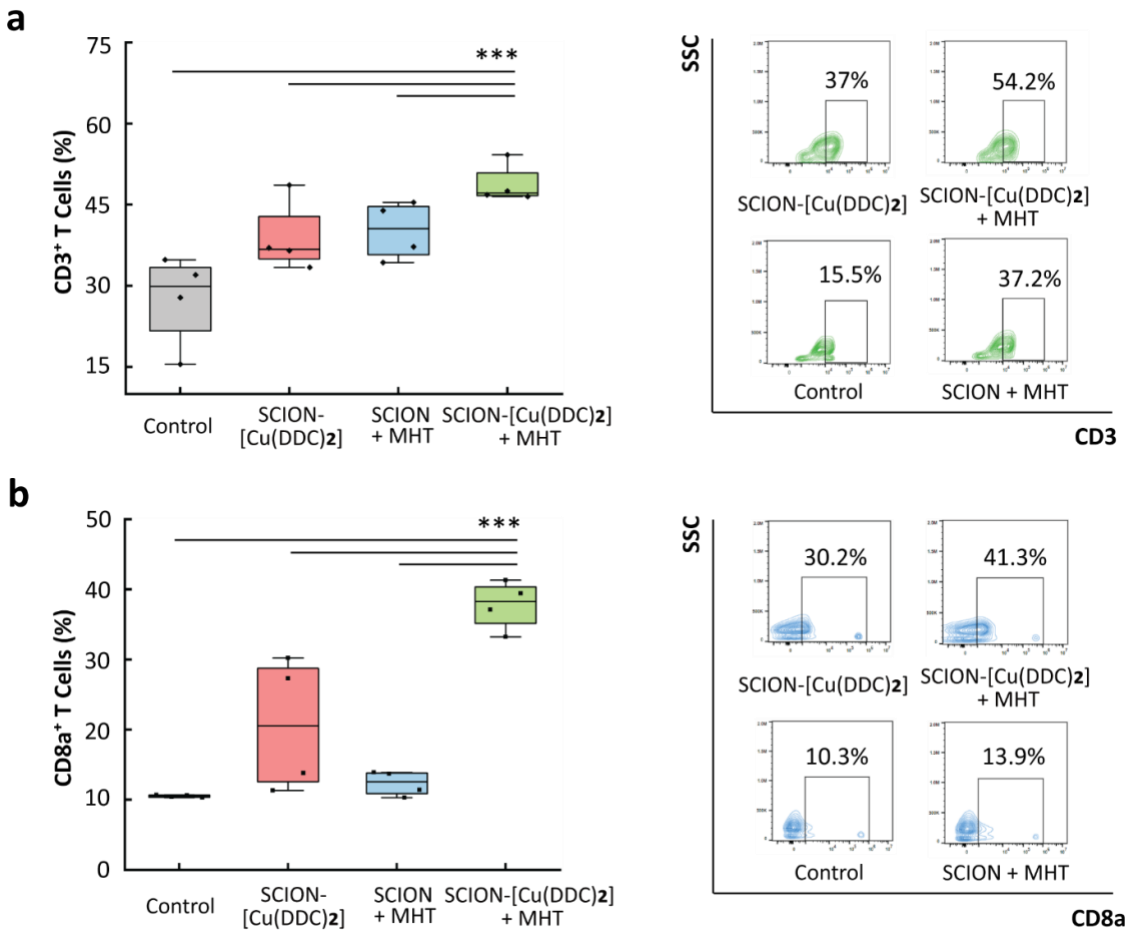

Figure.3.32 Mechanism study of antitumor effect of the SCIONs Complexes based MHT.

(a, b) Typical flow cytometry plots of CD3+ T cells (left panel in a) and CD8+ T cells (left panel in b) in left tumors after various treatments indicated. (Right panels in a, b)

Percentages of tumor-infiltrating CD3+ T cells (right panel in a) and CD8+ T cells (right panel in b) with respect to the total tumor of cells. (n = 4). Statistical significances were calculated via Student's t-test. *P < 0.05, **P < 0.01, and ***P < 0.001.

To provide a mechanistic understanding of these effects, we analyzed the increase in the number of tumor-infiltrating mature T cells (CD3+) and CD8+ T cells (CD3+ CD8+) in the immune system of the spleen in tumor-bearing mice using flow cytometry (n=4 per group).[273] The results of the flow cytometry tests indicated a significant increase in the percentage of T cells (Figure 3.32a) and CD8+ T cells (Figure 3.32b) in the spleen of the mice after treatment with (2) SCION complex alone, (3) SCION combined with MHT, and (4) SCION complex combined with MHT, as compared to the control group. Notably, the highest population of T cells and CD8+ T cells was observed in the mice treated with SCION complex combined with MHT.

The underlying mechanism of the collaborative antitumor effect produced by the combination of SCION-complex treatment and MHT aligns with the mechanisms of other reported combinational immunotherapies and hyperthermia therapies. The MHT-treated tumors generate tumor-associated antigens that can be recognized by dendritic cells (DCs). The maturation of DCs triggers systemic antitumor immune responses. Additionally, our SCION-complex effectively activates DC maturation and accelerates the priming of T cells, significantly increasing their presence in the tumor microenvironment. As a result, T cells, particularly cytotoxic CD8+ T cells infiltrate the cancer patient's immune system and target the remaining cancer cells, leading to a synergistic antitumor effect.

3.3.6 *In Vitro* Immunity Stimulation of Dendritic Cells by SCION-complex

Antigen-specific immune cells are crucial for the effectiveness of cancer immunotherapy, and their activation is facilitated by antigen-presenting cells (APCs). Dendritic cells (DCs), an important type of APC, are critical in both the stimulation and control of innate and adaptive immune responses.[19] One way to assess the maturation level of DCs is to estimate the expression of the representative co-stimulatory molecules CD80 and CD86. Therefore, we used a transwell coculture system to mimic the DCs in the tumor microenvironment in vitro to study the impact of our SCION-complex on the immunological system (Figure 3.33).[162]

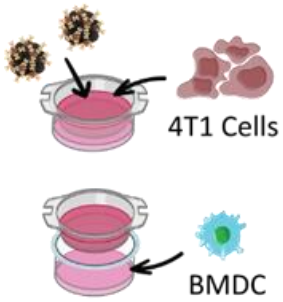

Figure.3.33 *In vitro* Transwell system experiment to mimic different therapies.

DCs were labeled with antibodies CD40, CD80, CD86, and MHCII. The maturation of DCs was determined by the flow cytometry analysis of the co-culture medium. Remarkably, the 4T1 cell fragments from SCION-complex treatment could highly elevate the percentage of matured DCs (Figure 3.34). The data indicates that our anti-cancer SCION-complex effectively activates DCs in vitro.

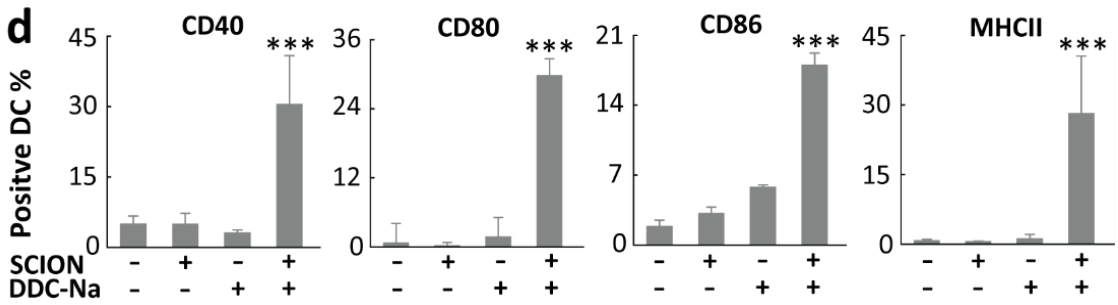

Figure.3.34 Representative flow cytometry plots and quantification of CD80 and CD86 expression on dendritic cells gated by CD11c+ cells. Data are expressed as means ± SD (n = 3). Statistical significances were calculated via Student's t-test.

3.4 Conclusion

In conclusion, the multifunctional SCION-[Cu(DDC)$_2$] complex has demonstrated its potential as an effective therapeutic option for primary and metastatic tumor treatments. The unique combination of targeted delivery, magnetic thermal therapy, and immune therapy allows for the induction of cell death in primary tumor cells and the stimulation of systemic immune responses. The ability of the SCIONs to deliver the active anticancer compound [Cu(DDC)$_2$] directly to the tumor microenvironment, and to generate heat through magnetic thermal therapy, enhances the efficacy of the treatment. Furthermore, the continuous stimulation of the tumor microenvironment by the SCION-[Cu(DDC)$_2$] complex leads to a series of immune responses, including the activation of DCs and the secretion of desired molecular patterns, ultimately resulting in immunogenic cell death. The results of our study show that the SCION-[Cu(DDC)$_2$] complex has the potential to effectively prevent the progression of metastasis and enhance the therapeutic outcomes for patients with metastatic cancer. The promising results of this study provide a basis for

further development and clinical translation of the SCION-[$Cu(DDC)_2$] complex as a promising combined therapeutic approach for cancer treatment.

Chapter 4

Optical Detection of Brain Cell and Neuron Activities Using 3D Plasmonic Micro Antenna Array

4.1 Introduction

Parallel to fluorescence methods, localized surface plasmonic resonances (LSPR) has become a particularly interesting technique for studying the chemistry of living cells. LSPR is a label-free, non-invasive technique, confined to subwavelength-size noble metal nanoparticles that possess large optical cross-sections which have been thoroughly studied.[30,233] The nanoplasmonic structures propose remarkable potential in sensor sensitivity, tuneability, miniaturization, and large-scale fabrication, which makes it possible to intrinsically record neural cell activity at a single neuron level by optical means.

Deciphering the mechanisms of brain and neuron-related activities requires the acquisition of detailed information from a wide range of different scales, ranging from neuron networks to single neuron cells, which means large assemblies of neurons must be monitored on the centimeter scale simultaneously to analyze the collective behavior, while

access to the chemical, sub-cellular, nanoscale of single neurons must be achieved.[274,275] In our study, we directly measured the change of surface electron density on a metal nanoparticle that is induced by the local neural cell's electric field to monitor brain neural activity.

Murine differentiated hippocampal cell line (H19-7) and dissociated hippocampal neurons were observed on our micro-antenna sensing array.[276] After a common preparation of the sensing array surface, differentiated hippocampal cells and dissociated hippocampal neurons were transferred to the sensing surface and furtherly cultured, forming a neuron-network-like in vitro cultured specimen and later treated with different formulations. Firstly, the baseline was set when there was rarely any scattered light change captured before any formulation was injected. However, after the cytokine injection, spiking activities were spotted under the dark field microscope. According to the references, the shape of the signals is typical of results that would be obtained in extracellular electrode recordings. The signal amplitude varied slightly from neuron to neuron.[277] We attribute it to the varying average distance between different neurons and the gold nanoparticle array, as well as the state of activity of the individual neuron.

4.2 Materials and methods

4.2.1 Plamonic 3D microneedle sensing array fabrication

To accomplish the fabrication of a microneedle sensing array of biosensors, we adopted a 3D structure formulated by polystyrene. Because of its low cost, easy processability, biocompatibility, and hydrophobic nature, polystyrene is widely used for biomedical research. First, we designed the desired basal face of the 3D structure and transferred it into a mask. Then, a silicone mode will be manufactured through lithography. By precisely manipulating the etching time, the thickness of the photoresist layer, and the ultraviolet light source, we are able to control the height and shape of the pattern, and finally formed a micro-antenna array to acquire unlimited polydimethylsiloxane (PDMS) microwell masks.[197] With oxygen plasma to make the PDMS microwell mask hydrophilic, a polystyrene solution (20% w/v in toluene) will be cast onto the PDMS mask and covered with indium-doped tin oxide (ITO) coated glass.[6] After degas process and evaporation of the organic solvent, a large-scale sensitive 3D microneedle sensing array will be formed (as shown in Figure.4.1). The tip of our 3D microneedle sensing array will be subsequently coated with gold nanoparticles to serve the sensing purpose with the strong plasmonic coupling can be observed by our previously developed LSPR dark-field imaging technique.[105]

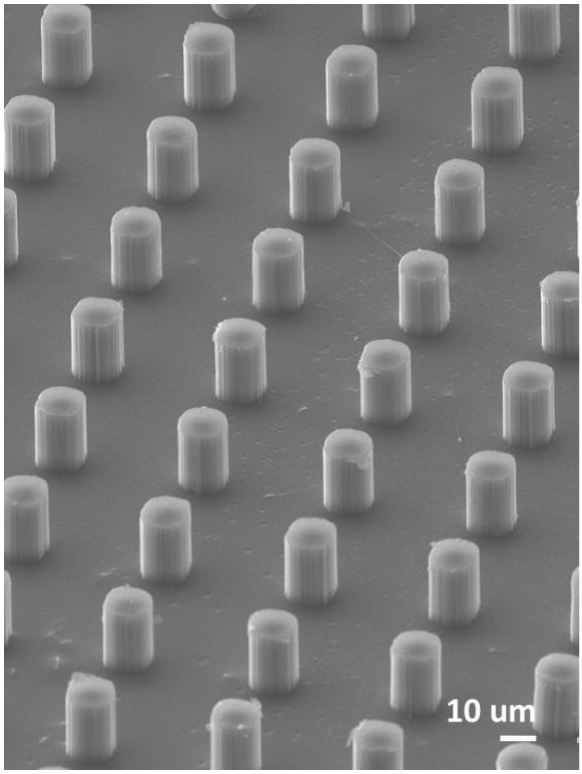

Fig.4.1 SEM image of the sensitive 3D microneedle sensing array.

The sensing area must be millimeter to centimeter-scale so enough neuron cells can be cultured in the micro-electrode arrays so the interaction between them can be recorded. Figure 4.2 shows the large-scale SEM image of our 3D microneedle sensing array. Meanwhile, the biosensing spot needs to be small and separated well from each other to make sure the recording is accurate and precise.

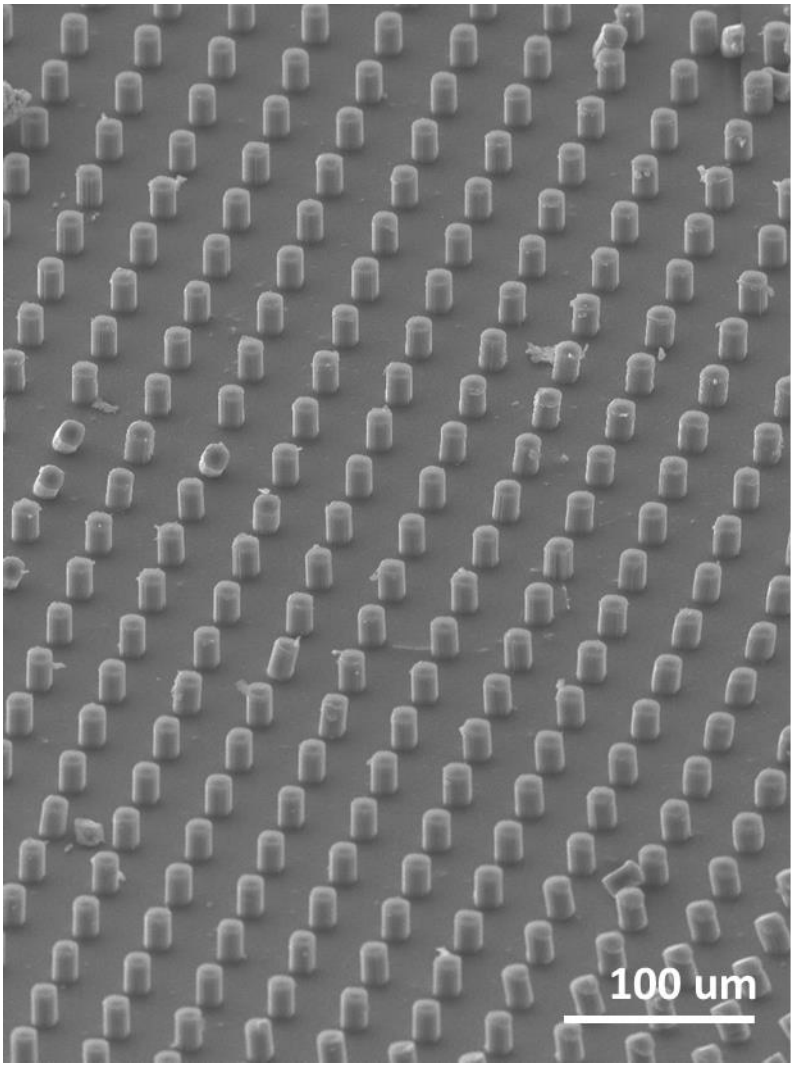

Fig.4.2 SEM image of the large-scale 3D microneedle sensing array.

4.2.2 The microneedle tip coating for LSPR sensing

The tip of the 3D microneedle sensing array will be coated with nanoplasmonic gold nanoparticles, ensuring each microneedle serves as one LSPR "sensing spot". While the electrical signal passes through the neuron cells, the localized concentration of Ca^{2+} at the neuron cell surface will be captured by the sensitive LSPR sensing spot and transferred to

an optical signal (as illustrated in Figure 4.4) based on the LSPR sensing mechanism introduced in Chapters 1 and 2.

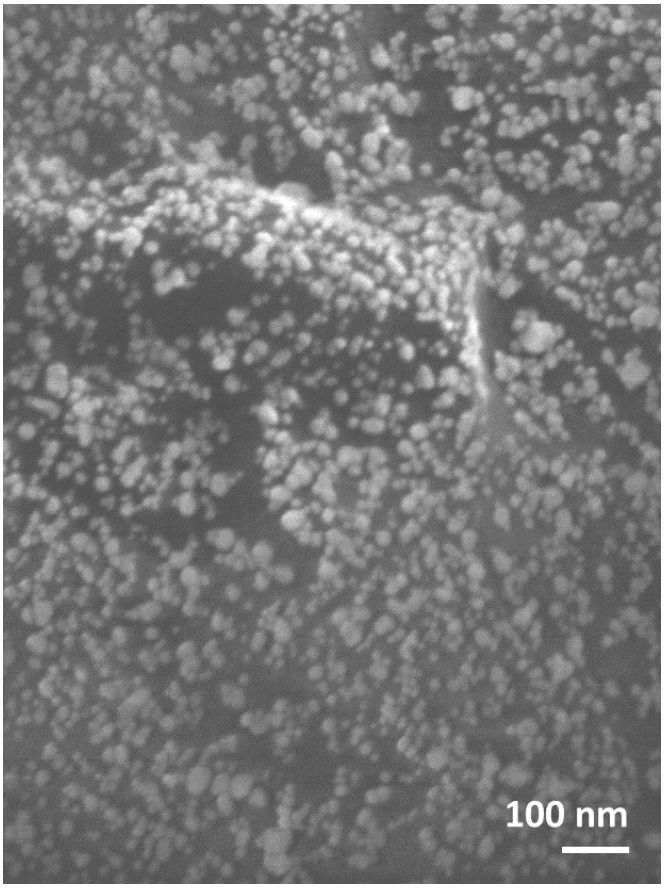

Fig.4.3 SEM image of the surface of the tip from one microneedle. It shows in the image, the surface was coated by well-dispersed gold nanoparticles.

4.2.3 The optical setup for the neuron spiking activities sensing

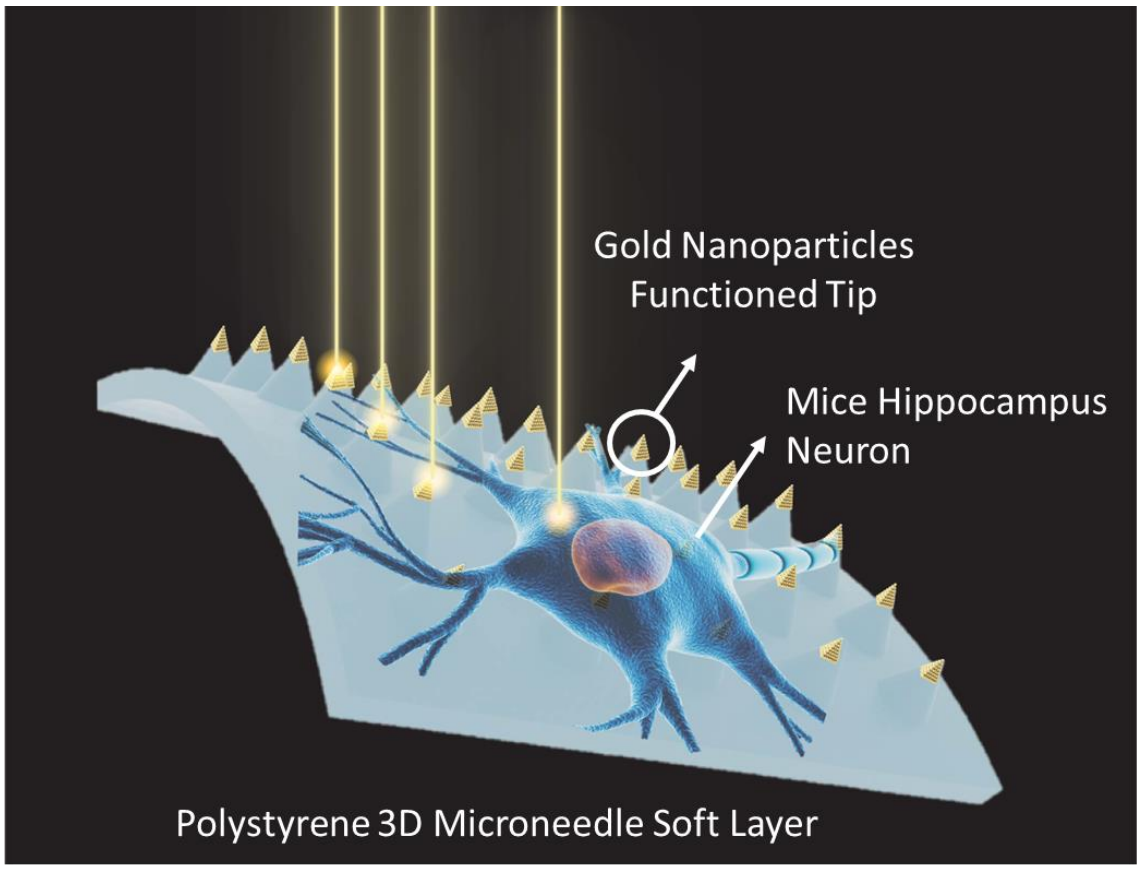

Fig.4.4 Schematic of the LSPR sensing setup for neuron activities 3D microneedle imaging.

The differentiated hippocampal neuron cells were cultured on the prepared microneedle arrays, with the other side of the sensing arrays in contact with the dark-field condenser via silicon oil. The light scattered from the microneedle tip will be collected by an objective lens and imaged by the EMCCD, where the electrical signal passing by, the local microneedle sensing tip should be lightened.[278]

4.3 Results and discussion

4.3.1 Biocompatibility of microneedle patches

Besides the micro-electrode arrays, especially the biosensing spots, need to be renovated, preparing the in vitro cultured neuron cells and finally growing the neuron cells on top of the nanoparticle arrays can also be a challenge.

In preparing the plasmonic nanoparticle templates for the neural cell experiment, the current choice for attempt is the hippocampus cell line from a rat embryo, which can be cultured in “non-processing” status under 34 °C and be differentiated at 37 °C. The differentiation process is quite complicated.

The differentiation design for this study will follow the protocols established in a previous similar study. The hippocampus cells cultured under the "non-processing" status will undergo a specific treatment. They will be subjected to trypsin for a duration of 15 minutes, followed by dissociation through trituration in Hank's balanced salt solution (HBSS) containing 1% 4-(2-hydroxyethyl)-1-piperazineethanesulfonic acid (HEPES) and 1% penicillin-streptomycin. The digestion process will be terminated by changing the HBSS solution to Dulbecco's modified eagle's medium and fetal bovine serum (DMEM/FBS).[279]

Next, the dissociated neurons will be plated onto the plasmonic templates at an average density of approximately five cells per array. These templates will then be placed inside an incubator with a 5% CO_2 environment at a temperature of 37°C. After three hours, the DMEM/FBS solution will be replaced with a serum-free medium containing Neurobasal media, 2% B27 serum-free supplement, 1% Geneticin, and 0.25% Glutamax.

The cells will be fed twice a week using this medium for a duration of two weeks before the actual experiment.

Figure 4.5 shows a microscope image of the dissociated hippocampal neurons cultured on a plasmonic template at 16 days in vitro. The smoothness of the cell bodies and the rich outgrowth of the neuronal "wiring" in the form of axons and dendrites (known as "processes") indicate the health of the neurons, which can be a challenge in preparing in vitro cultured specimens.

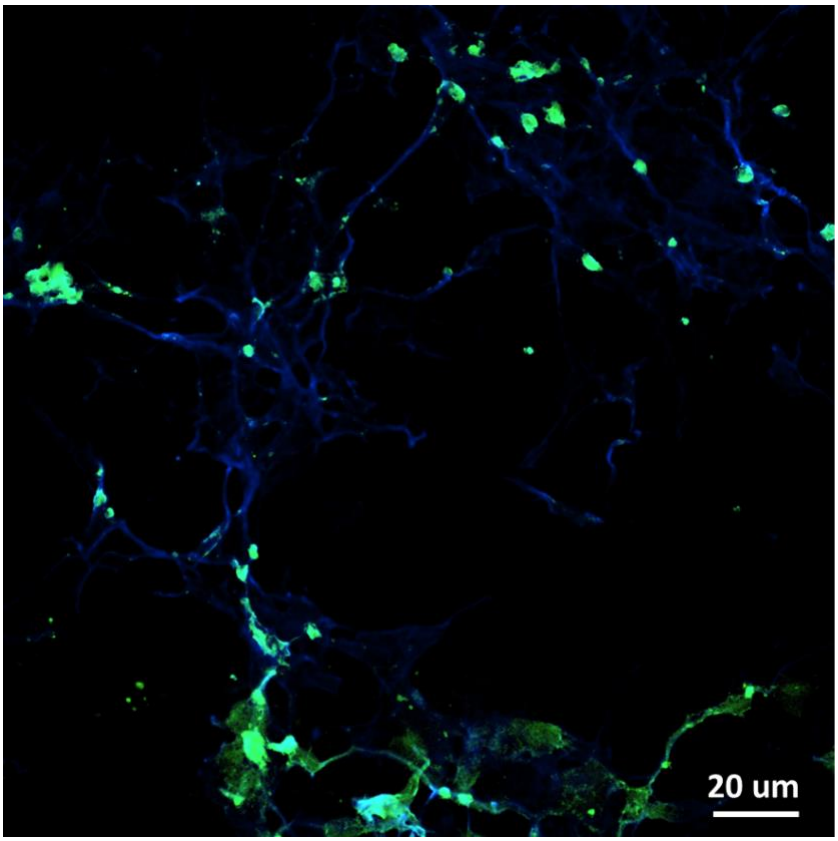

Fig.4.5 Optical microscope image of the hippocampal neuron cells (H19-7 cell line) cultured for 10 days in vitro growth, showing neuron bodies (somas, in green) and axons/dendrites (processes, in blue).

For the experiment, the plasmon/neuron sample was transferred from the incubator into a recording chamber with our 3D microneedle sensing arrays. The neuronal cells displayed excellent adhesion to the device and developed a network with dense arborizations over the passivation layer and micro-structured sensing spots. This observation is indicative of the good biocompatibility of the nanoantennas, and it provides a promising indication of their potential usefulness in neural applications.

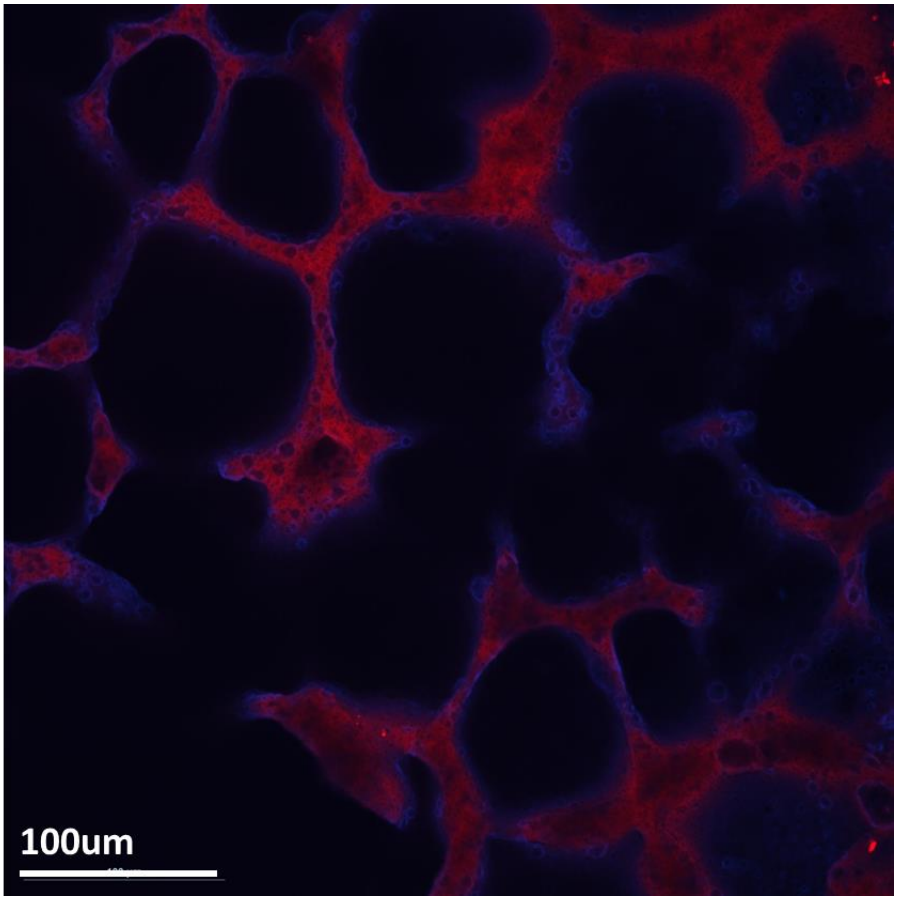

Fig.4.6 The confocal microscopy image of the differentiated hippocampal neuron cells (H19-7 cell line) cultured on the 3D microneedle sensing arrays showing neuron bodies and axons/dendrites.

The high density of arborizations and the intricate network formed by the neurons suggest that they have the ability to establish functional connections with neighboring cells, which is essential for the proper functioning of neural networks. Additionally, the strong adhesion of the neurons to the device ensures that they are firmly anchored to the substrate, offering the opportunity for long-term studies of neuronal activity.

Overall, the good biocompatibility of the microneedles observed in this study is a promising indication of their potential use in neural applications, such as neural interfaces, biosensors, and neural tissue engineering. Further investigations are necessary to fully understand the underlying mechanisms of neuronal adhesion to the microneedles and to optimize their design for specific applications.

4.3,2 The transformation between the electrical and optical signal

In order to quantify and model the LSPR response of the 3D microneedle sensing arrays of gold nanoparticles coated tip in the presence of an applied electric/electrostatic field, the device needs to be designed to house the plasmonic template in the absence of any biological material. There is a model device design and optical measurement setup from the previous study are illustrated in Figure 4.7.

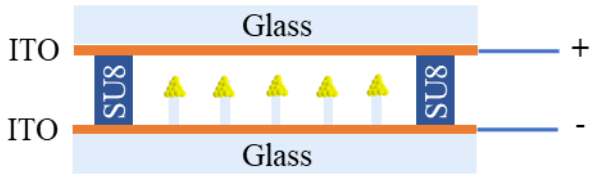

Fig.4.7 Device section illustration for measuring the response of the “bare plasmonic” template to an external electrostatic field. The SU8 polymer spacer ring defines a circular

microchamber filled with air. A modulating potential at 500 Hz was applied between the ITO plates.

The device consisted of two indium tin oxide (ITO)-coated glass substrates with the 3D microneedle sensing arrays in the middle. The two ITO glass slides were separated by a ring structure of SU8, which is a high contrast, epoxy-based photoresist designed for micromachining and other microelectronic applications where a thick chemically and thermally stable image is desired.

To mimic typical neural cell dynamics, a modulation frequency of 500 Hz should be used to apply an electric potential difference between the two ITO substrates using a function generator. This setup will enable us to detect the LSPR response of neuronal signaling between cells on microneedle sensing arrays using a dark field microscope. The collective shift in light intensity will be captured in real-time using an electron-multiplying charge-coupled device (EMCCD) camera. Additionally, a photodiode will be utilized to collect and record the signal into a lock-in amplifier. For future analysis, we will need to customize a program.

4.3.3 The logic behind the customized program for signal processing

To develop a program for analyzing the LSPR signal, we will start by examining the logical algorithm. Similar to the approach outlined in Chapter 2 for establishing a calibration curve for cytokine concentration measurements, we will establish a calibration curve for the differential scattering signals (ΔS/S) from the plasmonic template (refer to Figure 4.6 for the structure illustration) at various applied voltages V_0. The lock-in amplifier will be used to measure the ac signal (ΔS), while an oscilloscope will monitor the dc (V_0=0) signal (S ~ 250 mV). The scattering signal should increase linearly with the applied voltage at a certain rate, which we will define as $\Delta S/SV_0$. To describe the changes in the scattering signal in terms of variations in the applied voltage, we will refer to the model proposed by McIntyre and used by Lioubimov et al. for explaining the changes in (propagating) surface plasmon resonance in a gold film under an oscillating electric potential.

Ignoring the capacitive effects, an applied potential V_0 across the ITO plates induces a surface charge density at the gold surface.

$$\Delta\sigma = -\varepsilon_0 \frac{V_0}{d} \qquad (1)$$

where ε_0 is the electric permittivity of vacuum and d is the distance between the plates (the plasmonic template is assumed to be at ground potential). The surface electron density is elevated as a result of electron transfer from ITO to the gold nanoparticles. Assuming the change in the surface charge density is localized within the Thomas-Fermi screening length d_{TF}, the change in the electron number density N can be written as

$$\Delta N = -\frac{\Delta\sigma}{e d_{TF}} \qquad (2)$$

where e is the elementary charge. The modulation of N leads to a change in the gold plasma frequency $\omega_P^* = (e^2 N/ \varepsilon_0 m^*)^{1/2}$, where m^* is the effective electron mass. The change in ω_P^* can be calculated by

$$\Delta\omega_P^* = \frac{\omega_P^*}{2N}\Delta N \qquad (3)$$

The Drude model is a suitable description of the dielectric function of gold for our intended use.[280,281]

$$\varepsilon(\omega) = \varepsilon_\infty - \frac{\omega_P^{*\,2}}{\omega(\omega + i\gamma)} \qquad (4)$$

The static dielectric constant ε_∞ represents the background polarization originating from the core electrons, while γ denotes the characteristic collision frequency. In the quasi-static approximation, the gold nanoparticles are treated as oblate spheroids with an aspect ratio of 0.25, and their polarizability is determined by

$$\alpha = V\frac{\varepsilon(\omega) - \varepsilon_D}{L[\varepsilon(\omega) - \varepsilon_D] + \varepsilon_D} \qquad (5)$$

where V is the volume of the particle, ε_D is the dielectric constant of the surrounding medium, and L is the geometrical factor in the polarization direction of the incident electromagnetic wave.

For the resonance condition $\mathrm{Re}[\varepsilon(\omega)] = \varepsilon_D\ (L - 1)/L$, the LSPR frequency can be found using equation (4).

$$\omega_{LSP} = \sqrt{\frac{{\omega_P^*}^2}{\varepsilon_\infty + \frac{1-L}{L}} - \gamma^2} \qquad (6)$$

where we assume $\varepsilon_D \sim 1$. The LSPR wavelength will change to

$$\Delta\omega_{LSP} = \frac{\omega_P^*}{\omega_{LSP}(\varepsilon_\infty + \frac{1-L}{L})}\Delta\omega_P^* \qquad (7)$$

Combine equations (1), (2), (3) and (7), the wavelength shift in the LSPR when applied voltage V_0 can be written as

$$\Delta\lambda_{LSP} = -\frac{\varepsilon_0 {\omega_P^*}^2 {\lambda_{LSP}}^3}{8\pi^2 c^2 N e d d_{TF}(\varepsilon_\infty + \frac{1-L}{L})}V_0 \qquad (8)$$

where the c is the speed of light in vacuum.

For the dielectric function of gold, we used the fitting parameters ε_∞ = 9.07, $\hbar\omega_P^*$ = 8.92 eV, and $\hbar\gamma$ = 74 meV ($\hbar$ is Planck's constant divided by 2π) of Vial et al.

Substitute the LSPR wavelength λ_{LSP} of our gold nanoparticles, the electron number density *N*, the distance between the ITO slides d = 100 μm (which is adjustable), the Thomas-Fermi screening length d_{TF} = 0.6 Å, and L which is corresponding to the aspect ratio of our 3D microneedle sensing structure, we will be able to derive the $\frac{\lambda_{LSP}}{V_0}$ from the equation (8).

Given the minimal shift of the LSPR, any alteration in the transmission spectrum shape can be disregarded, and it is reasonable to assume that the entire spectrum shifts uniformly by $\Delta\lambda = \Delta\lambda_{LSP}$. The differential scattering signal can be obtained by approximating the scattered intensity as S = 1 - T, and it is expressed as

$$\frac{\Delta s/s}{V_0} = \frac{\Delta T\, \Delta\lambda_{LSP}}{(1-T)\Delta\lambda V_0} \qquad (10)$$

where $\Delta T/\Delta\lambda$ is the derivative of the transmission spectrum.

The fundamental Stern model was utilized to examine the all-optical signals and characterize the changes in electric potential near the interface of the Au-tip microneedle.[282] The basic Stern model divides the electrolyte solution close to the gold surface into two regions: the electrical double layer (EDL) and the diffuse region. A uniform layer of oppositely charged ions (the Stern layer) forms at a molecular distance (~5 Å) away from the gold surface. The potential change is linear within the EDL region that lies between the metal surface and the Stern layer. The diffuse region, situated beyond the Stern layer, comprises a distribution of ions, where ion concentration decreases gradually with increasing distance from the gold surface, approaching zero. The potential at the Stern layer is defined by:

$$V_s = V_0 - d_S\sqrt{\frac{8k_BTN_i}{\varepsilon_s\varepsilon_0}}\sinh\frac{zeV_s}{2k_BT} \qquad (11)$$

where V_s is the Stern layer potential, V_0 is the surface potential, d_S is the EDL thickness, k_B is the Boltzmann constant, T is the absolute temperature, N_i is the known bulk concentration of ions, ε_s is the static dielectric constant of the electrolyte solution, and z is the valence of the ions. Equation (11) can be solved graphically to find the electric field and the charge density at the gold surface.

The extracellular action potential of a hippocampal neuron near the membrane exhibits experimental values ranging from 100 μV to a few millivolts, which depend on

the physiological features of the neuron, such as membrane resistance, as well as the proximity of the probe to the membrane.

Substitute the theoretical wavelength shift in the resonance $\Delta\lambda_{LSP}$ calculated before

$$\frac{V_0}{d} \rightarrow \frac{\varepsilon_s}{d_S}(V_0 - V_s)$$

$$\frac{1-L}{L} \rightarrow \frac{1-L}{L}\varepsilon_D$$

Using the aforementioned equations, we can determine the theoretical $|\Delta S|/S$ and establish a calibration relationship between the LSPR wavelength shift triggered by our 3D microneedle sensing arrays and neuron spiking activities. This model can then be fine-tuned through experimental data. Once complete, the custom program will accurately output the readout for neuron activity signals.

The measured and calculated scattering changes induced by neural cell spiking have an amplitude on the order of 10^{-3}, which is notably larger than that obtained from the intrinsic (dielectric) birefringence change of the neuron, which is on the order of 10^{-5}. It is noteworthy that the signals obtained from this method are comparable to those obtained from other techniques.

Moreover, it is essential to recognize that one image pre-processes layer was introduced as the initial layer of the image input, serving to subtract the scattering light arising from the height and edge of each microneedle structure. The scattering light ring (depicted in Figure 4.8) should be deemed as background noise in our optical detection procedure. When capturing images on a larger scale, the relative intensity of the scattering light can be significantly higher. Therefore, the elimination of the background before signal

processing can considerably enhance the sensitivity of the gold tip microneedle sensing arrays.

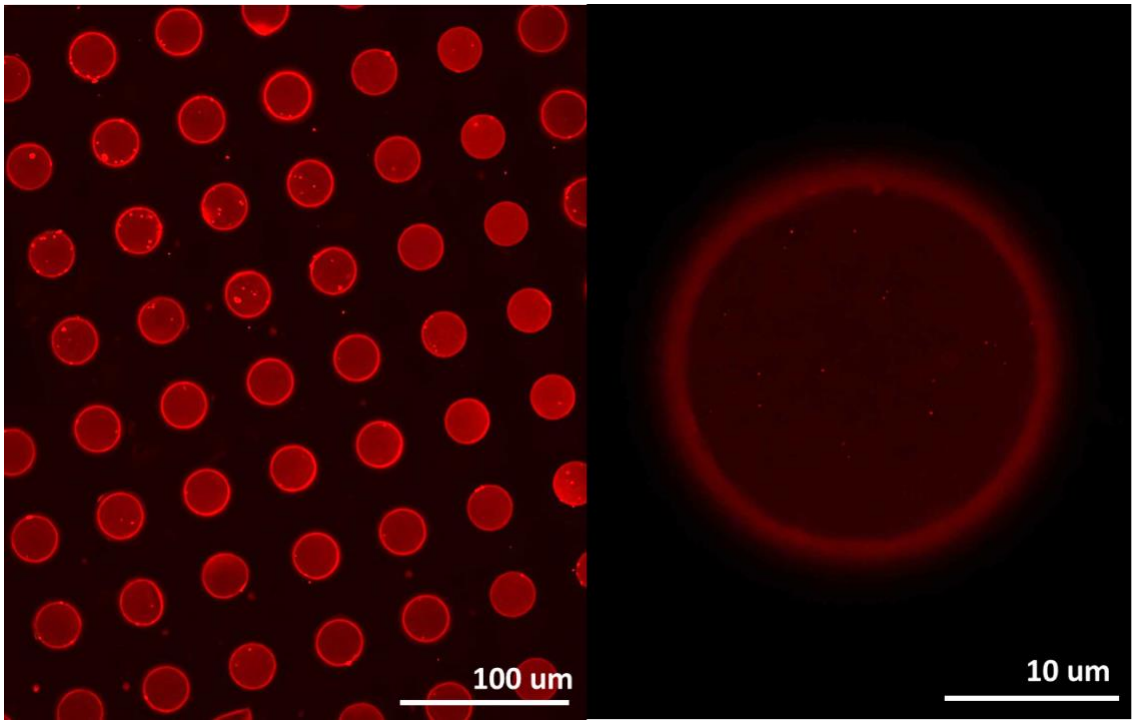

Fig.4.8 The confocal microscopic images of one fixed area of the 3D microneedle sensing arrays. We can tell by comparing the left image and the right image, the background noise (edge scattering light) is becoming more nonnegligible when recording on larger scale.

4.4 Conclusion

We developed and produced 3D microneedle sensing arrays equipped with gold nanoparticles at the tips to detect neuron spiking activities using the LSPR optical detection method. This platform has the potential to be utilized for multiple applications, including neuron cytotoxic screening and the exploration of neuron network formation mechanisms. The sensing structure enables the realization of cell secretion and electrical signal

transmission on a single chip, providing high-resolution, real-time imaging and information regarding the mammalian neuron system.

Chapter 5

Overall Conclusion and Future Direction

The precise monitoring and regulation of the immune response are crucial in cancer and other disease treatments. The immune system is a complex network of different immune cells and proteins that work together to combat pathogens and protect the body. It consists of three primary lines of defense: (i) physical and chemical barriers; (ii) non-specific innate responses; and (iii) specific adaptive responses. Despite the conceptual clarity of the immune system's role, the defense mechanism is not fully understood due to the intricate functional interactions between biomolecules and immune cells.

To access a patient's immune profile, it is crucial to monitor the secretion level of biomolecules such as cytokines, a class of low molecular weight signaling proteins secreted by various cells in the body. Cytokines play a vital role in regulating the activation and inhibition of the immune response. Therefore, monitoring cytokine levels can provide

insight into the transient immune status in different inflammatory diseases, offering guidance for clinical treatment. However, accurately quantifying cytokines can be challenging due to their low levels in circulation and short half-lives. Additionally, clinical samples subjected to repeated freeze-thaw cycles can result in inaccurate cytokine concentration readings. To overcome these challenges, we have demonstrated the development of next-generation point-of-care nanoplasmonic immunoassays in this work. The assay's manufacturing is scalable, and the sensing performance is improved, while the assay time is considerably reduced. This development has the potential to revolutionize the monitoring and regulation of the immune response, providing essential information for clinical treatment. (Chapter 2)

To treat immune-related diseases by regulating a patient's immune response, we aimed to design a combined immunological cancer therapy. In this pursuit, multifunctional superparamagnetic copper iron oxide nanoparticles (SCIONs) were synthesized as drug loads. These SCIONs can be magnetically delivered to the tumor area after injection, where the anti-cancer ingredient and hyperthermia effect work together to eliminate tumor cells, offering a combined therapy to further treat metastatic cancers. The SCIONs generate a substantial amount of local heat when an AMF is applied, leading to the elimination of tumor cells. Additionally, the anti-cancer ingredients continually function in the tumor microenvironment, inducing tumor cell death and apoptosis. The combined therapy has the potential to generate tumor-associated antigens, resulting in the activation of immunological cell death (ICD). The complexes will also inhibit epithelial-mesenchymal transition (EMT), which helps prevent cancer metastasis from occurring. (Chapter 3)

In addition to the immune system, it is essential to pay attention to other systems as well. Regulating the immune response through therapy may cause severe side effects to other systems working within a patient's body. For instance, CAR T cell therapy is an effective cancer immunotherapy, but it can result in a severe side effect called "cytokine release syndrome." When CAR T cell therapy is used to treat brain tumors, the high-level cytokine release may cause an abnormal quantity of cytokines to cross the blood-brain barrier, resulting in damage to the patient's neuron system. Therefore, it is crucial to develop sensors that mimic and monitor other systems, such as establishing a platform for neuron cytotoxic screening. (Chapter 4) Furthermore, accurately simulating the *in vivo* microenvironment *ex vivo* is always important, either for learning the mechanisms in human complex microenvironments or for mapping multicellular dynamics across time and space in the human body.

In the future, I aspire to broaden my research focus and explore the realm of precision medicine. Building on my established research experience in nanomaterials and micro/nanoengineering, as well as my knowledge of cancer biology and immunology, I intend to venture into new research avenues that offer insights into precision medicine. This precise simulation is vital for comprehending the underlying mechanisms governing immune responses in tumor microenvironments, as well as mapping multicellular dynamics over time and space. I aim to incorporate predictive machine learning models in my research to advance the field of precision medicine. The predictive capabilities of a trained program, based on the collection of real-time data, could be instrumental in the advancement of precision medicine. Drawing on my expertise in machine learning and cancer biology, I intend to develop predictive models that could help healthcare

practitioners make personalized and accurate treatment decisions. This approach has the potential to revolutionize precision medicine, contributing to the development of more personalized and effective treatment strategies for patients.

Reference

1 Vert, M. *et al.* Terminology for bio-related polymers and applications (IUPAC Recommendations 2012). *Pure and Applied Chemistry* **84**, 377 - 410 (2012).

2 Yager, P. *et al.* Microfluidic diagnostic technologies for global public health. *Nature* **442**, 412-418 (2006).

3 Pokropivny, V. V. & Skorokhod, V. V. Classification of nanostructures by dimensionality and concept of surface forms engineering in nanomaterial science. *Materials Science and Engineering: C* **27**, 990-993 (2007).

4 Pokropivny, V. V. & Skorokhod, V. V. New dimensionality classifications of nanostructures. *Physica E: Low-dimensional Systems and Nanostructures* **40**, 2521-2525 (2008).

5 Wang, Z., Hu, T., Liang, R. & Wei, M. Application of Zero-Dimensional Nanomaterials in Biosensing. *Front Chem* **8**, 320 (2020).

6 Gao, Z. *et al.* Morphology-Invariant Metallic Nanoparticles with Tunable Plasmonic Properties. *ACS Nano* **15**, 2428-2438 (2021).

7 Gao, Z., Lv, S., Xu, M. & Tang, D. High-index {hk0} faceted platinum concave nanocubes with enhanced peroxidase-like activity for an ultrasensitive colorimetric immunoassay of the human prostate-specific antigen. *Analyst* **142**, 911-917 (2017).

8 Ogueri, K. S. & Laurencin, C. T. Nanofiber Technology for Regenerative Engineering. *ACS Nano* **14**, 9347-9363 (2020).

9 VahidMohammadi, A., Mojtabavi, M., Caffrey, N. M., Wanunu, M. & Beidaghi, M. Assembling 2D MXenes into Highly Stable Pseudocapacitive Electrodes with High Power and Energy Densities. *Adv Mater* **31**, e1806931 (2019).

10 Cha, C., Shin, S. R., Annabi, N., Dokmeci, M. R. & Khademhosseini, A. Carbon-Based Nanomaterials: Multifunctional Materials for Biomedical Engineering. *ACS Nano* **7**, 2891-2897 (2013).

11 Navrotsky, A. Thermodynamics of solid electrolytes and related oxide ceramics based on the fluorite structure. *Journal of Materials Chemistry* **20**, 10577-10587 (2010).

12 Han, J. *et al.* Polymer-Based Nanomaterials and Applications for Vaccines and Drugs. *Polymers* **10**, 31 (2018).

13 Ahmadi, A. *et al.* Recent advances in ultrasound-triggered drug delivery through lipid-based nanomaterials. *Drug Discovery Today* **25**, 2182-2200 (2020).

14 Makvandi, P. *et al.* Metal-Based Nanomaterials in Biomedical Applications: Antimicrobial Activity and Cytotoxicity Aspects. *Advanced Functional Materials* **30**, 1910021 (2020).

15 Ando, T. The electronic properties of graphene and carbon nanotubes. *NPG Asia Materials* **1**, 17-21 (2009).

16 Grosskopf, A. K. *et al.* Viscoplastic Matrix Materials for Embedded 3D Printing. *ACS Applied Materials & Interfaces* **10**, 23353-23361 (2018).

17 Rethi, L. *et al.* Lipid-Based Nanomaterials for Drug Delivery Systems in Breast Cancer Therapy. *Nanomaterials* **12**, 2948 (2022).

18 García-Pinel, B. *et al.* Lipid-Based Nanoparticles: Application and Recent Advances in Cancer Treatment. *Nanomaterials* **9**, 638 (2019).

19 Pardi, N., Hogan, M. J., Porter, F. W. & Weissman, D. mRNA vaccines — a new era in vaccinology. *Nature Reviews Drug Discovery* **17**, 261-279 (2018).

20 Khlebtsov, N. G. & Dykman, L. A. Optical properties and biomedical applications of plasmonic nanoparticles. *Journal of Quantitative Spectroscopy and Radiative Transfer* **111**, 1-35 (2010).

21 Huang, X. & El-Sayed, M. A. Plasmonic photo-thermal therapy (PPTT). *Alexandria Journal of Medicine* **47**, 1-9 (2011).

22 Mayer, K. M. & Hafner, J. H. Localized surface plasmon resonance sensors. *Chemical reviews* **111**, 3828-3857 (2011).

23 Xiao, Y. & Du, J. Superparamagnetic nanoparticles for biomedical applications. *Journal of Materials Chemistry B* **8**, 354-367 (2020).

24 Neuberger, T., Schöpf, B., Hofmann, H., Hofmann, M. & von Rechenberg, B. Superparamagnetic nanoparticles for biomedical applications: Possibilities and limitations of a new drug delivery system. *Journal of Magnetism and Magnetic Materials* **293**, 483-496 (2005).

25 Gupta, A. K. & Wells, S. Surface-modified superparamagnetic nanoparticles for drug delivery: preparation, characterization, and cytotoxicity studies. *IEEE Transactions on NanoBioscience* **3**, 66-73 (2004).

26 Hou, W. & Cronin, S. B. A Review of Surface Plasmon Resonance-Enhanced Photocatalysis. *Advanced Functional Materials* **23**, 1612-1619 (2013).

27 Barnes, W. L., Dereux, A. & Ebbesen, T. W. Surface plasmon subwavelength optics. *Nature* **424**, 824-830 (2003).

28 Homola, J., Yee, S. S. & Gauglitz, G. Surface plasmon resonance sensors: review. *Sensors and Actuators B: Chemical* **54**, 3-15 (1999).

29 Chen, Y. & Ming, H. Review of surface plasmon resonance and localized surface plasmon resonance sensor. *Photonic Sensors* **2**, 37-49 (2012).

30 Chen, P. *et al.* Multiplex serum cytokine immunoassay using nanoplasmonic biosensor microarrays. *ACS Nano* **9**, 4173-4181 (2015).

31 Kim, D. M., Park, J. S., Jung, S.-W., Yeom, J. & Yoo, S. M. Biosensing Applications Using Nanostructure-Based Localized Surface Plasmon Resonance Sensors. *Sensors* **21**, 3191 (2021).

32 Zhang, X. *et al.* Spoof Localized Surface Plasmons for Sensing Applications. *Advanced Materials Technologies* **6**, 2000863 (2021).

33 Wang, C., Cai, Y., MacLachlan, A. & Chen, P. Novel Nanoplasmonic-Structure-Based Integrated Microfluidic Biosensors for Label-Free In Situ Immune Functional Analysis: A review of recent progress. *IEEE Nanotechnology Magazine* **14**, 46-C43 (2020).

34 Vogel, N. *et al.* Reusable Localized Surface Plasmon Sensors Based on Ultrastable Nanostructures. *Small* **6**, 104-109 (2010).

35 Anatoly, V. Z. & Igor, I. S. Near-field photonics: surface plasmon polaritons and localized surface plasmons. *Journal of Optics A: Pure and Applied Optics* **5**, S16 (2003).

36 McBane, R. D. *et al.* Importance of Device Evaluation for Point-of-Care Prothrombin Time International Normalized Ratio Testing Programs. *Mayo Clinic Proceedings* **80**, 181-186 (2005).

37 Wang, C. *et al.* Point-of-care diagnostics for infectious diseases: From methods to devices. *Nano Today* **37**, 101092 (2021).

38 Yetisen, A. K., Akram, M. S. & Lowe, C. R. Paper-based microfluidic point-of-care diagnostic devices. *Lab on a Chip* **13**, 2210-2251 (2013).

39 Brolo, A. G. Plasmonics for future biosensors. *Nature Photonics* **6**, 709-713 (2012).

40 Borisov, S. M. & Wolfbeis, O. S. Optical Biosensors. *Chemical Reviews* **108**, 423-461 (2008).

41 Lowe, C. R. Biosensors. *Trends in Biotechnology* **2**, 59-65 (1984).

42 Kissinger, P. T. Biosensors—a perspective. *Biosensors and Bioelectronics* **20**, 2512-2516 (2005).

43 Di Nardo, F., Chiarello, M., Cavalera, S., Baggiani, C. & Anfossi, L. Ten Years of Lateral Flow Immunoassay Technique Applications: Trends, Challenges and Future Perspectives. *Sensors* **21**, 5185 (2021).

44 Wang, D. *et al.* Rapid lateral flow immunoassay for the fluorescence detection of SARS-CoV-2 RNA. *Nature Biomedical Engineering* **4**, 1150-1158 (2020).

45 Porstmann, T. & Kiessig, S. T. Enzyme immunoassay techniques an overview. *Journal of Immunological Methods* **150**, 5-21 (1992).

46 Mohanty, S. P. & Kougianos, E. Biosensors: a tutorial review. *IEEE Potentials* **25**, 35-40 (2006).

47 Metkar, S. K. & Girigoswami, K. Diagnostic biosensors in medicine – A review. *Biocatalysis and Agricultural Biotechnology* **17**, 271-283 (2019).

48 Schotter, J. *et al.* Comparison of a prototype magnetoresistive biosensor to standard fluorescent DNA detection. *Biosensors and Bioelectronics* **19**, 1149-1156 (2004).

49 Wang, M. *et al.* A wearable electrochemical biosensor for the monitoring of metabolites and nutrients. *Nature Biomedical Engineering* **6**, 1225-1235 (2022).

50 Heineman, W. R. & Jensen, W. B. Leland C. Clark Jr. (1918–2005). *Biosensors and Bioelectronics* **21**, 1403-1404 (2006).

51 Scheller, F. W. *et al.* Second generation biosensors. *Biosensors and Bioelectronics* **6**, 245-253 (1991).

52 Liedberg, B., Nylander, C. & Lundström, I. Biosensing with surface plasmon resonance — how it all started. *Biosensors and Bioelectronics* **10**, i-ix (1995).

53 Syahir, A., Usui, K., Tomizaki, K.-y., Kajikawa, K. & Mihara, H. Label and Label-Free Detection Techniques for Protein Microarrays. *Microarrays* **4**, 228-244 (2015).

54 Sakamoto, S. *et al.* Enzyme-linked immunosorbent assay for the quantitative/qualitative analysis of plant secondary metabolites. *Journal of Natural Medicines* **72**, 32-42 (2018).

55 Lequin, R. M. Enzyme Immunoassay (EIA)/Enzyme-Linked Immunosorbent Assay (ELISA). *Clinical Chemistry* **51**, 2415-2418 (2005).

56 Mendoza, L. G. *et al.* High-Throughput Microarray-Based Enzyme-Linked Immunosorbent Assay (ELISA). *BioTechniques* **27**, 778-788 (1999).

57 Tamura, T. & Hamachi, I. Recent Progress in Design of Protein-Based Fluorescent Biosensors and Their Cellular Applications. *ACS Chemical Biology* **9**, 2708-2717 (2014).

58 Krishnan, S. K., Singh, E., Singh, P., Meyyappan, M. & Nalwa, H. S. A review on graphene-based nanocomposites for electrochemical and fluorescent biosensors. *RSC Advances* **9**, 8778-8881 (2019).

59 Chen, J. *et al.* A SiO2 NP–DNA/silver nanocluster sandwich structure-enhanced fluorescence polarization biosensor for amplified detection of hepatitis B virus DNA. *Journal of Materials Chemistry B* **3**, 964-967 (2015).

60 Wen, J., Xu, Y., Li, H., Lu, A. & Sun, S. Recent applications of carbon nanomaterials in fluorescence biosensing and bioimaging. *Chemical Communications* **51**, 11346-11358 (2015).

61 Hsing, I.-M., Xu, Y. & Zhao, W. Micro- and Nano- Magnetic Particles for Applications in Biosensing. *Electroanalysis* **19**, 755-768 (2007).

62 Marquette, C. A. & Blum, L. J. Electro-chemiluminescent biosensing. *Analytical and Bioanalytical Chemistry* **390**, 155-168 (2008).

63 Marquette, C. A. & Blum, L. J. Applications of the luminol chemiluminescent reaction in analytical chemistry. *Analytical and Bioanalytical Chemistry* **385**, 546-554 (2006).

64 Giannetti, A. & Bocková, M. Optical Chemosensors and Biosensors. *Chemosensors* **8**, 33 (2020).

65 Singh, A. *et al.* Recent Advances in Electrochemical Biosensors: Applications, Challenges, and Future Scope. *Biosensors* **11**, 336 (2021).

66 Cho, I.-H., Kim, D. H. & Park, S. Electrochemical biosensors: perspective on functional nanomaterials for on-site analysis. *Biomaterials Research* **24**, 6 (2020).

67 Kour, R. *et al.* Review—Recent Advances in Carbon Nanomaterials as Electrochemical Biosensors. *Journal of The Electrochemical Society* **167**, 037555 (2020).

68 Cesewski, E. & Johnson, B. N. Electrochemical biosensors for pathogen detection. *Biosensors and Bioelectronics* **159**, 112214 (2020).

69 Valverde, A. *et al.* Phage-Derived and Aberrant HaloTag Peptides Immobilized on Magnetic Microbeads for Amperometric Biosensing of Serum Autoantibodies and Alzheimer's Disease Diagnosis. *Analysis & Sensing* **1**, 161-165 (2021).

70 Xu, L. *et al.* Optical, electrochemical and electrical (nano)biosensors for detection of exosomes: A comprehensive overview. *Biosensors and Bioelectronics* **161**, 112222 (2020).

71 Man, Y. *et al.* An anchored monopodial DNA walker triggered by proximity hybridization for amplified amperometric biosensing of nucleic acid and protein. *Analytica Chimica Acta* **1107**, 48-54 (2020).

72 Fu, Z., Lu, Y.-C. & Lai, J. J. Recent Advances in Biosensors for Nucleic Acid and Exosome Detection. *cmj* **55**, 86-98 (2019).

73 Huerta-Nuñez, L. *et al.* A biosensor capable of identifying low quantities of breast cancer cells by electrical impedance spectroscopy. *Scientific reports* **9**, 1-12 (2019).

74 Kiew, L.-V. *et al.* Development of flexible electrochemical impedance spectroscopy-based biosensing platform for rapid screening of SARS-CoV-2 inhibitors. *Biosensors and Bioelectronics* **183**, 113213 (2021).

75 Magar, H. S., Hassan, R. Y. & Mulchandani, A. Electrochemical impedance spectroscopy (EIS): Principles, construction, and biosensing applications. *Sensors* **21**, 6578 (2021).

76 Park, H. *et al.* Ultrasensitive and selective field-effect transistor-based biosensor created by rings of MoS2 Nanopores. *ACS nano* **16**, 1826-1835 (2021).

77 Syedmoradi, L., Ahmadi, A., Norton, M. L. & Omidfar, K. A review on nanomaterial-based field effect transistor technology for biomarker detection. *Microchimica Acta* **186**, 1-23 (2019).

78 Uzunoglu, D., Altunbek, M., Kuku, G. & Culha, M. in *Single-cell omics* 153-177 (Elsevier, 2019).

79 Tang, W., Wang, D., Xu, Y., Li, N. & Liu, F. A self-assembled DNA nanostructure-amplified quartz crystal microbalance with dissipation biosensing platform for nucleic acids. *Chemical Communications* **48**, 6678-6680 (2012).

80 Länge, K., Rapp, B. E. & Rapp, M. Surface acoustic wave biosensors: a review. *Analytical and bioanalytical chemistry* **391**, 1509-1519 (2008).

81 Ding, X. *et al.* Surface acoustic wave microfluidics. *Lab on a Chip* **13**, 3626-3649 (2013).

82 Yeo, L. Y. & Friend, J. R. Surface acoustic wave microfluidics. *Annual review of fluid mechanics* **46**, 379-406 (2014).

83 Griffin, N. M. *et al.* Label-free, normalized quantification of complex mass spectrometry data for proteomic analysis. *Nature biotechnology* **28**, 83-89 (2010).

84 Neilson, K. A. *et al.* Less label, more free: approaches in label-free quantitative mass spectrometry. *Proteomics* **11**, 535-553 (2011).

85 Callister, S. J. *et al.* Normalization approaches for removing systematic biases associated with mass spectrometry and label-free proteomics. *Journal of proteome research* **5**, 277-286 (2006).

86 Hillenkamp, F., Karas, M., Beavis, R. C. & Chait, B. T. Matrix-assisted laser desorption/ionization mass spectrometry of biopolymers. *Analytical chemistry* **63**, 1193A-1203A (1991).

87 Seng, P. *et al.* Ongoing revolution in bacteriology: routine identification of bacteria by matrix-assisted laser desorption ionization time-of-flight mass spectrometry. *Clinical Infectious Diseases* **49**, 543-551 (2009).

88 Bizzini, A. & Greub, G. Matrix-assisted laser desorption ionization time-of-flight mass spectrometry, a revolution in clinical microbial identification. *Clinical Microbiology and infection* **16**, 1614-1619 (2010).

89 Damborský, P., Švitel, J. & Katrlík, J. Optical biosensors. *Essays in biochemistry* **60**, 91-100 (2016).

90 Baird, C. L. & Myszka, D. G. Current and emerging commercial optical biosensors. *Journal of molecular recognition* **14**, 261-268 (2001).

91 Dorfner, D. *et al.* Photonic crystal nanostructures for optical biosensing applications. *Biosensors and Bioelectronics* **24**, 3688-3692 (2009).

92 Pal, S., Guillermain, E., Sriram, R., Miller, B. L. & Fauchet, P. M. Silicon photonic crystal nanocavity-coupled waveguides for error-corrected optical biosensing. *Biosensors and Bioelectronics* **26**, 4024-4031 (2011).

93 Sharma, S., Kumari, R., Varshney, S. K. & Lahiri, B. Optical biosensing with electromagnetic nanostructures. *Reviews in Physics* **5**, 100044 (2020).

94 Foreman, M. R., Swaim, J. D. & Vollmer, F. Whispering gallery mode sensors. *Advances in optics and photonics* **7**, 168-240 (2015).

95 Vollmer, F. & Arnold, S. Whispering-gallery-mode biosensing: label-free detection down to single molecules. *Nature methods* **5**, 591-596 (2008).

96 Toropov, N. *et al.* Review of biosensing with whispering-gallery mode lasers. *Light: Science & Applications* **10**, 42 (2021).

97 Mejía-Salazar, J. & Oliveira Jr, O. N. Plasmonic biosensing: Focus review. *Chemical reviews* **118**, 10617-10625 (2018).

98 Jebelli, A., Oroojalian, F., Fathi, F., Mokhtarzadeh, A. & de la Guardia, M. Recent advances in surface plasmon resonance biosensors for microRNAs detection. *Biosensors and Bioelectronics* **169**, 112599 (2020).

99 Rezabakhsh, A., Rahbarghazi, R. & Fathi, F. Surface plasmon resonance biosensors for detection of Alzheimer's biomarkers; an effective step in early and accurate diagnosis. *Biosensors and Bioelectronics* **167**, 112511 (2020).

100 Falkowski, P., Lukaszewski, Z. & Gorodkiewicz, E. Potential of surface plasmon resonance biosensors in cancer detection. *Journal of Pharmaceutical and Biomedical Analysis* **194**, 113802 (2021).

101 Sarkar, M. *et al.* Hybrid plasmonic mode by resonant coupling of localized plasmons to propagating plasmons in a Kretschmann configuration. *Acs Photonics* **2**, 237-245 (2015).

102 Kim, H.-M. *et al.* Localized surface plasmon resonance biosensor using nanopatterned gold particles on the surface of an optical fiber. *Sensors and Actuators B: Chemical* **280**, 183-191 (2019).

103 Willets, K. A. & Van Duyne, R. P. Localized surface plasmon resonance spectroscopy and sensing. *Annu. Rev. Phys. Chem.* **58**, 267-297 (2007).

104 Banerjee, R. & Jaiswal, A. Recent advances in nanoparticle-based lateral flow immunoassay as a point-of-care diagnostic tool for infectious agents and diseases. *Analyst* **143**, 1970-1996 (2018).

105 Cai, Y. *et al.* Magnet Patterned Superparamagnetic Fe3O4/Au Core–Shell Nanoplasmonic Sensing Array for Label-Free High Throughput Cytokine Immunoassay. *Advanced Healthcare Materials* **8**, 1801478 (2019).

106 Presta, L. G. Antibody engineering. *Current Opinion in Structural Biology* **2**, 593-596 (1992).

107 Nelson, A. L., Dhimolea, E. & Reichert, J. M. Development trends for human monoclonal antibody therapeutics. *Nature reviews drug discovery* **9**, 767-774 (2010).

108 Liu, H. *et al.* in *MAbs.* 1145-1154 (Taylor & Francis).

109 Boulianne, G. L., Hozumi, N. & Shulman, M. J. Production of functional chimaeric mouse/human antibody. *Nature* **312**, 643-646 (1984).

110 Birch, J. R. & Racher, A. J. Antibody production. *Advanced drug delivery reviews* **58**, 671-685 (2006).

111 Lu, R.-M. *et al.* Development of therapeutic antibodies for the treatment of diseases. *Journal of biomedical science* **27**, 1-30 (2020).

112 Sahin, U. *et al.* COVID-19 vaccine BNT162b1 elicits human antibody and TH1 T cell responses. *Nature* **586**, 594-599 (2020).

113 Pillay, T. S. & Muyldermans, S. Application of single-domain antibodies ("nanobodies") to laboratory diagnosis. *Ann Lab Med* **41**, 549-558 (2021).

114 Zebardast, A., Hosseini, P., Hasanzadeh, A. & Latifi, T. The role of single-domain antibodies (or nanobodies) in SARS-CoV-2 neutralization. *Molecular Biology Reports* **49**, 647-656 (2022).

115 Voss, J. E. (Nature Publishing Group UK London, 2021).

116 Basso, A. & Serban, S. Industrial applications of immobilized enzymes—A review. *Molecular Catalysis* **479**, 110607 (2019).

117 Tu, J., Torrente-Rodríguez, R. M., Wang, M. & Gao, W. The era of digital health: A review of portable and wearable affinity biosensors. *Advanced Functional Materials* **30**, 1906713 (2020).

118 Jia, Y., Sun, S., Cui, X., Wang, X. & Yang, L. Enzyme-like catalysis of polyoxometalates for chemiluminescence: Application in ultrasensitive detection of H2O2 and blood glucose. *Talanta* **205**, 120139 (2019).

119 Samanta, D., Ebrahimi, S. B. & Mirkin, C. A. Nucleic-acid structures as intracellular probes for live cells. *Advanced Materials* **32**, 1901743 (2020).

120 Chen, Y. *et al.* Nucleic acid amplification free biosensors for pathogen detection. *Biosensors and Bioelectronics* **153**, 112049 (2020).

121 Zhang, T., Tian, T. & Lin, Y. Functionalizing framework nucleic-acid-based nanostructures for biomedical application. *Advanced Materials* **34**, 2107820 (2022).

122 Kumar Kulabhusan, P., Hussain, B. & Yüce, M. Current perspectives on aptamers as diagnostic tools and therapeutic agents. *Pharmaceutics* **12**, 646 (2020).

123 Zou, X., Wu, J., Gu, J., Shen, L. & Mao, L. Application of aptamers in virus detection and antiviral therapy. *Frontiers in microbiology* **10**, 1462 (2019).

124 Song, Y. *et al.* Discovery of aptamers targeting the receptor-binding domain of the SARS-CoV-2 spike glycoprotein. *Analytical chemistry* **92**, 9895-9900 (2020).

125 Xu, Y. *et al.* Systematic evolution of ligands by exponential enrichment technologies and aptamer-based applications: Recent progress and challenges in precision medicine of infectious diseases. *Frontiers in Bioengineering and Biotechnology* **9**, 704077 (2021).

126 Rosch, J. C., Balikov, D. A., Gong, F. & Lippmann, E. S. A systematic evolution of ligands by exponential enrichment workflow with consolidated counterselection to efficiently isolate high-affinity aptamers. *Engineering Reports* **2**, e12089 (2020).

127 Fares, J., Fares, M. Y., Khachfe, H. H., Salhab, H. A. & Fares, Y. Molecular principles of metastasis: a hallmark of cancer revisited. *Signal transduction and targeted therapy* **5**, 28 (2020).

128 Weigelt, B., Peterse, J. L. & Van't Veer, L. J. Breast cancer metastasis: markers and models. *Nature reviews cancer* **5**, 591-602 (2005).

129 O'Shaughnessy, J. *et al.* Iniparib plus chemotherapy in metastatic triple-negative breast cancer. *New England Journal of Medicine* **364**, 205-214 (2011).

130 O'Shaughnessy, J. Extending survival with chemotherapy in metastatic breast cancer. *The oncologist* **10**, 20-29 (2005).

131 Hryniuk, W. & Bush, H. The importance of dose intensity in chemotherapy of metastatic breast cancer. *Journal of Clinical Oncology* **2**, 1281-1288 (1984).

132 Mellman, I., Coukos, G. & Dranoff, G. Cancer immunotherapy comes of age. *Nature* **480**, 480-489 (2011).

133 Couzin-Frankel, J. (American Association for the Advancement of Science, 2013).

134 Wei, S. C., Duffy, C. R. & Allison, J. P. Fundamental mechanisms of immune checkpoint blockade TherapyFundamental mechanisms of immune checkpoint blockade therapy. *Cancer discovery* **8**, 1069-1086 (2018).

135 Auslander, N. *et al.* Robust prediction of response to immune checkpoint blockade therapy in metastatic melanoma. *Nature medicine* **24**, 1545-1549 (2018).

136 Hargadon, K. M., Johnson, C. E. & Williams, C. J. Immune checkpoint blockade therapy for cancer: an overview of FDA-approved immune checkpoint inhibitors. *International immunopharmacology* **62**, 29-39 (2018).

137 Zhao, X. & Subramanian, S. Intrinsic Resistance of Solid Tumors to Immune Checkpoint Blockade TherapyResistance to Immune Checkpoint Blockade Therapy. *Cancer research* **77**, 817-822 (2017).

138 Sunshine, J. & Taube, J. M. Pd-1/pd-l1 inhibitors. *Current opinion in pharmacology* **23**, 32-38 (2015).

139 Champiat, S. *et al.* Hyperprogressive Disease Is a New Pattern of Progression in Cancer Patients Treated by Anti-PD-1/PD-L1Hyperprogressive Disease with Anti-PD-1/PD-L1 Therapy. *Clinical Cancer Research* **23**, 1920-1928 (2017).

140 Chen, L. & Han, X. Anti–PD-1/PD-L1 therapy of human cancer: past, present, and future. *The Journal of clinical investigation* **125**, 3384-3391 (2015).

141 Oosterwegel, M. A. *et al.* The role of CTLA-4 in regulating Th2 differentiation. *The Journal of Immunology* **163**, 2634-2639 (1999).

142 Mandelbrot, D. A., McAdam, A. J. & Sharpe, A. H. B7-1 or B7-2 is required to produce the lymphoproliferative phenotype in mice lacking cytotoxic T lymphocyte–associated antigen 4 (CTLA-4). *The Journal of experimental medicine* **189**, 435-440 (1999).

143 Ying, H. *et al.* Cutting edge: CTLA-4–B7 interaction suppresses Th17 cell differentiation. *The Journal of Immunology* **185**, 1375-1378 (2010).

144 Webster, R. M. The immune checkpoint inhibitors: where are we now? *Nature reviews. Drug discovery* **13**, 883 (2014).

145 Shek, D. *et al.* Immune-checkpoint inhibitors for advanced hepatocellular carcinoma: a synopsis of response rates. *The Oncologist* **26**, e1216-e1225 (2021).

146 Tran, E. *et al.* T-cell transfer therapy targeting mutant KRAS in cancer. *New England Journal of Medicine* **375**, 2255-2262 (2016).

147 Rosenberg, S. A., Spiess, P. & Lafreniere, R. A new approach to the adoptive immunotherapy of cancer with tumor-infiltrating lymphocytes. *Science* **233**, 1318-1321 (1986).

148 Zhao, Y. *et al.* Tumor infiltrating lymphocyte (TIL) therapy for solid tumor treatment: progressions and challenges. *Cancers* **14**, 4160 (2022).

149 Sterner, R. C. & Sterner, R. M. CAR-T cell therapy: current limitations and potential strategies. *Blood cancer journal* **11**, 69 (2021).

150 Shah, N. N. & Fry, T. J. Mechanisms of resistance to CAR T cell therapy. *Nature reviews Clinical oncology* **16**, 372-385 (2019).

151 Chavez, J. C., Bachmeier, C. & Kharfan-Dabaja, M. A. CAR T-cell therapy for B-cell lymphomas: clinical trial results of available products. *Therapeutic advances in hematology* **10**, 2040620719841581 (2019).

152 Santomasso, B. D. *et al.* Clinical and biological correlates of neurotoxicity associated with CAR T-cell therapy in patients with b-cell acute lymphoblastic LeukemiaBiomarkers of neurotoxicity in CD19 CAR T cell therapy. *Cancer discovery* **8**, 958-971 (2018).

153 Stanton, S. E. & Disis, M. L. Clinical significance of tumor-infiltrating lymphocytes in breast cancer. *Journal for immunotherapy of cancer* **4**, 1-7 (2016).

154 Lee, W. S., Park, S., Lee, W. Y., Yun, S. H. & Chun, H. K. Clinical impact of tumor-infiltrating lymphocytes for survival in stage II colon cancer. *Cancer* **116**, 5188-5199 (2010).

155 Pruneri, G. *et al.* Clinical validity of tumor-infiltrating lymphocytes analysis in patients with triple-negative breast cancer. *Annals of oncology* **27**, 249-256 (2016).

156 Amini, L. *et al.* Preparing for CAR T cell therapy: patient selection, bridging therapies and lymphodepletion. *Nature Reviews Clinical Oncology* **19**, 342-355 (2022).

157 Wang, M. *et al.* KTE-X19 CAR T-cell therapy in relapsed or refractory mantle-cell lymphoma. *New England journal of medicine* **382**, 1331-1342 (2020).

158 Mikkilineni, L. & Kochenderfer, J. N. CAR T cell therapies for patients with multiple myeloma. *Nature reviews Clinical oncology* **18**, 71-84 (2021).

159 Rafiq, S., Hackett, C. S. & Brentjens, R. J. Engineering strategies to overcome the current roadblocks in CAR T cell therapy. *Nature reviews Clinical oncology* **17**, 147-167 (2020).

160 Fu, C. *et al.* Tumor-associated antigens: Tn antigen, sTn antigen, and T antigen. *Hla* **88**, 275-286 (2016).

161 Saxena, M. & Bhardwaj, N. Re-emergence of dendritic cell vaccines for cancer treatment. *Trends in cancer* **4**, 119-137 (2018).

162 Banchereau, J. & Palucka, A. K. Dendritic cells as therapeutic vaccines against cancer. *Nature Reviews Immunology* **5**, 296-306 (2005).

163 Palucka, K. & Banchereau, J. Dendritic-cell-based therapeutic cancer vaccines. *Immunity* **39**, 38-48 (2013).

164 Rusek, A. M. *et al.* MicroRNA modulators of epigenetic regulation, the tumor microenvironment and the immune system in lung cancer. *Molecular cancer* **14**, 1-10 (2015).

165 Falah, R. R., Talib, W. H. & Shbailat, S. J. Combination of metformin and curcumin targets breast cancer in mice by angiogenesis inhibition, immune system modulation and induction of p53 independent apoptosis. *Therapeutic advances in medical oncology* **9**, 235-252 (2017).

166 Old, L. J., Clarke, D. A. & Benacerraf, B. Effect of Bacillus Calmette-Guerin infection on transplanted tumours in the mouse. *Nature* **184**, 291-292 (1959).

167 Cooper, M. A., Fehniger, T. A. & Caligiuri, M. A. The biology of human natural killer-cell subsets. *Trends in immunology* **22**, 633-640 (2001).

168 Zwirner, N. W. & Domaica, C. I. Cytokine regulation of natural killer cell effector functions. *Biofactors* **36**, 274-288 (2010).

169 Cooper, M. A. *et al.* Cytokine-induced memory-like natural killer cells. *Proceedings of the National Academy of Sciences* **106**, 1915-1919 (2009).

170 De Maria, A., Bozzano, F., Cantoni, C. & Moretta, L. Revisiting human natural killer cell subset function revealed cytolytic CD56dimCD16+ NK cells as rapid producers of abundant IFN-γ on activation. *Proceedings of the National Academy of Sciences* **108**, 728-732 (2011).

171 Fuge, O., Vasdev, N., Allchorne, P. & Green, J. S. Immunotherapy for bladder cancer. *Research and reports in urology*, 65-79 (2015).

172 Kawai, K., Miyazaki, J., Joraku, A., Nishiyama, H. & Akaza, H. B acillus C almette–G uerin (BCG) immunotherapy for bladder cancer: Current understanding and perspectives on engineered BCG vaccine. *Cancer science* **104**, 22-27 (2013).

173 Hockfield, S. & McKay, R. Identification of major cell classes in the developing mammalian nervous system. *Journal of Neuroscience* **5**, 3310-3328 (1985).

174 Raj, B. & Blencowe, B. J. Alternative splicing in the mammalian nervous system: recent insights into mechanisms and functional roles. *Neuron* **87**, 14-27 (2015).

175 Varadarajan, S. G., Hunyara, J. L., Hamilton, N. R., Kolodkin, A. L. & Huberman, A. D. Central nervous system regeneration. *Cell* **185**, 77-94 (2022).

176 Nudell, V. *et al.* HYBRiD: hydrogel-reinforced DISCO for clearing mammalian bodies. *Nature methods* **19**, 479-485 (2022).

177 Gong, L., Liu, X., Wu, J. & He, M. Emerging strategies for the genetic dissection of gene functions, cell types, and neural circuits in the mammalian brain. *Molecular Psychiatry* **27**, 422-435 (2022).

178 Seng, C., Luo, W. & Földy, C. Circuit formation in the adult brain. *European Journal of Neuroscience* **56**, 4187-4213 (2022).

179 Ni, Y. *et al.* Flexible optoelectronic neural transistors with broadband spectrum sensing and instant electrical processing for multimodal neuromorphic computing. *SmartMat* **4**, e1154 (2023).

180 Dupuit, V. *et al.* A Multifunctional Hybrid Graphene and Microfluidic Platform to Interface Topological Neuron Networks. *Advanced Functional Materials*, 2207001 (2022).

181 Lin, L. *et al.* Large-scale neural ensemble recording in the brains of freely behaving mice. *Journal of neuroscience methods* **155**, 28-38 (2006).

182 Berdondini, L. *et al.* Active pixel sensor array for high spatio-temporal resolution electrophysiological recordings from single cell to large scale neuronal networks. *Lab on a Chip* **9**, 2644-2651 (2009).

183 Mantini, D., Perrucci, M. G., Del Gratta, C., Romani, G. L. & Corbetta, M. Electrophysiological signatures of resting state networks in the human brain. *Proceedings of the National Academy of Sciences* **104**, 13170-13175 (2007).

184 Singh, P., Saxena, K., Sahoo, P., Ghosh, S. & Bandyopadhyay, A. Electrophysiology using coaxial atom probe array: Live imaging reveals hidden circuits of a hippocampal neural network. *Journal of Neurophysiology* **125**, 2107-2116 (2021).

185 Joung, J. F. *et al.* Deep learning optical spectroscopy based on experimental database: potential applications to molecular design. *JACS Au* **1**, 427-438 (2021).

186 Zheng, X. S., Tan, C., Castagnola, E. & Cui, X. T. Electrode materials for chronic electrical microstimulation. *Advanced healthcare materials* **10**, 2100119 (2021).

187 Abdelfattah, A. S. *et al.* Bright and photostable chemigenetic indicators for extended in vivo voltage imaging. *Science* **365**, 699-704 (2019).

188 Chen, T.-W. *et al.* Ultrasensitive fluorescent proteins for imaging neuronal activity. *Nature* **499**, 295-300 (2013).

189 Thestrup, T. *et al.* Optimized ratiometric calcium sensors for functional in vivo imaging of neurons and T lymphocytes. *Nature methods* **11**, 175-182 (2014).

190 Chou, N. *et al.* A Multimodal Multi-Shank Fluorescence Neural Probe for Cell-Type-Specific Electrophysiology in Multiple Regions across a Neural Circuit. *Advanced Science* **9**, 2103564 (2022).

191 Kumar, A., Parihar, A., Panda, U. & Parihar, D. S. Microfluidics-based point-of-care testing (POCT) devices in dealing with waves of COVID-19 pandemic: The emerging solution. *ACS Applied Bio Materials* **5**, 2046-2068 (2022).

192 Ren, J. *et al.* Recent advances in microfluidics-based cell migration research. *Lab on a Chip* (2022).

193 Ramezankhani, R., Solhi, R., Chai, Y. C., Vosough, M. & Verfaillie, C. Organoid and microfluidics-based platforms for drug screening in COVID-19. *Drug discovery today* **27**, 1062-1076 (2022).

194 Ramlan, N., Zubairi, S. I. & Maskat, M. Y. Response Surface Optimisation of Polydimethylsiloxane (PDMS) on Borosilicate Glass and Stainless Steel (SS316) to Increase Hydrophobicity. *Molecules* **27**, 3388 (2022).

195 Persson, H. *et al.* Rapid assembly of PMMA microfluidic devices with PETE membranes for studying the endothelium. *Sensors and Actuators B: Chemical* **356**, 131342 (2022).

196 Gostel, M. R., Zúñiga, J. D., Kress, W. J., Funk, V. A. & Puente-Lelievre, C. Microfluidic Enrichment Barcoding (MEBarcoding): A new method for high throughput plant DNA barcoding. *Scientific Reports* **10**, 8701 (2020).

197 Wang, C. *et al.* Nanoplasmonic Sandwich Immunoassay for Tumor-Derived Exosome Detection and Exosomal PD-L1 Profiling. *ACS Sensors* **6**, 3308-3319 (2021).

198 Nguyen, Q. H. & Kim, M. I. Nanomaterial-mediated paper-based biosensors for colorimetric pathogen detection. *TrAC Trends in Analytical Chemistry* **132**, 116038 (2020).

199 Illath, K., Narasimahan, A. K., Nagai, M., Wankhar, S. & Santra, T. S. in *Microfluidics and Bio-MEMS* 429-501 (Jenny Stanford Publishing, 2020).

200 Li, Q., Niu, K., Wang, D., Xuan, L. & Wang, X. Low-cost rapid prototyping and assembly of an open microfluidic device for a 3D vascularized organ-on-a-chip. *Lab on a Chip* **22**, 2682-2694 (2022).

201 Ma, C., Peng, Y., Li, H. & Chen, W. Organ-on-a-chip: a new paradigm for drug development. *Trends in pharmacological sciences* **42**, 119-133 (2021).

202 Campbell, S. B. *et al.* Beyond polydimethylsiloxane: alternative materials for fabrication of organ-on-a-chip devices and microphysiological systems. *ACS biomaterials science & engineering* **7**, 2880-2899 (2020).

203 Carvalho, V. *et al.* 3D printing techniques and their applications to organ-on-a-chip platforms: A systematic review. *Sensors* **21**, 3304 (2021).

204 Richard, C., Neild, A. & Cadarso, V. J. The emerging role of microfluidics in multi-material 3D bioprinting. *Lab on a Chip* **20**, 2044-2056 (2020).

205 Liu, X. *et al.* Tumor-on-a-chip: from bioinspired design to biomedical application. *Microsystems & Nanoengineering* **7**, 50 (2021).

206 Zhou, L. *et al.* Spatiotemporal dissection of tumor microenvironment via in-situ sensing and monitoring in tumor-on-a-chip. *Biosensors and Bioelectronics*, 115064 (2023).

207 Xiao, Y. & Yu, D. Tumor microenvironment as a therapeutic target in cancer. *Pharmacology & therapeutics* **221**, 107753 (2021).

208 Kundu, S. C. & Reis, R. *Biomaterials for 3D Tumor Modeling*. (Elsevier, 2020).

209 Kumar, V. & Varghese, S. Ex Vivo Tumor-on-a-Chip Platforms to Study Intercellular Interactions within the Tumor Microenvironment. *Advanced healthcare materials* **8**, 1801198 (2019).

210 Brassard, J. A., Nikolaev, M., Hübscher, T., Hofer, M. & Lutolf, M. P. Recapitulating macro-scale tissue self-organization through organoid bioprinting. *Nature Materials* **20**, 22-29 (2021).

211 Mao, X. *et al.* Crosstalk between cancer-associated fibroblasts and immune cells in the tumor microenvironment: new findings and future perspectives. *Molecular cancer* **20**, 1-30 (2021).

212 Sobierajska, K., Ciszewski, W. M., Sacewicz-Hofman, I. & Niewiarowska, J. Endothelial cells in the tumor microenvironment. *Tumor Microenvironment: Non-Hematopoietic Cells*, 71-86 (2020).

213 Chanmee, T., Ontong, P., Konno, K. & Itano, N. Tumor-associated macrophages as major players in the tumor microenvironment. *Cancers* **6**, 1670-1690 (2014).

214 Cretu, A. & Brooks, P. C. Impact of the non-cellular tumor microenvironment on metastasis: potential therapeutic and imaging opportunities. *Journal of cellular physiology* **213**, 391-402 (2007).

215 Baghban, R. *et al.* Tumor microenvironment complexity and therapeutic implications at a glance. *Cell Communication and Signaling* **18**, 1-19 (2020).

216 Masson, J.-F. Surface plasmon resonance clinical biosensors for medical diagnostics. *ACS sensors* **2**, 16-30 (2017).

217 Acimovic, S. S. *et al.* LSPR chip for parallel, rapid, and sensitive detection of cancer markers in serum. *Nano letters* **14**, 2636-2641 (2014).

218 Dantham, V. R. *et al.* Label-free detection of single protein using a nanoplasmonic-photonic hybrid microcavity. *Nano letters* **13**, 3347-3351 (2013).

219 Yavas, O. *et al.* Self-calibrating on-chip localized surface plasmon resonance sensing for quantitative and multiplexed detection of cancer markers in human serum. *ACS sensors* **3**, 1376-1384 (2018).

220 Hornbeck, P. V. Enzyme-linked immunosorbent assays. *Current protocols in immunology* **110**, 2.1. 1-2.1. 23 (2015).

221 Baaske, M. D., Foreman, M. R. & Vollmer, F. Single-molecule nucleic acid interactions monitored on a label-free microcavity biosensor platform. *Nature nanotechnology* **9**, 933-939 (2014).

222 Vlasov, Y. A., Bo, X.-Z., Sturm, J. C. & Norris, D. J. On-chip natural assembly of silicon photonic bandgap crystals. *Nature* **414**, 289-293 (2001).

223 Sun, Y. & Fan, X. Optical ring resonators for biochemical and chemical sensing. *Analytical and bioanalytical chemistry* **399**, 205-211 (2011).

224 Homola, J. Surface plasmon resonance sensors for detection of chemical and biological species. *Chemical reviews* **108**, 462-493 (2008).

225 Choi, H. Y. *et al.* Miniature fiber-optic high temperature sensor based on a hybrid structured Fabry–Perot interferometer. *Optics letters* **33**, 2455-2457 (2008).

226 Im, H. *et al.* Label-free detection and molecular profiling of exosomes with a nano-plasmonic sensor. *Nature biotechnology* **32**, 490-495 (2014).

227 Eustis, S. & El-Sayed, M. A. Why gold nanoparticles are more precious than pretty gold: noble metal surface plasmon resonance and its enhancement of the radiative and nonradiative properties of nanocrystals of different shapes. *Chemical society reviews* **35**, 209-217 (2006).

228 Zijlstra, P., Paulo, P. M. & Orrit, M. Optical detection of single non-absorbing molecules using the surface plasmon resonance of a gold nanorod. *Nature nanotechnology* **7**, 379-382 (2012).

229 Xu, S. *et al.* Highly uniform gold nanobipyramids for ultrasensitive colorimetric detection of influenza virus. *Analytical Chemistry* **89**, 1617-1623 (2017).

230 Siabi-Garjan, A. & Savaloni, H. Extinction spectra and electric field enhancement of silver chiral nano-flower shaped nanoparticle; comparison of discrete dipole approximation results with experimental results. *The European Physical Journal B* **86**, 1-13 (2013).

231 Xu, Z., Hou, Y. & Sun, S. Magnetic core/shell Fe3O4/Au and Fe3O4/Au/Ag nanoparticles with tunable plasmonic properties. *Journal of the American Chemical Society* **129**, 8698-8699 (2007).

232 Im, H. *et al.* Template-stripped smooth Ag nanohole arrays with silica shells for surface plasmon resonance biosensing. *Acs Nano* **5**, 6244-6253 (2011).

233 Sepúlveda, B., Angelomé, P. C., Lechuga, L. M. & Liz-Marzán, L. M. LSPR-based nanobiosensors. *nano today* **4**, 244-251 (2009).

234 Song, Y. *et al.* AC electroosmosis-enhanced nanoplasmofluidic detection of ultralow-concentration cytokine. *Nano letters* **17**, 2374-2380 (2017).

235 Oh, B.-R. *et al.* Integrated nanoplasmonic sensing for cellular functional immunoanalysis using human blood. *ACS nano* **8**, 2667-2676 (2014).

236 Zhu, J. *et al.* An integrated adipose-tissue-on-chip nanoplasmonic biosensing platform for investigating obesity-associated inflammation. *Lab on a Chip* **18**, 3550-3560 (2018).

237 Xia, Q. *et al.* Fabrication of Fe 3 O 4@ Au hollow spheres with recyclable and efficient catalytic properties. *New Journal of Chemistry* **40**, 818-824 (2016).

238 Gates, B. D. *et al.* New approaches to nanofabrication: molding, printing, and other techniques. *Chemical reviews* **105**, 1171-1196 (2005).

239 Cetin, A. E. *et al.* Handheld high-throughput plasmonic biosensor using computational on-chip imaging. *Light: Science & Applications* **3**, e122-e122 (2014).

240 Jeong, U. Teng x, Wang y, yang H, xia y. *Superparamagnetic colloids: controlled synthesis and niche applications. adv Mater* **19**, 33-60 (2007).

241 Chen, P. *et al.* Multiplex serum cytokine immunoassay using nanoplasmonic biosensor microarrays. *ACS nano* **9**, 4173-4181 (2015).

242 Romanov, V. *et al.* A critical comparison of protein microarray fabrication technologies. *Analyst* **139**, 1303-1326 (2014).

243 Khan, S. S., Smith, M. S., Reda, D., Suffredini, A. F. & McCoy Jr, J. P. Multiplex bead array assays for detection of soluble cytokines: comparisons of sensitivity and quantitative values among kits from multiple manufacturers. *Cytometry Part B: Clinical Cytometry: The Journal of the International Society for Analytical Cytology* **61**, 35-39 (2004).

244 Claussen, J. C., Franklin, A. D., ul Haque, A., Porterfield, D. M. & Fisher, T. S. Electrochemical biosensor of nanocube-augmented carbon nanotube networks. *ACS nano* **3**, 37-44 (2009).

245 Oh, B.-R. *et al.* Multiplexed nanoplasmonic temporal profiling of T-cell response under immunomodulatory agent exposure. *Acs Sensors* **1**, 941-948 (2016).

246 Pan, J. *et al.* Combined magnetic hyperthermia and immune therapy for primary and metastatic tumor treatments. *ACS nano* **14**, 1033-1044 (2020).

247 Liu, X. *et al.* Comprehensive understanding of magnetic hyperthermia for improving antitumor therapeutic efficacy. *Theranostics* **10**, 3793 (2020).

248 Pan, J., Xu, Y., Wu, Q., Hu, P. & Shi, J. Mild magnetic hyperthermia-activated innate immunity for liver cancer therapy. *Journal of the American Chemical Society* **143**, 8116-8128 (2021).

249 Soleymani, M., Velashjerdi, M., Shaterabadi, Z. & Barati, A. One-pot preparation of hyaluronic acid-coated iron oxide nanoparticles for magnetic hyperthermia therapy and targeting CD44-overexpressing cancer cells. *Carbohydrate polymers* **237**, 116130 (2020).

250 Gonzalez-Rodriguez, R., Campbell, E. & Naumov, A. Multifunctional graphene oxide/iron oxide nanoparticles for magnetic targeted drug delivery dual magnetic resonance/fluorescence imaging and cancer sensing. *PLoS One* **14**, e0217072 (2019).

251 Manzari, M. T. *et al.* Targeted drug delivery strategies for precision medicines. *Nature Reviews Materials* **6**, 351-370 (2021).

252 Liang, Y., Duan, L., Lu, J. & Xia, J. Engineering exosomes for targeted drug delivery. *Theranostics* **11**, 3183 (2021).

253 Chen, W., Yang, W., Chen, P., Huang, Y. & Li, F. Disulfiram Copper Nanoparticles Prepared with a Stabilized Metal Ion Ligand Complex Method for Treating Drug-Resistant Prostate Cancers. *ACS Applied Materials & Interfaces* **10**, 41118-41128 (2018).

254 Bauer, G., Sersenová, D., Graves, D. B. & Machala, Z. Cold atmospheric plasma and plasma-activated medium trigger RONS-based tumor cell apoptosis. *Scientific reports* **9**, 14210 (2019).

255 Sarhan, M., von Mässenhausen, A., Hugo, C., Oberbauer, R. & Linkermann, A. Immunological consequences of kidney cell death. *Cell Death & Disease* **9**, 114 (2018).

256 Lamouille, S., Xu, J. & Derynck, R. Molecular mechanisms of epithelial–mesenchymal transition. *Nature reviews Molecular cell biology* **15**, 178-196 (2014).

257 Ghasemi, M., Turnbull, T., Sebastian, S. & Kempson, I. The MTT assay: utility, limitations, pitfalls, and interpretation in bulk and single-cell analysis. *International journal of molecular sciences* **22**, 12827 (2021).

258 Bedoui, S., Herold, M. J. & Strasser, A. Emerging connectivity of programmed cell death pathways and its physiological implications. *Nature reviews Molecular cell biology* **21**, 678-695 (2020).

259 Nunes, A. S., Barros, A. S., Costa, E. C., Moreira, A. F. & Correia, I. J. 3D tumor spheroids as in vitro models to mimic in vivo human solid tumors resistance to therapeutic drugs. *Biotechnology and bioengineering* **116**, 206-226 (2019).

260 Martinotti, S. & Ranzato, E. Scratch wound healing assay. *Epidermal cells: methods and protocols*, 225-229 (2020).

261 Sahai, E. *et al.* A framework for advancing our understanding of cancer-associated fibroblasts. *Nature Reviews Cancer* **20**, 174-186 (2020).

262 Chen, Y., McAndrews, K. M. & Kalluri, R. Clinical and therapeutic relevance of cancer-associated fibroblasts. *Nature reviews Clinical oncology* **18**, 792-804 (2021).

263 Fucikova, J. *et al.* Detection of immunogenic cell death and its relevance for cancer therapy. *Cell death & disease* **11**, 1013 (2020).

264 Zhang, S. *et al.* Emerging photodynamic nanotherapeutics for inducing immunogenic cell death and potentiating cancer immunotherapy. *Biomaterials* **282**, 121433 (2022).

265 Zheng, P. *et al.* Ultrasound-augmented mitochondrial calcium ion overload by calcium nanomodulator to induce immunogenic cell death. *Nano Letters* **21**, 2088-2093 (2021).

266 Liu, S. *et al.* 3D culture boosting fullerenol nanoparticles to induce calreticulin exposure on MCF-7 cells for enhanced macrophage-mediated cell removal. *Colloids and Surfaces B: Biointerfaces*, 113204 (2023).

267 Ye, M. *et al.* Near-infrared light controllable DNA walker driven by endogenous adenosine triphosphate for in situ spatiotemporal imaging of intracellular microRNA. *ACS nano* **15**, 14253-14262 (2021).

268 Kim, M., Kim, G., Hwang, D. W. & Lee, M. Delivery of high mobility group box-1 siRNA using brain-targeting exosomes for ischemic stroke therapy. *Journal of biomedical nanotechnology* **15**, 2401-2412 (2019).

269 Chen, Y., Du, M., Yuan, Z., Chen, Z. & Yan, F. Spatiotemporal control of engineered bacteria to express interferon-γ by focused ultrasound for tumor immunotherapy. *Nature Communications* **13**, 4468 (2022).

270 Yang, J. *et al.* Guidelines and definitions for research on epithelial–mesenchymal transition. *Nature reviews Molecular cell biology* **21**, 341-352 (2020).

271 Katsuno, Y. & Derynck, R. Epithelial plasticity, epithelial-mesenchymal transition, and the TGF-β family. *Developmental cell* **56**, 726-746 (2021).

272 Zhang, N. *et al.* Novel therapeutic strategies: Targeting epithelial–mesenchymal transition in colorectal cancer. *The Lancet Oncology* **22**, e358-e368 (2021).

273 Dudek, M. *et al.* Auto-aggressive CXCR6+ CD8 T cells cause liver immune pathology in NASH. *Nature* **592**, 444-449 (2021).

274 Wang, W. & Wang, G.-Z. Understanding molecular mechanisms of the brain through transcriptomics. *Frontiers in physiology* **10**, 214 (2019).

275 Dipalo, M. *et al.* 3D plasmonic nanoantennas integrated with MEA biosensors. *Nanoscale* **7**, 3703-3711 (2015).

276 Ehret, F., Vogler, S. & Kempermann, G. A co-culture model of the hippocampal neurogenic niche reveals differential effects of astrocytes, endothelial cells and pericytes on proliferation and differentiation of adult murine precursor cells. *Stem cell research* **15**, 514-521 (2015).

277 Dipalo, M. *et al.* Plasmonic meta-electrodes allow intracellular recordings at network level on high-density CMOS-multi-electrode arrays. *Nature nanotechnology* **13**, 965-971 (2018).

278 Tischbirek, C., Birkner, A., Jia, H., Sakmann, B. & Konnerth, A. Deep two-photon brain imaging with a red-shifted fluorometric Ca²⁺ indicator. *Proceedings of the National Academy of Sciences* **112**, 11377-11382 (2015).

279 Zhang, J., Atay, T. & Nurmikko, A. V. Optical Detection of Brain Cell Activity Using Plasmonic Gold Nanoparticles. *Nano Letters* **9**, 519-524 (2009).

280 Gómez-Aguilar, J. F. Novel analytical solutions of the fractional Drude model. *Optik* **168**, 728-740 (2018).

281 Bade, W. L. Drude-Model Calculation of Dispersion Forces. I. General Theory. *The Journal of Chemical Physics* **27**, 1280-1284 (1957).

282 Oldham, K. B. A Gouy–Chapman–Stern model of the double layer at a (metal)/(ionic liquid) interface. *Journal of Electroanalytical Chemistry* **613**, 131-138 (2008).